Plasma Dynamics of Very-High-Frequency (VHF) Discharges with Application to Atomic-Layer-Etching (ALE)

Cleo Harvey B.Sc.

School of Physical Sciences

Dublin City University

Research Supervisor:

Prof. Albert R. Ellingboe

A thesis submitted for the degree of

Doctor of Philosophy (Ph.D.)

May 2021

Declaration

I hereby certify that this material, which I now submit for assessment on the programme of study leading to the award of PhD is entirely my own work, that I have exercised reasonable care to ensure that the work is original, and does not to the best of my knowledge breach any law of copyright, and has not been taken from the work of others save and to the extent that such work has been cited and acknowledged within the text of my work.

Signed:

(Candidate) ID No.: 10336895
Date: 31/05/2021

Acknowledgements

First and foremost, I would like to express my sincerest gratitude to my supervisor Dr. Bert Ellingboe for giving me the opportunity to undertake this research in the Plasma Research Laboratory (PRL), and for the continued support in getting me to the finish line. I will always be grateful.

A huge thanks to Dr. Cezar Gaman and Dr. Nishant Sirse for being invaluable mentors to me.

I am grateful to the technical staff in the School of Physics, namely Des Lavelle, Pat Wogan, and Alan Hughes.

Many thanks to Shane O'Donnell and the other members of the Surface Science group in the School of Physics for their contributions to the work on the XPS data.

Thanks to all the friends I made throughout my time in the physics department. I especially thank Adam D, Adam P, Aoife, Brian, Claire, Conor, Deirdre, Huw, Paul, Ronan and Stephen for all the great memories.

To all my friends from home or otherwise, I thank you for your years of friendship and continued support.

Special thanks to my Bayview housemates and friends. You have been so wonderful to live with, and thank you for the distractions when I needed it.

To Ben, thank you for all your encouragement. You never doubted me.

Finally, I thank my parents Francie and Margaret, and my brother Ross who have supported me in everything I do with unwavering con-

fidence and support. I will be forever grateful. I dedicate this thesis to you.

Publications

Research work has been disseminated through the following publications:

Journal Publications

C. Harvey, N. Sirse, C. Gaman and A.R. Ellingboe, *Mode transition in an oxygen low-pressure, very high frequency (162 MHz), multi-tile electrode capacitively coupled plasma.* Phys. Plasmas 27(11), 2020 (Editor's Pick)

C. Harvey, S. Vandenburg and A.R. Ellingboe, *A non-Equilibrium Atmospheric Pressure Capacitively-Coupled-Plasma (CCP) driven at VHF(162MHz) for Plasma Catalysis of CO2 into CO.* Curr Appl Phys 2021

N. Sirse, C. Harvey, C. Gaman and A.R. Ellingboe, *Investigation of plasma uniformity, rotational and vibrational temperature in a 162 MHz multi-electrode capacitive discharge.* J. Phys. D: Appl. Phys 53(33), 2020

Conference Papers

C. Harvey, N. Sirse, C. Gaman and A.R. Ellingboe, *Experimental study of a high-VHF multi-electrode capacitively-coupled-plasma for thin layer surface processing.* 44th EPS Conference on Plasma Physics, Belfast, Ireland 26-30 June 2017

Oral Presentations

C. Harvey, N. Sirse, C. Gaman and A.R. Ellingboe, *Power-coupling Mode-Change in a high-VHF (162MHz) Multi-tile, Capacitively-coupled Plasma.* Joint International Conference on the 8th ICMAP & 9th ISFM, Online Conference, 17-20 January 2021

C. Harvey, and A.R. Ellingboe, *Demonstration of Atomic-Layer-Etching of SiO_2 in a small-plasma-volume system incorporating 162 MHz CCP-source and 27 MHz substrate-bias using CHF_3 and Ar/O_2* Accepted to present at the 8th International ALE Workshop, Online Conference, 27-30 June 2021

Poster Presentations

Cleo Harvey, N. Sirse, C. Gaman and A.R. Ellingboe, *Mode transition in an oxygen low-pressure, very high frequency (162 MHz), multi-tile electrode capacitively coupled plasma.* 73rd Annual GEC Conference, 5-9 October 2020 (Winner of Graduate Student Poster Award)

Cleo Harvey and A.R. Ellingboe, *A non-Equilibrium Atmospheric Pressure Plasma for Reprocessing of CO2 for Renewable Energy Storage.* IoP Spring Meeting, Athlone, Ireland, March 2019 (Finalist for Rosse Medal)

N. Sirse, C. Harvey, C. Gaman and A.R. Ellingboe, *Electron Energy Distribution Function in a Weakly Magnetized Expanding Helicon Plasma Discharge.* 69th Annual GEC Conference, Bochum, Germany, 10-14 October 2016

Contents

List of Abbreviations

ALD	Atomic Layer Deposition
ALE	Atomic Layer Etching
BEOL	Back End of Line
CCP	Capacitively Coupled Plasma
CW	Continuous Wave
E-S	Electrostatic
ECR	Electron Cyclotron Resonance
EEDF	Electron Energy Distribution Function
EI	Electron Impact
EPC	Etch per Cycle
EQP	Electrostatic Quadrupole Plasma
ESC	Electrostatic Chuck
FC	Fluorocarbon
FPS	First Positive System
FWHM	Full Width Half Maximum
HPEM	Hybrid Plasma Equipment Model
ICP	Inductively Coupled Plasma
IED	Ion Energy Distribution
LF	Low Frequency
MD	Molecular Dynamics

MERIE	Magnetically Enhanced Reactive Ion Etcher
MFC	Mass Flow Controllers
OES	Optical Emission Spectroscopy
PEM	Photoelastic Modulator
PI	Plasma Ion
PMSE	Phase-Modulated-Spectroscopic Ellipsometer
PMT	Photo-multiplier Tube
PSTLD	Power Splitting Line Driver
RAS	Reflection Anisotropic Spectroscopy
RF	Radio Frequency
RGA	Residual Gas Analysis
RIE	Reactive Ion Etching
RSLA	Radial Slot-Line Antennae
SAC	Self Aligned Contacts
SEM	Secondary Electron Multiplier
SPS	Second Positive System
UHF	Ultra High Frequency
UV	Ultra-Violet
VHF	Very High Frequency
VUV	Vacuum Ultra-Violet
XPS	X-ray Photoelectron Spectroscopy

List of Figures

List of Tables

Abstract

Cleo Harvey

Plasma Dynamics of Very-High-Frequency (VHF) Discharges with Application to Atomic-Layer-Etching (ALE)

Processing of SiO_2 layers with atomic scale control is one of the main requirements to achieve nanoscale device fabrication. In this thesis, a novel (multi-frequency) Capacitively-Coupled-Plasma (CCP) system with a Very-High-Frequency (VHF) multi-tile electrode is investigated for the application to cyclic fluorocarbon-based etching of SiO_2, based on a two-step Atomic-Layer-Etch process. This system (*Starchief*) is a modification of an industrial wafer-processing tool, originally comprised of a lower powered (2+27 MHz) and upper grounded electrode. For this research, the upper grounded electrode is replaced with a multi-tile-array excited at 162 MHz. The unique plasma chemistry and low energy sheath of high-VHF limits ion-driven surface mixing; this in turn promotes an etch plateau resulting in a broader ALE process window with a self-limiting removal half-cycle. Investigation into the unique plasma physics of high-VHF excitation and power coupling mechanisms of a multi-tile electrode is conducted in a single-frequency powered plasma source, called PASTIS. In a nitrogen discharge, optical emission spectroscopy results show large differences between vibrational ($\sim$6200-9400 K) and rotational gas ($\sim$350-450 K) temperatures, which suggest highly non-equilibrium conditions. The ratio of stochastic to ohmic heating is determined, and even at high operating pressures ($>$ 500 mTorr), the VHF plasma is driven dominantly

by stochastic electron heating. Ion energy distributions (IEDs), measured using an energy-resolved mass spectrometer, exhibit symmetric narrow distributions due to very-high-frequency plasma operation. Negative ion densities are inferred from measured electron density and ion flux using resonance hairpin probe and planar probe respectively. In a low-pressure electronegative discharge, measured electrode voltage and current, charged particle density, including negative ions, and ion energy distributions exhibit a mode transition versus RF power. The results conclude that the observed mode transition is caused by the change in current coupling mechanisms and modification in the discharge impedance, including the presence of negative ions. In electropositive, and high-pressure electronegative discharges, the ion energy distribution trends versus RF power provide evidence of electrical asymmetry; the push-pull power delivery to the multi-tile electrode result in floating electrode tiles that develop a DC bias such that ion energy delivered to the substrate-holding electrode is substantially reduced. The significance of this is that the solution of a multi-tile electrode CCP driven at VHF facilitates independent control of flux densities and low-ion-energy driven sheaths. In the *Starchief* system, a Phase-Modulated Spectroscopic Ellipsometer (PMSE) is used for in-situ monitoring of the surface changes at each half-cycle of the ALE process. The atomic composition and chemical bonding structure of the fluorocarbon modified layers are analysed by x-ray photoelectron spectroscopy (XPS). This research highlights the potential of combining existing atomic-layer-process technology, with a large-scale VHF CCP which enables unique plasma and surface chemistry necessary for next generation processing.

Chapter 1

Introduction

Contents

1.1 Introduction

The demands to construct evermore powerful computing devices is driving the semiconductor industry to continuously scale manufacturing dimensions, such that there is an urgent need for surface processing techniques with atomic control.

The performance of nano-manufactured devices rely critically on the etching step, where silicon dioxide (SiO_2) is one of the most commonly used dielectric materials in etching of device architectures [1]. The etch challenges for these architectures continue to change as process features scale below 10 nm dimensions [2]. Indeed, removing material with atomic-layer precision is a complex scientific problem, especially in directional plasma etching. It is therefore critical to develop a solid understanding of the processing environment; This includes the plasma kinetics, the resultant gas-phase chemistry, and interactions with the surface including ion-induced reactions. Furthermore, wafer sizes of 300 mm diameter and beyond (or other size substrates including those for roll-to-roll processing) are forecast to be in full-scale use, such that an understanding of the engineering and radio-frequency (RF) power coupling mechanisms involved in large-area plasma reactors is also of utmost importance.

1.1.1 Motivation for Research

Plasma-based Atomic-Layer-Etching (ALE) is an emerging etching technique that has the potential to meet the most stringent of scaling challenges and ameliorate next-generation manufacturing. The motivation for this research is to investigate how modifications to plasma discharge kinetics in VHF operation affect Atomic-Layer-Etching technology. To date, the majority of publications and research work in Atomic-Layer-Etching have been conducted in small-area rectors driven by conventional 13.56 MHz frequency. In low-pressure plasma processing, the advantages of increasing the driving frequency into the very-high-frequency (VHF) band are known, but the field is still deficient in experimental data of VHF discharges. The is mainly due to the electromagnetic non-uniformity effects that hinder VHF implementation in large-area systems. A primary aim of this research is to advance the development and understanding of a large-area multi-tile (differentially-powered), very-high-frequency plasma source, and two different configurations are utilized: PASTIS and *Starchief*. In this work, we are interested in plasmas tailored for atomic-layer-etching of SiO_2. For dielectric etching, fluorocarbon gases with argon and oxygen are generally used. The

complicated fluorocarbon chemistry requires appropriate plasma-driven reactions in the gas-phase that result in suitable surface reactions. The *Starchief* system is investigated as an appropriate system for fluorocarbon based SiO_2 ALE, and aims to address current limitations of fully self-limiting etching of SiO_2.

1.2 Plasma Theory

Plasma is a quasi-neutral gaseous mixture of electrons, ions and neutral particles, where quasi-neutral implies a close to equal density of the positively and negatively charged species. The term plasma was first coined by Irving Langmuir in 1928 [3] because the manner in which ionized gases carried the high-velocity electrons, ions, and impurities reminded him of blood plasma carrying red and white blood cells. Plasma can be produced by supplying energy from heat, or electro-magnetic fields to a gas, resulting in the energy of the gaseous molecules exceeding the ionization energy of the constituent gas. The degree of ionization of a plasma (α_{is}) describes the proportion of atoms which have lost or gained electrons via collisions, expressed as:

$$\alpha_{is} = \frac{n_i}{n_i + n_n} \tag{1.1}$$

where n_n is the neutral gas density, and n_i is the density of ions ($\approx$ the density of electrons n_e). For fully ionized plasmas α_{is} is nearly unity, whereas for weakly ionized plasmas $\alpha_{is} << 1$. Figure 1.1 identifies natural and man-made plasmas over a range of pressures, electron densities and temperatures. (It is convenient to characterise plasma by the temperatures of its constituents, which is simply the energy of the particles, directly related to their speed, as given by $\frac{1}{2}\, mv^2 = \frac{3}{2}\, \kappa_B T$, with temperature in units of eV). The conditions of plasma in the interstellar media are significantly different to the gas discharges that are used for industrial applications. For application to semiconductor manufacturing, we will deal only with weakly ionized gas discharges which contain electrons

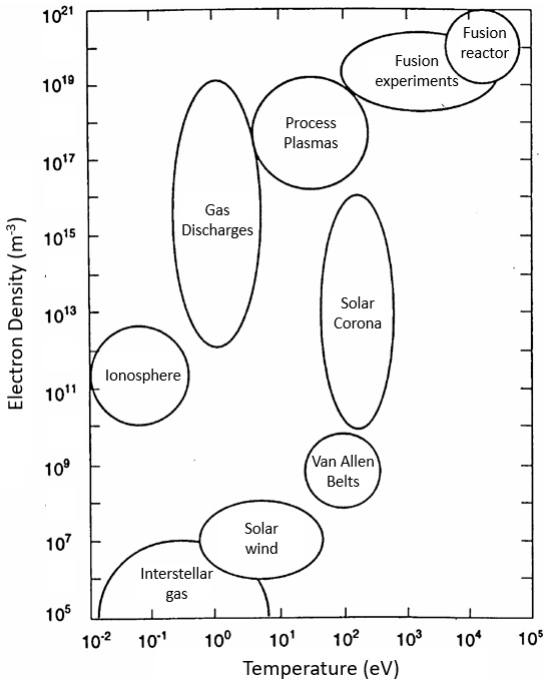

Figure 1.1: Plasma classification based on electron density and temperature, adapted from [4].

and ions that are not in thermal equilibrium, and are called "cold" plasmas[1]. In low-pressure discharges for industrial plasma processing, electrical power is used to sustain the plasma, which preferentially transfers power to the lower mass electrons (discussed further in Section 1.2.4). This results in the temperature of the electrons, T_e, being extremely high, e.g. 2 eV. In contrast, the ions collide with the dominant neutral particles with effective momentum transfer, resulting in ion temperatures, T_i, only slightly above the gas, and chamber, temperatures. Plasma is distinguished from ionized gas by "collective behaviour" of the free charge; collective behaviour particularly relevant to this thesis include the plasma frequency, Debye shielding, and sheath formation which will now be described.

[1]One such exception to this, is found in electron cyclotron resonance (ECR) plasma, in which the ionisation fraction can reach between 0.3 and 1.

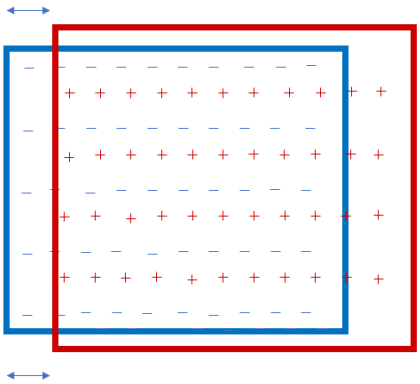

Figure 1.2: Illustration of an ion matrix (red) with an oscillating electron density cloud (blue) and characteristic restoring force.

1.2.1 Plasma Frequency

In a plasma, the charged particles arrange themselves in such a way as to oppose charge density imbalances. Consider, as in Figure 1.2, an ion matrix surrounded by an electron density cloud, where we initially assume the ions are stationary. If an external electric field E is applied to the plasma, the electrons will move along the electric field lines.

$$E = \frac{en_e}{\epsilon_0}\Delta x \tag{1.2}$$

where Δx is the displacement of the electrons from their equilibrium position, ϵ_0 is the permittivity of vacuum, and e is the electron charge. As the electrons move, a charge imbalance builds up which results in an electrostatic restoring force on the electrons. In the absence of collisions, the electrons will move back, overshoot their initial position due to inertia and continue to oscillate back and forth in Simple-Harmonic-Motion. From Equation 1.2 the motion of the electrons is described by:

$$\frac{d^2x}{dt^2} + \frac{e^2n_e}{\epsilon_0 m_e}x = 0 \tag{1.3}$$

which is the equation of motion for a harmonic oscillator. The frequency of the

sinusoidal electron cloud oscillation with respect to the ion matrix cloud, given by Equation 1.3, is the fundamental characteristic frequency of the plasma:

$$\omega_{pe} = (\frac{e^2 n_e}{\epsilon_0 m_e})^{1/2} \quad \rightarrow \quad f_{pe} = \frac{\omega_{pe}}{2\pi} \tag{1.4}$$

where m_e is the electron mass. Similarly, we define the ion frequency as

$$\omega_{pi} = (\frac{e^2 n_e}{\epsilon_0 m_i})^{1/2} \quad \rightarrow \quad f_{pi} = \frac{\omega_{pi}}{2\pi} \tag{1.5}$$

where m_i is the ion mass.
Electron frequency f_{pe} values for typical $n_e \sim 10^{10}\,\mathrm{cm}^{-3}$ are in the GHz range, compared to ion frequencies on the order of 1's MHz. Therefore, our assumption that the ions are fixed relative to the electrons is justified; the electrons react to an instantaneous change in electric field, nullifying the change in E before the ions can react. Note that the "long-range" electric force becomes localised to the edge of the plasma.

1.2.2 Debye Shielding

Suppose an electrostatic point charge is brought into contact with the plasma. This results in a perturbation to the local electric potential. The fast moving electrons reorganise themselves, amongst the much slower ions, to counter the imposed charge imbalance. The implication of this is that particles at a sufficient distance away from the perturbation will not be affected. To derive the scale length over which this electric potential screening occurs, we begin with Poisson's equation for a plasma in spherical co-ordinates

$$\frac{1}{r^2}\frac{d}{dr}\left(r^2 \frac{d\Phi(r)}{dr}\right) = -e\frac{(n_i - n_e(r))}{\epsilon_0} \tag{1.6}$$

where $\Phi(r)$ is the electric potential due to the point charge, and again the ions are fixed. The variation of the electron density over the region of the distur-

bance $n_e(r)$ follows a Maxwell-Boltzmann distribution such that Equation 1.6 becomes:

$$\frac{1}{r^2}\frac{d}{dr}\left(r^2\frac{d\Phi(r)}{dr}\right) = -\frac{en_e}{\epsilon_0}\left[1 - exp\left(\frac{-e\Phi(r)}{\kappa_B T_e}\right)\right] \tag{1.7}$$

where κ_B is Boltzmann's constant. Expanding the exponential term in a Taylor Series, and assuming $\Phi(r) < \kappa_B T_e$:

$$\frac{1}{r^2}\frac{d}{dr}\left(r^2\frac{d\Phi(r)}{dr}\right) = \frac{en_e}{\epsilon_0}\left[\left(\frac{-e\Phi(r)}{\kappa_B T_e}\right) - 1\right] \tag{1.8}$$

The solution to this differential equation is:

$$\Phi(r) = -\Phi_0 exp(\frac{r}{\lambda_D}\ ) \tag{1.9}$$

where λ_D is the characteristic screening length, called the Debye length:

$$\lambda_D = \sqrt{\frac{\epsilon_0 \kappa_B T_e}{n_e e^2}} \tag{1.10}$$

This length defines a sphere, the Debye sphere, of radius λ_D around an imposed charge. The ability of the plasma to reduce long-range electric fields is known as Debye shielding.

1.2.3 Sheath Formation

We now consider what happens when we confine the plasma within a boundary, known as a chamber or a reactor in technological plasma applications. This boundary imposes a potential, say ground, or floating for a metallic or dielectric boundary, and this invokes Debye-shielding at the plasma boundary. The chamber walls impose boundary conditions on the plasma such that quasi-neutrality

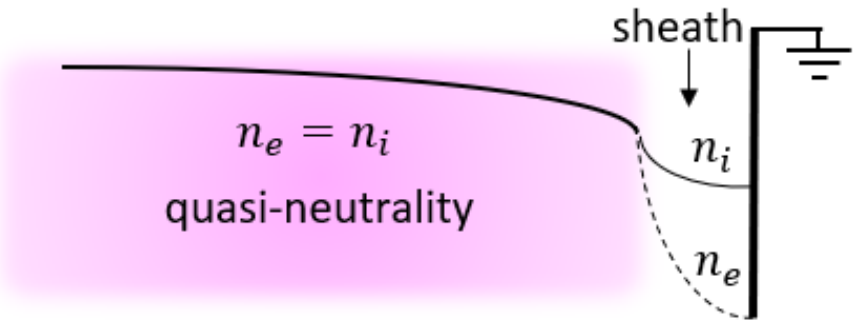

Figure 1.3: Quasi-neutral plasma separated from a grounded wall by a space charge sheath.

breaks down at the plasma-surface boundaries. Again, due to the mobility difference between the electrons and the ions, ($T_e >> T_i$), the electrons will initially be lost to the grounded walls at a faster rate, see Figure 1.3.

This results in the formation of a small layer of positive charge, called the sheath, dominated by positive ions. This positive space charge gives rise to an electric field, directed from the plasma to the wall, which repels further electrons from entering the region, and accelerates heavy ions to the walls. For the ions to be accelerated sufficiently to produce the charge separation, they must overcome the electrostatic forces attracting them back into the quasi-neutral bulk state, i.e. their velocity must be larger than the return speed to equilibrium. This means that at the boundary, the ions must have at least a speed u_s such that they break the screening effect λ_D, in a time less than the period of oscillation ω_{pi}.

$$u_s \geq \lambda_D \text{ x } \omega_{pi} = \sqrt{\frac{\kappa_B T_e}{m_i}} \equiv u_B \tag{1.11}$$

This velocity is known as the Bohm speed, u_B.

The plasma looses energy to the environment through formation of high-energy particles, which are lost or transported out of the system, such as ions, free electrons, rotationally and vibrationally excited states of atoms and molecules, and via radiation. To sustain the plasma in a "quasi-steady-state", equivalent

energy needs to be added into the plasma to balance losses. We will now discuss how this necessary energy is input to the plasma.

1.2.4 Electron Heating Mechanisms

Generally industrial plasmas are powered by imposing an RF-current on a boundary of the plasma, which means that the sheaths do not have a constant thickness; the electrons oscillate back and forth with a frequency of the RF excitation. This produces a mechanism for power deposition into the plasma. Again, because of the difference between the electron and ion mass, and the higher mobility of the electrons, power is preferentially coupled to the electrons. Two types of this electron "heating" in CCPs can be identified. In the high pressure case, bulk plasma electrons diffuse to electrodes during contraction of the sheath and accelerate back when it expands. The energy gained from the acceleration of the electrons in the electric field is transferred to thermal electron energy through local collisional processes. This is known as (collisional) ohmic heating and is analogous to running currents through metallic conductors where electrons exchange energy with other electrons, and eventually heat up the ions. The collisional ohmic power absorbed by electrons in plasma can be expressed as [4]:

$$P_{ohm} = \frac{1}{2}\tilde{J}^2\frac{1}{\sigma_p} \tag{1.12}$$

where $\tilde{J}$ is the current density and σ_p is the plasma conductivity:

$$\sigma_p = \frac{n_e e^2}{m(\omega + i\nu_m)} \tag{1.13}$$

where ω is the driving frequency and ν_m is the electron-neutral collision frequency [1].

The other heating mechanism in plasma occurs primarily at lower pressures where the electron mean free path is larger than the plasma gap. The electrons

[1] ν_m is defined later in Section 3.2, Equation 3.7

are more likely to interact with the sheaths rather than undergo collisions with gas molecules. The electron interaction with the sheath can be described by the "hard wall" model; a ball (electron) bouncing between rigid moving walls (sheaths). Assuming the collision is elastic, the change in velocity of an electron incident on the sheath with velocity u can be written as [4]:

$$u' = u + 2u_{sheath} \tag{1.14}$$

where u is the velocity after reflection, and u_{sheath} is the velocity of the plasma sheath boundary. Although this change in velocity (energy) can be positive or negative, on average there is an energy gain [5]. This type of collisionless electron heating is called stochastic.

1.2.5 Energy Distribution Functions

The range of electron energies in the plasma is known as the **Electron Energy Distribution Function (EEDF)**. This is a fundamental characteristic of a discharge and we will see how different types of EEDFs play a critical role in driving plasma chemistry that facilitate surface processing reactions. The general expression for the EEDF is:

$$f_c(E) \propto \sqrt{E}\, exp\left(\frac{-E^c}{\kappa_B T_e}\right) \tag{1.15}$$

The value of the parameter c determines the type of distribution, where c = 1 corresponds to a Maxwellian EEDF and c = 2 corresponds to a Druyvesteyn EEDF.
Figure 1.4 illustrates three extrema of electron energy distributions. The Maxwellian EEDF applies to an electron population in thermal equilibrium. Deviations from a classic Maxwellian distribution, such as Druyvesteyn and Bi-Maxwellian, are often a better representation of the EEDFs in technological discharges. Druyvesteyn is characteristic of bulk collisional-ohmic heating and depicts more electrons

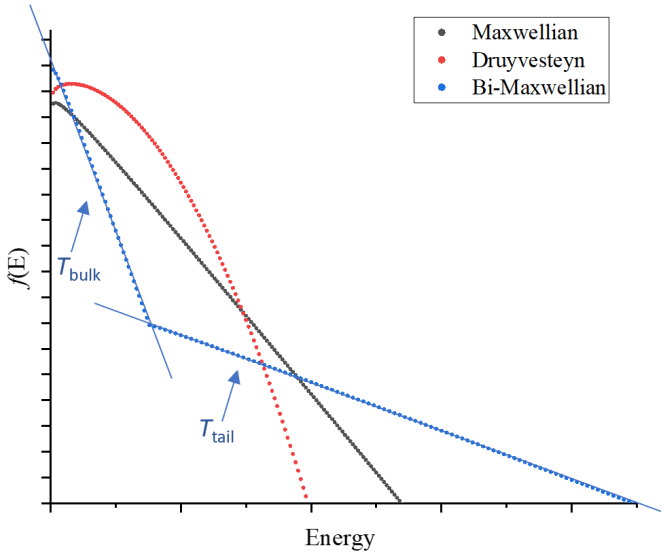

Figure 1.4: Illustrative plot of a Maxwellian, Druyvesteyn and Bi-Maxwellian EEDF.

with average energy and fewer high-energy electrons than a Maxwellian. A bi-Maxwellian distribution is generally observed at low-pressures [6] and is associated with dominate stochastic heating. The slope of two tangential lines indicated on the bi-Maxwellian curve in Figure 1.4 give a bulk electron temperature T_{bulk}, and high-energy tail electron temperature T_{tail}. In this regime, the majority of the electrons have very low-energy; they are confined in the bulk plasma and do not have enough energy to reach the oscillating sheaths, where stochastic heating takes place. On the other hand, the high-energy electrons effectively interact with the oscillating sheath, bouncing between them, and these electrons constitute T_{tail}. These high energy electrons have a significant effect on the chemical products produced in the plasma.

The energy with which the ions impinge the wafer surface is a critical parameter in any plasma material process. The ion spread, directed perpendicularly to the surface, is known as the **Ion Energy Distribution (IED)**. In DC discharges, the IED appears monoenergetic about eV_s, where V_s is the DC sheath voltage drop [7]. However, in RF discharges, ion modulation can cause large ion energy spreads. There are two main factors determining the shape and distribution of

the ion energies in RF discharges.

(i) RF Period (Frequency)

The ratio of the ion transit time τ_{ion} to the RF period τ_{rf} is the crucial parameter that determines that IED shape. The ion transit time is the time it takes an ion to travel the sheath when the sheath drop is at its DC value. The ratio is expressed as:

$$\frac{\tau_{ion}}{\tau_{rf}} = \frac{3\bar{s}\omega}{2\pi}\left(\frac{M}{2e\overline{V}_s}\right)^{1/2} \tag{1.16}$$

where $\bar{s}$ is the time averaged sheath thickness, $\overline{V}$ is the mean sheath voltage, ω is the RF frequency and M is the ion mass. There are three difference regimes; low frequency $\tau_{ion}/\tau_{rf} << 1$, intermediate frequency $\tau_{ion}/\tau_{rf} \approx 1$, and high frequency $\tau_{ion}/\tau_{rf} >> 1$. In the low frequency regime, the ions experience the instantaneous sheath voltage and the phase of the RF cycle in which the ion enters the sheath is important. The resultant IED has a double peak structure which is centred around the time averaged sheath potential. The higher energy peak corresponds to the ions entering the sheath at the maximum sheath voltage and the lower energy peak corresponds to the ions entering the sheath at the minimum sheath voltage. As the RF frequency increases, the ions can no longer respond to the oscillating RF sheath, they only experience the time-averaged sheath potential and therefore the phase in which the ions enter the sheath is no longer relevant. Consequently, the IED is a single peak structure in this regime that is centred at the time averaged sheath potential. For the case of the intermediate frequency regime, the ions take a couple of RF cycles to cross the sheath and the phase in which they enter the sheath is again important. The IED usually has a narrower gap two peak structure but with variations in the peak heights. The first analytical expression for the energy peak separation was provided by Beniot-Cattin and Bernard [8]:

$$\Delta E_i = \frac{8e\tilde{V}_s}{3\bar{s}\omega}\left(\frac{2e\bar{V}_s}{M}\right)^{1/2} = \frac{4e\tilde{V}_s}{\pi}\left(\frac{\tau_{ion}}{\tau_{rf}}\right) \tag{1.17}$$

This expression shows that the peak separation depends on frequency, RF voltage and sheath thickness. The energy spread is also dependent on ion mass (M), but for frequencies above 100 MHz, the IEDs are commensurate [9] which is important for varying mass plasma chemistries.

(ii) Sheath Collisions

If the ion mean free path (λ_i) is less than the sheath thickness, then ions undergo collisions which significantly change the shape of the IED. There are two kinds of collisions that effect the energy distributions, elastic collisions and symmetric charge exchange. The elastic collisions lead to loss in kinetic energy and a deviation from the perpendicular incidence of ions on the surface. The effect leads to wider angular distribution of the velocity of the ions and a low energy tail. Charge exchange collisions in the sheath generate new ions which will reach the sampling surface at a lower energy compared with the sheath potential. The influence of these collisions leads to number of additional peaks appearing at distinct energies in the spectrum.

1.3 Mechanisms of Dry Plasma Etching

Etching, in a microscopic sense, means removing atoms from a substrate by breaking bonds that attach them to their neighbours, which means overcoming an energy barrier (surface binding energy). There are four conventional mechanisms to modify or overcome this energy barrier in plasma etching: physical sputtering, chemical etch, ion inhibitor and ion energy driven etch. Figure 1.5 summarises schematically the four etch mechanisms by highlighting the species supplied by the discharge and the resulting etch effect (isotropic or anisotropic). One or more chemical reactions take place in each etching process. Types of reactions include oxidation-reduction (redox), complexation (reversible reaction of two dissolved species to form a third), and gas phase etching.

(i) Physical Sputtering

Sputtering is the process of ejecting atoms from a surface due to the bombard-

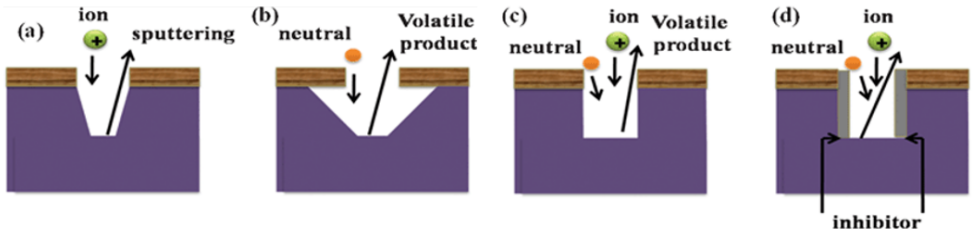

Figure 1.5: Four plasma etch mechanisms (a) Physical sputtering (b) purely chemical etch (c) ion energy driven etch (d) ion inhibitor etch [10].

ment of the surface by energetic ions. An atom ejects if, through the transfer of momentum, the atom accumulates enough kinetic energy in the upward direction to overcome the surface binding energy. The observed sputtering thresholds of common materials in semiconductor processing are on the order of 10's of eV, several times their surface binding energy. The large bombardment energy of ions is needed because the impact energy dissipates through a collision cascade of target atoms. Statistically, the atom hit with an initial ion strike is not removed, but rather a neighbouring atom is liberated or displaced through momentum transfer. The sputter yield, which is the number of atoms sputtered per incident ion, increases rapidly with energy up to a few hundred eV [4] and typically depends on the square root of the ion energy above a threshold; momentum transfer from incoming ion to surface atom results in mass-ratio dependency [2]. Even though sputtering is predominately un-selective, and the sputtering yields are generally low (on the order of one atom per incident ion), it is an anisotropic process and heavily depends on the ion angle of incidence to the target surface. Sputtering is also the only mechanism that can remove non-volatile products which is important for sputter deposition processes.

(ii) Purely Chemical Etch

For chemical plasma etch, the discharge etchant species chemically react with the surface to form volatile by-products in the gas phase. For example, in etching of Silicon, F atoms in gas phase react with the silicon substrate yielding a volatile etch by-product:

$$\mathrm{Si(s)} + 4\mathrm{F(g)} \rightarrow \mathrm{SiF_4(g)}$$

where (g) and (s) indicate gas and solid phase respectively. Chemical plasma etch

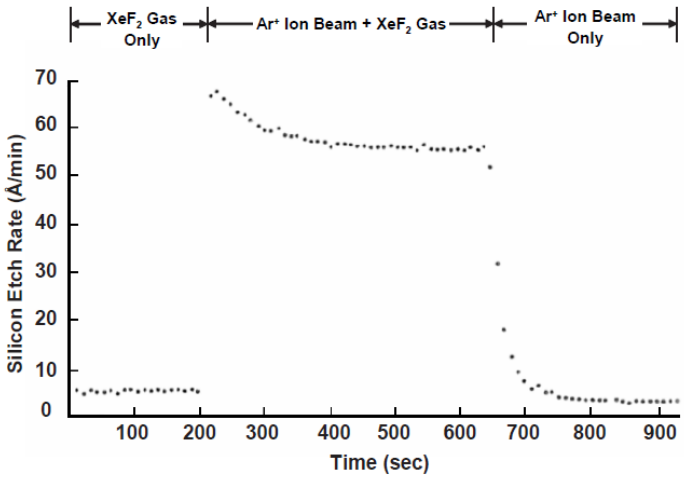

Figure 1.6: Ion-assisted gas surface chemistry using Ar^+ and XeF_2 on silicon [11].

is predominately isotropic because the etching species from the discharge hit the surface with a nearly uniform angular distribution. One case where anisotropic chemical etch occurs is if the target surface is a crystal, so the etching rate depends on the crystal orientation.

(iii) Ion Energy Driven Etch

Here, the discharge supplies both etchants and energetic ions to the surface. This mechanism can be more effective in producing etching by-products than physical sputtering or chemical etch alone. It is suggested that the etching is of a chemical nature, but the rate is determined by the energetic ion bombardment, thus indicating that there is an ion energy threshold. The combined effect of chemical and physical etching means that there is both selective and anisotropic (due to the directional dependence of the ion incidence) etching. This opens the concept of the selectivity and anisotropy trade off.

The important work done by Coburn and Winters [11] showed that the combined actions of both neutral gas etching and ion bombardment (i.e. ion energy driven etch) produced a much faster etch rate than the simple algebraic addition of the two. This result, shown in Figure 1.6, is the basis of modern day industrial etching.

(iv) Ion Inhibitor Etch

This mechanism involves the use of an inhibitor species. Etchants, energetic ions,

and precursor molecules that act as an inhibitor protective layer are supplied by the plasma discharge. The inhibitor species form a protective layer on feature sidewalls which help block etching and thus aid an increase in anisotropic etch. First off, the etchant used produces a high chemical etch rate of the substrate even without the inhibitor or the energetic ions. The inhibitor species tries to form a protective layer on vertical and horizontal surfaces, but the directional dependent injection of ions prevents the inhibitor species surviving on the horizontal surfaces due to sputtering. The chemically selective etchant then etches the horizontal surfaces that are not protected by the inhibitor. This phenomenon can be called sidewall passivation [12]. For example [13], in etching of Silicon, the addition of O_2 to SF_6 plasma forms an inorganic film (SiO_xF_y) on the Si surface such that etching directionality is controlled by desorption capabilities of etching passivation film and etching products by energetic ions.

1.4 Plasma Etch Sources and Technologies

1.4.1 Historical

Plasma processing tools are produced with electrical power of frequencies ranging from DC to microwave. DC discharges suffer numerous disadvantages for material processing, thus are mainly studied now for fundamental plasma concepts (or DC magnetron sputtering). They lack spatial uniformity, have low discharge current densities, are limited to conductive surfaces, and are sustained by secondary electron emission which restricts the electrode surface composition. On the other end, microwave discharges also have inherent problems such as charge build-up damage due to a high-degree of dissociation and charge accumulation on substrates [14].

Typically, industrial plasmas are produced with RF that is between the positive ion oscillation frequency f_{pi} and the electron (plasma) oscillation frequency f_{pe}. These frequencies are low enough to allow the electrons to respond to the electric fields but high enough to allow current through insulating layers. Due to

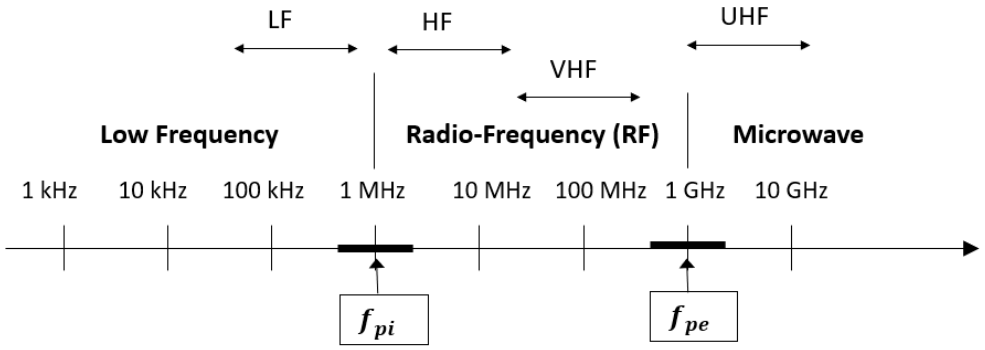

Figure 1.7: Range of possible excitation frequencies in terms of ion and electron plasma frequencies, f_{pi} and f_{pe} respectively. In the low frequency excitation, electrons and ions follow the oscillations of the electric field. In the RF range, the electrons only follow the electric field oscillations, while the ions are influenced by the average temporal local values of the field. Behaviours observed in RF are enhanced in microwave excitation.

government communication regulations, the classic, and most widely used, RF frequency in plasma processing tools is 13.56 MHz [1]. Figure 1.7 shows a frequency spectrum and depicts the typical range for electron- and ion- plasma frequencies. This figure also highlights the Very-High-Frequency (VHF) RF range, 30 - 300 MHz, and this section will later discuss the benefits of operating in this frequency range instead of the conventional 13.56 MHz.

In the early years of plasma etching, RF power was coupled capacitively to the plasma systems, resulting in the moniker Capacitively-Coupled-Plasmas (although initially, CCPs were solely known as Reactive-Ion-Etchers (RIE)). As the industry migrated to 200 mm wafers, high-throughput single wafer etchers with enhanced etching rates were needed in replacement of large batch RIE reactors. This meant there was a need for higher ion flux at the same sheath voltage, but with the same surface driven reactions. To achieve this, attention was directed to developing alternative high-density plasma sources such Inductively-Coupled Plasmas (ICP) and Electron Cyclotron Resonance (ECR) plasmas. Over the years, these sources, and other high-density source alternatives [15, 16] have

[1] 13.56 MHz is the centre frequency of the second ISM band. The industrial, scientific and medical (ISM) radio bands are defined by the ITU-R. the International Telecommunications Union. The first four ISM bands are: 6.780 MHz ± 0.015 MHz, 13.560 MHz ± 0.007 MHz, 27.120 MHz ± 0.163 MHz and 40.68 MHz ± 0.02 MHz

been developed with success for etching of metals and gate materials, however, they have mainly failed in the dielectric SiO_2 etching because of their low controllability and reproducibilty of complicated gas chemistries in oxide etching. This low controllability in ICPs and ECRs is because, by nature, they are high-density large-volume reactors, which means they have large gas-residence-times and highly dissociated gases. The resultant lack of larger moieties of molecular radicals causes a lack of passivation in the dielectric etch process and so ICP tools in general were incapable of achieving the high aspect ratio and high selectivity required by industry [17]. Therefore, CCPs have remained the preferred method for dielectric etching, where higher order complexities of C_xF_y species and surface layers are critical.

1.4.2 Capacitively-Coupled Plasmas (CCPs)

This section begins with a description of basic CCPs. Then, the advantages of CCPs driven at higher frequencies (into the VHF range) will be presented in terms of the discharge properties and resulting effects on substrate reactions. Extending beyond single VHF excitation, the benefits dual(2)-frequency CCPs will be introduced. Finally, the engineering problems associated with VHF excitation scaled to large reactors will be explored.

CCPs are possibly one of the simplest forms of RF gas discharges, whereby the plasma is excited by an electric field (an oscillating voltage) between two electrodes, shown in Figure 1.8 (left)[1]. This electric field set up by the oscillating voltage is perpendicular to the plane of the electrodes, so we say (at low RF frequencies) that the power coupled into the plasma is purely capacitive.
The capacitance in CCP is not actually between the electrodes directly, but rather between the electrodes and plasma, i.e. across the electron-free sheaths, that are acting as a capacitive barrier.

The impedance of the two capacitive sheaths is equal to the sum of their

[1]The blocking capacitor shown between the RF source and powered electrode results in no net current flow and as a result the plasma potential must approach the powered electrode potential for a brief period in RF cycle to allow electrons reach the powered electrode.

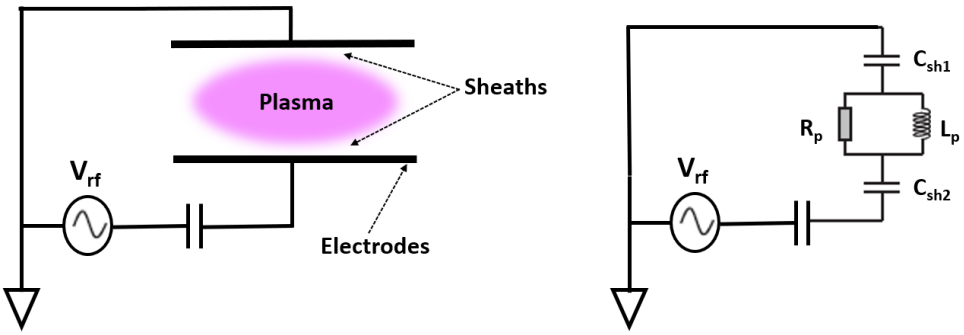

Figure 1.8: Schematic diagram of a capacitively coupled plasma discharge (left) and a simplified equivalent circuit (right).

individual impedances:

$$Z_{sh1} + Z_{sh2} = Z_{sh} = \frac{1}{j\omega C_{sh}} \tag{1.18}$$

where ω is the RF excitation frequency, and C_{sh} is the sum of the two sheath capacitances.

In single-frequency operation, one of the electrodes is powered by an RF generator through an appropriate matching network, while the other electrode is grounded. The CCP schematic shown in Figure 1.8 is that of a symmetric system; both electrodes are of equal area. Let us take the case of an asymmetric system, where the grounded electrode is larger. When the smaller powered electrode exhibits a positive potential (during a fraction of the RF cycle), it will rapidly collect high mobility electrons. At the same instance, the counter electrode will collect heavy ions, but at a much smaller rate. The relatively larger influx of electrons causes a negative bias to develop on the smaller powered electrode, which subsequently becomes larger cycle by cycle, until a time-averaged steady-state is reached. The consequence of this negative DC self-bias developing on the smaller electrode facilitates the production of higher ion energies relative to the larger grounded electrode. In his way, variation between between high and low ion energies for a given frequency can be achieved with asymmetrical CCPs.

1.4.2.1 Very-High-Frequency (VHF) driven CCPs

Surface processing in CCPs is dominantly driven by a synergy of ion energy, ion flux and plasma chemistry. Despite developments in alternative CCPs (such as Magnetically-Enhanced-Reactive-Ion-Etcher (MERIE)[18] and Dipole-Ring-Magnet[19] reactors), to improve control of ion energies and charge damage, it became clear that increasing the frequency beyond the traditional 13.56 MHz into the VHF band affects all these crucial parameters in a way that is highly desirable for material processing, and specifically etching. This is a result of changes in RF power coupling due to the capacitive sheaths, as shown in Equation 1.18, such that with increasing frequency and constant power, voltage drops resulting in ions with lower energy from the reduced sheath impedance, and current increases which provides more ohmic (I^2R) power to the plasma, and have higher density and higher ion flux.

Several simulation studies have been performed in the past few decades for plasmas operating in the VHF band [20, 21, 22, 23]. Using particle-in-cell/Monte Carlo method, Surrendra et al [21] simuated CCPs in helium at frequencies from 20 to 120 MHz. Under constant applied voltage, electrode gap, and pressure conditions, they found that the plasma density and ion current is enhanced by increasing the driving frequency with minimal effect on the maximum ion energy.

The EEDF (Section 1.2.5), which drives the plasma chemistry and determines radical densities, is also strongly affected by an increase in operating frequency [24, 25]. At a fixed pressure of 100 mTorr in Ar, Figure 1.9, from [26], shows the transition in shape from a convex Druyvestyn toward a Bi-Maxwellian type with a concave nature with increasing frequency, from 13.56 MHz to 50 MHz. This is attributed to a change from collisional ohmic heating to dominant stochastic heating which creates more ionisation in the plasma bulk. A balance between the production and loss of electrons leads to a lower value of effective electron temperature in the VHF range. But the nature of a cold bulk and hot tail indicates a highly non-thermal plasma, with the neutral gas at a temperature similar to the chamber walls (ions ≈300 K warmer) and electrons at very high temperatures of 1000s K. This has been experimentally investigated [27, 28, 29] with Optical Emission Spectroscopy (OES). Results of very high vibrational temperature T_{vib}

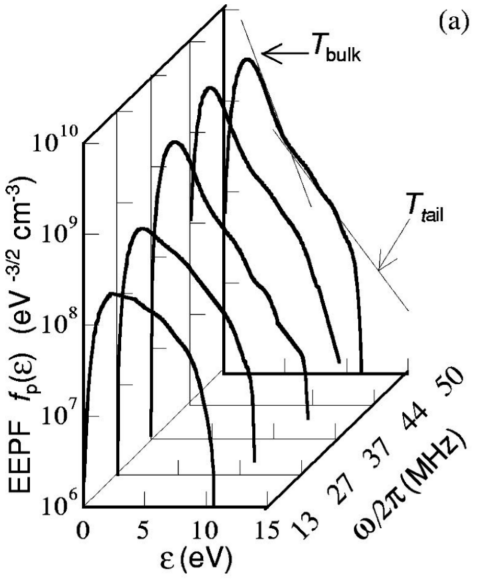

Figure 1.9: EEDF transition from a Druyvesteyn to Bi-Maxwellian with increasing frequency. Argon 100 mTorr and RF voltage = 80 V_{pp} [30].

with low rotational temperature T_{rot}, suggests that the energy from the low energy electrons is preferentially coupled into vibrational states. Sugai et all [30] noted that CCP discharges can exhibit a Bi-Maxwellian EEDF in some gases at particular low pressures, whereas VHF CCPs reveal a Bi-Maxwellian EEDF irrespective of gas type or pressure (initial experimental reports from Godyak [6]).

Several experiments and studies have also reported the advantages of using VHF for deposition and etching in the semiconductor industry. For example, Howling et al [31] measured the deposition rate of Si films vs frequency and showed that the deposition rate is 3x higher at 70 MHz than at 13.56 MHz, with comparable film optical qualities. Recently, Monaghan and Ellingboe [29] produced nano-crystalline silicon layers at a high deposition rate (exceeding 0.75 nm/s) with a high degree of crystalline fraction uniformity in a large-scale reactor. This work employed a multi-electrode CCP source that will be discussed later.

From an etching perspective, Samukawa et al [14] reported the development and use of a Ultra-High-Frequency (UHF) plasma source, 500 MHz, with spoke-wise antenna for large-scale 200 m wafer etching. Their study highlighted the benefits of increasing driving frequency but noted that there is a certain cut-off

point where the advantages of VHF/UHF no longer apply. Specifically, with microwave ECR (2.45 GHz)[1], the pressure range is limited, electron temperature begins to increase and there is a non-linear dependence of electron density with power, as shown in Figure 1.10.

In summary, increasing driving frequency into the VHF band (30-300 MHz) favourably affects crucial process parameters for material surface processing. Namely, the sheath impedance drops (Equation 1.18) which is equivalent to lower ion energies. The reduced sheath width with increasing frequency also causes the ion motion to be less collisional which is important for maintaining narrow ion energy spread in the IED. The EEDF, responsible for driving plasma chemistry and subsequent surface chemistry, is altered with increasing frequency. There is a transition to a bi-Maxwellian electron distribution, with a distinct low-energy cold-bulk and high-energy hot-tail, which is associated with enhanced stochastic heating, increasing dissipated power into the plasma resulting in higher densities. Characteristic of a bi-Maxwellian EEDF at VHF is a highly non-equilibrium discharge; very high vibrational temperatures with low rotational temperatures. This facilitates favourable chemical activation whilst maintaining low operating temperatures.

The ion-assisted chemical etching process (Section 1.3) requires ions with just enough energy to weaken the chemical bonds at the surface, but also with sufficient fluxes of ions to make the process worthwhile. However, to increase ion flux (plasma density), the power needs to increase, which in general also increases the ion energy. In this sense, for a single-frequency CCP, a limit is placed on the ion flux, and therefore the etch rate before surface damage occurs. Furthermore, asymmetrical geometry discharges are very hard to achieve for large-area applications such as solar cells and flat panel displays, where minimizing plasma volume to control gas-residence-time and plasma chemistry results in nearly symmetric systems, which curtails their advantage to control higher and lower ion energies limits.

To obtain independent control of both the ion energy and ion flux, dual-frequency plasmas have been developed with success [32, 33, 34]. In these systems,

[1]Typically 2.45 GHz reactors are not CCP, but are rather Electron Cyclotron Resonance (ECR) reactors

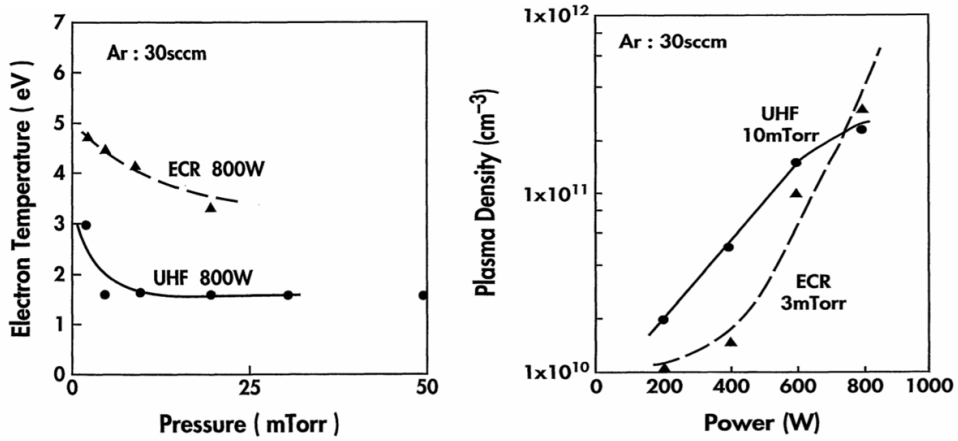

Figure 1.10: Comparison between UHF (500 MHz) and ECR (2.45 GHz) Ar discharge. Effect of pressure on electron temperature (left) and effect of power on plasma density (right). Reproduced from Samukawa [14].

the upper frequency tends to dominate plasma formation and the lower frequency dominates the lower electrode sheath voltage. Typically upper frequencies in the HF range (3-30 MHz) and lower frequency in the LF range (0.3-3 MHz) are used [35, 36]. For decoupled operation between ion-flux and ion-energy, a sufficient separation between the operating frequencies is required; a ratio of lower to upper frequency that is $\lesssim 0.1$ [37].

In addition to the desire of increasing frequency for plasma production, and exploiting advantages of dual-frequency, there is an increasing demand for larger surface processing area, due to larger wafers, flat panel displays and other industrial applications. However, the dovetailing of VHF and large area processing poses significant technical and engineering difficulties which we will discuss.

Recall from earlier, that for CCPs operating at normal low frequencies, the power coupled is purely capacitively because the electric (E-field) is perpendicular to the electrodes. From a modeling perspective, this means that the electrical characteristics of the plasma are only governed by Poisson's equations. This is not the case when CCPs are operated at VHF, and we will see how there can be both capacitive and inductive coupling. As a result, they cannot be described simply by a conventional electrostatic model.

We begin by noting the effect of driving frequency on the skin depth, for

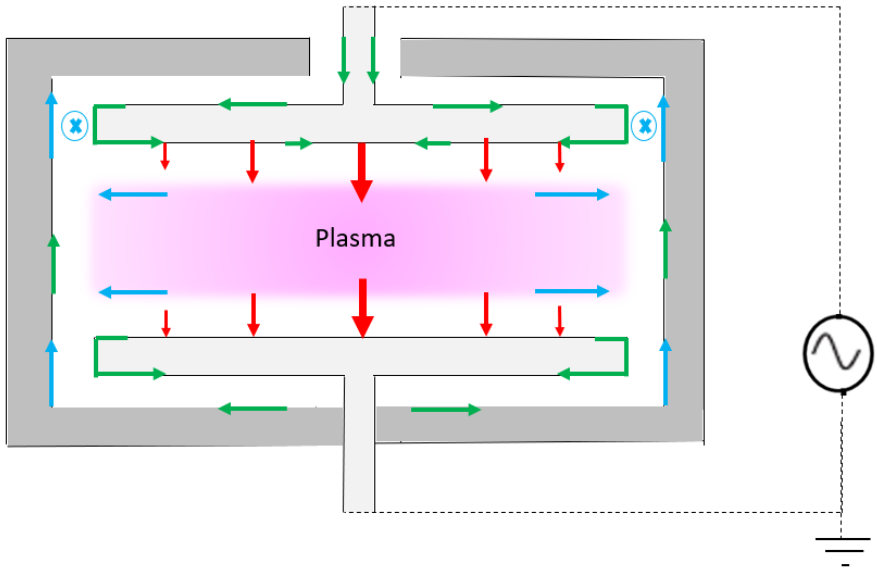

Figure 1.11: Resulting currents and magnetic dipoles in a conventional large electrode VHF CCP. Green arrows are electrode currents, blue are inductive image currents, red are capacitive displacement currents, and blue vector crosses are magnetic dipoles.

current in metals (electrode). The skin depth is given by:

$$\delta = \sqrt{\frac{2\rho}{\omega\mu}} \tag{1.19}$$

where ω is the frequency, and ρ and μ are the resistivity and permeability of the conductor respectively. The skin depth for VHF is much smaller than the thickness of the electrode ($\delta \approx$ microns compared to $\approx$ mm thick electrode). Therefore, the currents of the VHF electromagnetic wave travel along the surface of the electrode. Let us consider the VHF current path, which flows radially inward on the plasma-facing surface of the upper electrode shown in Figure 1.11 [1]. This electrode has no direct connection to ground, so there occurs a point of effective electrical termination, at the centre of this top electrode (furthest point from the current supply). The counter-propagating waves (traveling radially inward to the centre from opposing electrode edges, shown in Figure 1.11)

[1] Length/size of arrows are representative of the magnitude of currents

constructively interfere and produce a standing wave which has a zero in current and voltage maximum at this centre. As this standing wave characteristic length (which is 1/4 wavelength of the RF signal) becomes comparable to the electrode length; the current and voltage non-uniformities become significant, causing plasma non-uniformities. The E-field at the electrode centre, E_z, is purely capacitive and drives maximum displacement across the sheath, because the voltage (from standing wave) is at a maximum, but the current is approaching zero. On the other hand, the E-field at the plasma sheath edges has a radial inductive component as well as an axial capacitive one. This inductive E-field E_r, parallel to the electrode, occurs because of the maximum current at the edges, which induces image currents, that draw current around the edges of the discharge. The strength of these image currents depends of the plasma skin depth and the discharge gap. For collisionless plasma, the plasma skin depth is given by:

$$\delta_{pl} = \frac{c}{\omega_{pe}} \tag{1.20}$$

where ω_{pe} is the plasma frequency given by the Eqn 1.4, and is $\sim$cm for densities of $\sim 10^{10} cm^{-3}$. Additionally, the grounded chamber (return) current flows in opposite direction to the currents coming around the powered electrode edge, and thus sets up a magnetic dipole between the electrode and the chamber. This magnetic dipole in turn drives inductive currents in the plasma, in the same direction as the image currents produced by the electrode oscillating current. This increases the non-uniform effect due to the current density in the electrode increasing with electrode "radius" ($I \propto r$).

It is clear that power non-uniformities (when the 1/4 wavelength becomes comparable to the electrode length) are the result of radial variations in capacitive coupling, dominating at the electrode centre, and inductive coupling, increasing at the electrode edge. The non-uniformities are transferred differently by non-local power deposition at lower pressure, compared to local power deposition at higher pressure. This will be explored further in the experimental section.

Over the years, there have been engineering attempts at suppressing the electromagnetic non-uniformities in VHF CCPs. Some examples include the use

of Gaussian shaped electrodes [38, 39], and graded conductivity (divided) electrodes [40, 41]. The former example is specifically for a cylindrical geometry and is dependent on a consistent plasma refractive index, and as such has limited flexibility once implemented. The graded conductivity electrodes can pose problems, in that all the electrodes are driven by the same power supply (i.e. without splitting). This means that the electrodes are not electrically isolated and can result in localised breakdown in front of only one electrode. Furthermore, net current is still driven through the substrate to ground.

A successful solution for VHF CCP operation is the use of a multi-tile electrode system with a unique Power-Splitting-Line-Driver (PSTLD) that provides independent, equal, push-pull power to each of the pair of tiles. The use of "small" tiles in an array mean that the aforementioned electromagnetic effects within a tile are minimised. The standing wave wavelength can be estimated as [4]:

$$\lambda_{sw} = \frac{\lambda_0}{\sqrt{1 + \Delta/2s}} \tag{1.21}$$

where λ_0 is the free space wavelength, s is the sheath thickness, and Δ is either the half plasma thickness or the plasma skin depth; whichever is smaller. For 162 MHz, this wavelength $\lambda_{sw} \approx 49$ cm, which means that electromagnetic effects are minimised for tile dimensions of 10 cm ($\lambda_{sw}/4 > R$) in the PASTIS reactor, and for tile dimensions of 4 cm in *Starchief*. Further detail on the power coupling mechanisms in a multi-tile VHF system, and specifically the PASTIS reactor will be given in Chapter 3.

So far, improvements from the plasma-reactor perspective have been discussed. In the following section we discuss the technology of Atomic-Layer-Etching that can facilitate future scaling, and improve on the shortcomings of continuous etch mechanisms.

1.5 Atomic-Layer-Etching Technology

ALE is a technique that uses sequential reactions to remove atomically thin layers of material, where at least one of the reactions is self-limiting to control the amount of removed material per full-cycle. The self-limiting nature of ALE fundamentally differentiates it from existing etch technologies in CCPs that facilitate atomic precision. Using conventional plasma etching, even with an inhibitor layer, it is difficult to obtain reliable atomic layer precision because the adsorption of the inhibitor layer (also the reactant layer) and the reaction of ions occur simultaneously in a somewhat uncontrolled, non-self-limiting manner.

The basics of an ALE cycle is as follows: in the first half-cycle, a modification step (step 1) occurs which forms a reactive layer on the substrate. In the second half-cycle, a removal step (step 2) involves removing this reactive layer as well as the top (mono)layer of the underlying substrate. Using ions in this removal step allows for anisotropic etching that is critical for deep narrow structures.

ALE is somewhat analogous to its predecessor Atomic-Layer-Deposition (ALD), which has become productive enough to advance to mainstream technology implemented in industrial large-scale manufacturing. ALE technology is still in the early stages, but even though the mechanisms are more complex than its deposition technique counterpart, ALE is proving itself one of, if not the most, promising techniques for achieving the low process variability necessary in the atomic-scale etch era.

Figure 1.12 below highlights the benefits of decoupling the reaction steps. Ultimately, in continuous etch processes, the paradox is that we need a reactive layer that is formed from reactive gas species and low energy ions, but this layer is produced by the same high energy ions that are required to perform the etch in the first place. The separation of the reaction steps allows for ion energy variability in each reaction. In the ALE illustration in Figure 1.12, a reactant layer forms in the first step after chemical reactants are delivered to the substrate. This reaction step is not necessarily self-limiting; this is discussed further in the following section. Following energetic ion bombardment in the second ALE step, the reactive layer and underlying substrate is removed in a controlled self-limiting manner. It should be noted from the same Figure 1.12, that the resulting surface

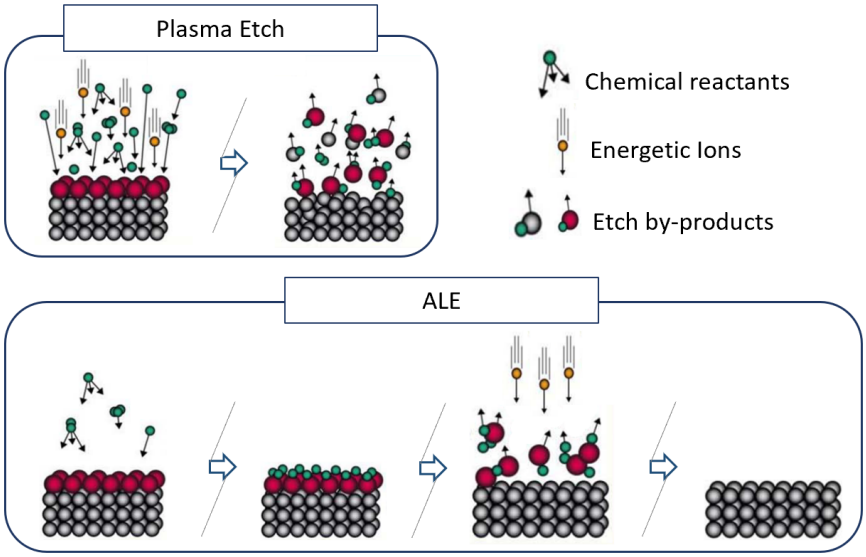

Figure 1.12: Schematic of the comparison between conventional plasma etching and ALE. The chemical reactants are supplied simultaneously and non-interrupted in conventional processes, where as in the ALE scheme, they are alternated.

after an ALE cycle is near pristine, contrary to continuous etch. This is because stoichiometry can be maintained in ALE [1] which provides atomically smooth surfaces, whereas continuous etching has the tendency to alter stoichiometry as one element is favourably moved relative to another [42, 43, 44].

1.5.1 History of ALE

The earliest reports of ALE trace back to 1988 [45], with most of the early focus on isotropic ALE [46] as a thermal processes [47]. Early reports using thermal reactions claimed long process times, up to 5 minutes (per cycle), with corresponding etch rates of ∼0.1-0.01 nm/min. Soon after, etch-per-cycle (EPC) was aptly adapted instead of "etch rate" because the etch rate is not continuous in time. Reports in the early 1990s claimed self-limiting reactions on Si using Cl_2

[1] It has been reported that the stoichiometry of the reaction mixing layer is much easier to control with Si etch using Cl_2 chemistries compared to dielectric etching using multi-component FC-polymer layers

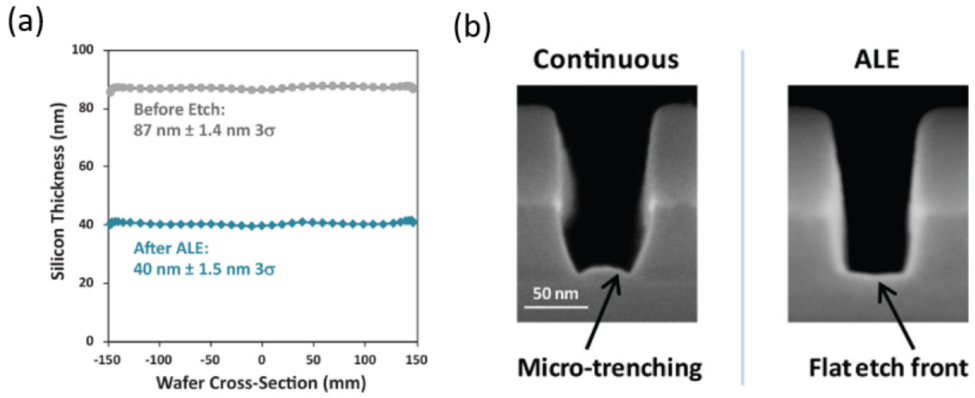

Figure 1.13: (a) Uniformity across a blanket silicon wafer before and after ALE process (b) SEM images of polysilicon trenches etched under comparable process conditions [56].

and Ar^+, but the EPC were less than one atomic monolayer [48, 49]. The early experimental Si ALE in the 1990s was paralleled with modeling efforts that include computation techniques such as molecular dynamics, kinetic Monte Carlo simulations, Density Functional Theory, and feature scale simulators [50, 51, 52, 53]. Athavale and Economou simulated ALE of one atomic layer of Si (0.14 nm), followed by experimental evidence in a Helicon source with both self-limiting modification reaction and etching removal [51, 54].

Some later work in the 2000s aimed to reduce charge related damage by using an Ar neutral beam, again for Si etching [55].In 2013, Kanarik et al [56] validated ALE behaviour in a commercially available reactor by showing atomically smooth Si surfaces, flat Si etch front (Figure 1.13), and with an EPC of 0.7 nm/cycle. This EPC corresponds very well to simulation results published the following year by Brichon et al [57] that estimated 0.5 nm reactive layer thickness. Their simulation work obtained a self-limiting reactive layer by controlling ion energy of under 10 eV. This reactive layer thickness is significantly thinner than the mixed layer in continuous plasma etching [55, 58].

A variety of self-limiting mechanisms, for both the modification step and the removal step, have been experimentally investigated. Modification mechanisms include chemisorption, deposition, conversion, and extraction, while removal mechanisms include thermal desorption, particle bombardment, and chem-

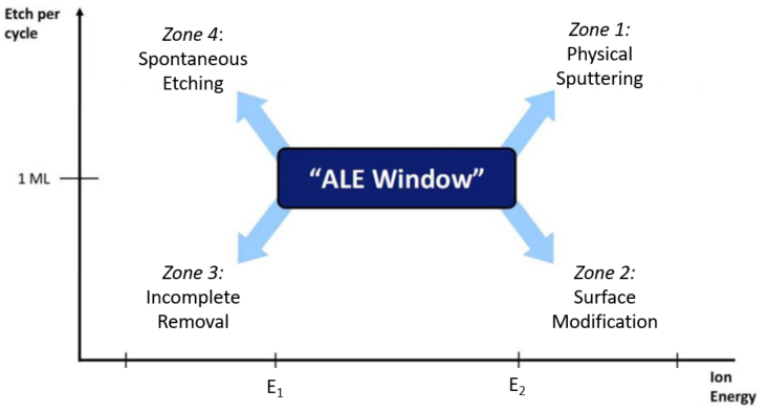

Figure 1.14: Illustration of the ALE window; etch rate of an ideal process as a function of removal step irradiation energy.

ical reaction. All the above reaction mechanisms are explored based on the so-called ALE window, which is similar to the well-reported counter ALD window. The ALE window [59], shown in Figure 1.14 is bound by E_1, which is the threshold energy to create reactive species on the surface capping layer, or to initiate reaction of the reactive layer with substrate, and E_2, which is the threshold energy for initiating reaction with any other material on the substrate, or the substrate itself. Outside of this window, there are 4 zones which exhibit non-ideal behaviour, namely physical sputtering, surface modification, incomplete removal, and spontaneous etching.

Consider the case of Si ALE using Cl_2 and Ar^+ ions. Here the modification mechanism is chemisorption, which is the mostly widely used mechanism. A reactive (chemisorbed) surface layer weakens the underlying substrate bonds. Specifically, a chemisorbed layer is formed on the surface; Cl diffusivity into the Si crystal is low, such that the formed $SiCl_x$ surface layer has a low sticking fraction for Cl_2 and therefore inhibits further additional Cl uptake. The sole reason for using plasma in the adsorption step is to speed up the process, because instead of waiting for the Cl_2 molecules to dissociate before reacting with the dangling silicon bonds, the Cl_2 molecules are readily dissociated in plasma to produce radicals that quickly react with the surface. Full surface saturation is reported to take 8-40 seconds [48] under typical thermal conditions. By using plasma, the chemisorption is reported to saturate in less than 1 second in the case of silicon

[60], due to the increase in adsorption rate constants by several orders of magnitude.

In step 2, removal of the $SiCl_n$ etch by-product is then obtained from energetic ion bombardment (usually by Ar^+ ions), with energies that are high enough to remove the $SiCl_n$ layer, but low enough to avoid physical sputtering of Si. Specifically, the work by Athavale and Economou [51, 54] found for a 50 eV Ar^+ bombardment, a dose of 1.6x10^{16} ions cm^{-2} was required to remove one monolayer of Si. There was no particular attention paid to fast switching gases in these earlier studies, thus relatively long times, ∼100 s, were needed for each ALE cycle.

1.5.2 Focus on SiO_2 ALE

ALE of Si has been well reported and is now quite well understood. The case of SiO_2 ALE, however, is not fully understood and still lacks extensive experimental evidence. Fluorocarbons are used for ALE of SiO_2, where, (in step 1 of the ALE cycle) an overlying fluorocarbon polymer layer is deposited by C_xF_y radicals. This is the deposition-based modification mechanism[1]. The fluorocarbon (FC) polymer layer facilitates chemical etching of the SiO_2 as the C aids removal of the O_2, while the F helps elimination of the Si, resulting in a process:

$$SiO_2(s) + 2(CF_2)_x(g) \rightarrow SiF_4(g) + CO_2(g)$$

Indeed, fluorocarbons have been used extensively in manufacturing for etching of silicon dioxide (and other dielectrics; Si_3N_4). The fluorine-based chemistry is needed because the reaction is exothermic, however fluorine-rich environments result in a favourable etch of Si over SiO_2. A breakthrough paper was published by Heinecke in 1975 [61], detailing that the use of higher order fluroalkanes, or

[1]To clarify a possible confusion regarding deposition-based ALE; it is indeed similar to the so-called Bosch process in that they both use alternate deposition and etching steps. However, the Bosch process is usually optimized to protect the feature sidewall and to remove much more than just the reactive layer in each cycle.

the addition of hydrogen, improves the SiO_2/Si etch rate ratio [1]. It was later found [62] through careful X-ray spectroscopic and ellipsometry studies, that high selectivity of SiO_2/Si and SiO_2/Si_3N_4 etch rate ratios were observed when the fluorocarbon polymer film thicknesses on the SiO_2, Si_3N_4, and Si were 1,5 and 6 nm respectively.

The energy threshold for SiO_2 removal is higher than Si due to the difference in thickness of FC reaction layers. This has led to desired selectivites for Back-End-of-Line (BEOL) in traditional continuous processing. However, in the ALE regime, it is not as straightforward because the reaction layer is confined to a thickness appropriate for penetration by the Ar^+ ion for single monolayer removal.

In the instance of SiO_2 ALE, simulation work appeared many years before relevant experimental data. Deposition-based ALE was first proposed by Agarwal and Kushner [50]. Their computational investigation utilised the well-known Hybrid Plasma Equipment Model (HPEM) [63] to obtain reactor scale plasma properties and produce reactant fluxes to the substrate. In this work, SiO_2 ALE was studied in a MERIE reactor using Ar/C_4F_8 chemistry (as well as Si ALE using Ar/Cl_2 in a conventional 13.56 MHz ICP). They emphasized that careful control of chemistry and ion energy during the passivation and etching steps were crucial for successful implementation [2] Rauf et al [52] used Molecular Dynamics (MD) simulations to examine the possibility of realising ALE using nanometer-scale FC passivation of SiO_2 and Si, using low energy CF_2^+ and CF_3^+ ions, followed by Ar^+ ion etching with energies less than 50 eV ($\sim$ the physical sputtering threshold for SiO_2).

It wasnt until 2014, that Metzler et al [64] showed the first experimental evidence of SiO_2 ALE. In this work, 1.5 s pulses of C_4F_8 were injected to form a 0.5 nm layer, followed by Ar^+ ion bombardment with energies at 25 eV, provided by a continuous-wave (CW) plasma (13.56 MHz ICP), with a 3 MHz CCP bias

[1] Essentially the polymerisation overwhelms the chemical etching of Si(or other resist), whereas the oxygen in the SiO_2 fights off the polymerisation by combining with the carbon to form the volatile products such as CO and CO_2

[2] Paper also claimed that ALE will be inevitably too slow, and suggested that either it should be used in succession of a continuous etch, or develop regime that involves the self-limiting reactions to occur in single gas mixture.

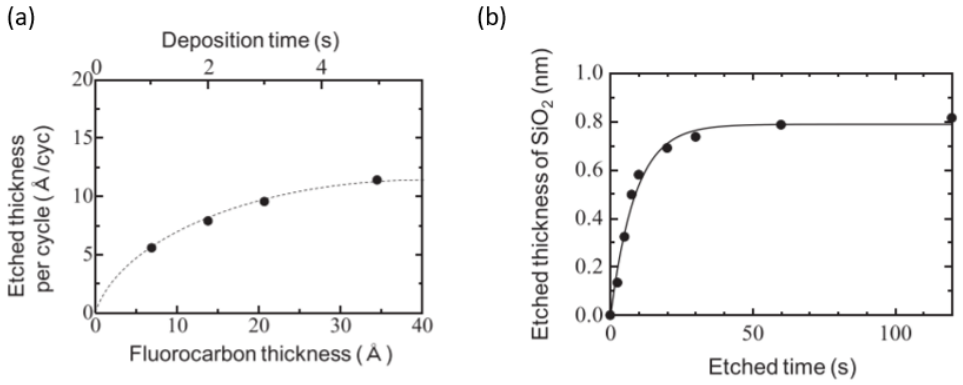

Figure 1.15: (a) EPC dependence on FC deposition time and (b) SiO_2 thickness changes (etched amount) during single cycle following FC deposition of 2 s [66].

(125 mm diameter) substrate. An etch rate of 0.25 nm/cycle of SiO_2 was reported. Their later report [65] in 2016, demonstrated selective etching of SiO_2 to Si_3N_4 by adjusting ion energy, etch step duration, and FC film thickness. This selectivity is possible because the presence of C promotes O removal but hinders etching of Si and Si_3N_4. In the same year, Tsutsumi et al [66] used a 60 MHz CCP system to deposit a much thicker FC film (0.69-3.45 nm) followed by an O_2 plasma. The EPC was shown to depend on FC deposition time, as shown below in Figure 1.15(a), but self-limiting etching behaviour was demonstrated, evident from the plateau region after 40 s in Figure 1.15(b).

In a further effort to reduce the residual contaminants that remain on Si surfaces after ALE cycles of SiO_2, Metzler et al [67] added H_2 to the Ar discharge in the removal step. They showed a successful reduction in both the carbon and fluorine content, albeit a net loss of 0.4 nm of underlying Si. In 2017, Economou et al [68] used two distinct (remote) ICPs sources, connected to a single processing chamber via gate-valves, such that the substrate is not immersed directly in the plasma. They used a CF_2 rich beam, generated from C_4F_8 plasma, to form a $\sim$0.8 nm FC film. Afterward, a 20 s Ar^+ ion bombardment with energies at 130 eV (produced from the second ICP reactor) was introduced, and an EPC of 0.19 nm/cycle was achieved. Also in 2017, Hudson and Agarwal claimed a much thinner FC film growth of 0.38 nm, from a 2 s C_4F_8 plasma. Following a 30 s Ar^+ ion bombardment, an EPC of 0.3-0.4 nm/cycle was achieved, but with the

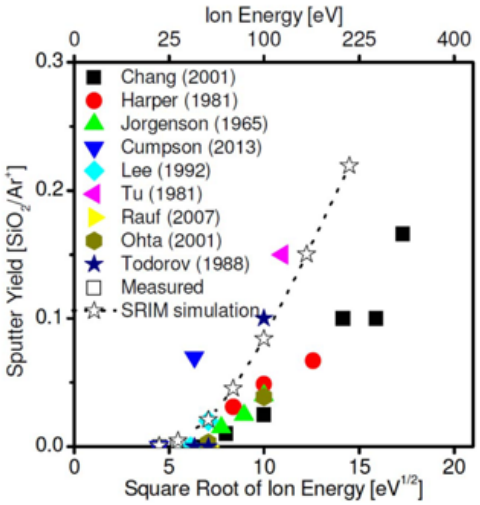

Figure 1.16: Review of literature data of physical sputter yields of SiO_2 vs Ar ion energy [69].

disadvantage of a reported CF_x build up on the reactor walls.

It has been observed [69] that processing near the energy thresholds for physical sputtering is necessary for self-limiting behaviour in the *removal* half-cycle of ALE. Figure 1.16 shows a review of the literature data of physical sputter rates for SiO_2 versus Ar^+ ion bombardment energy (nominally reported as sputter yield vs square root of ion bombardment energy). The threshold for physical sputtering of SiO_2 is ~45 eV (range between 30 and 50 eV).

It's evident that the implementation of ALE requires extreme control of the IED, but the ability to tailor the energy of ions to the level of precision needed for monolayer reaction control is not straightforward. Conventional ICP plasmas have an intrinsic plasma potential that produces an ion energy which is greater than the threshold for self-limitation. Referring to the ALE process window described previously in Figure 1.14, this means that the process window is exceeded and either selectivity loss or surface modification can occur [70]. Furthermore, ECR microwave systems can have plasma potentials below threshold, but high amounts of UV and VUV photons which prevent self-limiting behaviour [71]. These issues again reinforce the attractiveness for using alternative VHF CCP sources that can produce lower ion energies while also reducing VUV photon damage.

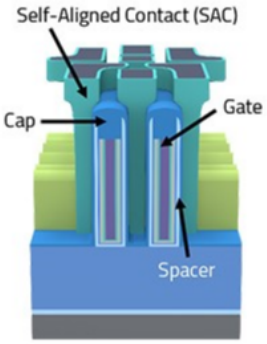

Figure 1.17: Illustration of a Self-Aligned-Contact (SAC) [73].

There are many challenges facing the continuous progress of plasma etching; mainly uniformity, defects, surface precision, and sticky/non-volatile etch materials [72]. Indeed, there is not one single etching solution that can encompass all these critical issues.

For example, Self-Aligned-Contacts (SACs) rely on the ability to etch out an oxide, namely SiO_2, without eroding a thin nitride, Si_3N_4, etch stop layer that defines a via contact hole (see Figure 1.17). This is desirable when the source/drain are extremely close to the gate, and thus SACs avoid the risk of misaligned printed contacts which could cause shorting between the source (or drain) and gate. It has been shown that ALE can increase selectivity by a factor of 2 over RIE, while maintaining directionality and layer-by-layer removal [64]. The driving factor for ALE therefore is not only surface precision blanket etch, but particularly precision in etch selectivites.

1.6 Thesis Layout

This thesis is comprised of five chapters. Chapter 1 provides a brief background in plasma theory; the progression and development of plasma etch sources are reviewed, and finally, the principles of ALE, and developments to date are discussed. Chapter 2 describes the experimental plasma reactors used in this work;

PASTIS, a single-frequency VHF plasma source and *Starchief*, a 2-frequency system (VHF plasma source + 27 MHz bias at wafer). Subsequent sections discuss the background theory and specific experimental details of each plasma and surface diagnostic employed. Chapter 3 presents results from the PASTIS reactor, and describes plasma dynamics of VHF multi-tile discharges and RF power coupling mechanisms associated with VHF and differential power delivery. Chapter 4 presents results from the *Starchief* reactor. The effects of VHF and low-frequency (LF) power coupling on plasma parameters are investigated, and a self-limiting fluorocarbon-based ALE process of SiO_2 is demonstrated in the large-area, low volume dual-excited reactor. Chapter 5 summarises the results presented in the thesis and provides suggestions for future experimental work.

Chapter 2

Experimental Set-up and Diagnostic Techniques

Contents

This chapter describes the plasma reactors used in this work; PASTIS, the single-frequency CCP source (section 2.1), and *Starchief*, the dual-excited CCP source (section 2.2). Subsequent sections discuss the plasma diagnostics used in both PASTIS and *Starchief*, specifically; electrode current and voltage probes (section 2.3), resonance hairpin probe (section 2.4), planar flux probe (section 2.5), energy resolved mass spectroscopy (section 2.6), and optical emission spectroscopy (section 2.7). Finally the surface diagnostics, Ellipsometry (section 2.8) and X-Ray Photoelectron Spectroscopy (section 2.9) are described. Each diagnostic section outlines the background theory and specific experimental details.

2.1 Description of PASTIS: single-frequency 162 MHz VHF CCP

The PASTIS plasma reactor source is shown in Figure 2.1, and accompanying labeled photograph in Figure 2.2. The upper, powered, multi-tile electrode of the source consists of a 3 x 4 array of 10 x 10 cm square aluminum tiles separated by 1 cm wide alumina, such that the resulting electrode size is 45 x 34 cm. The plasma discharge gap is 5.5 cm. A dielectric material is used at the back of the electrode to insulate the multi-tile electrode from the grounded plate. The plasma boundary opposite the electrode is grounded, albeit with optical flanges and a turbomolecular pump. The four walls of the chamber are insulated with 10 mm thick dielectric "skirts" as shown in Figure 2.1.

The RF power is supplied by a 162 MHz Advanced Energy Ovation generator to a matching unit and coupled to a Power Splitting Transmission Line Driver (PSTLD). The PSTLD consists of two concentric metal cylinders forming a co-axial transmission line which is terminated by a conductive end plate forming an electrical short as shown in Figure 2.3. RF current is driven along the central conductor with opposite phase image currents in the outer conductor, and current standing waves are formed on this central and outer conductor that are 180° out of phase (the transmission line length is at least 1/4 of the RF electrical wavelength so that all electromagnetic amplitudes are evident). The opposing current standing waves result in an oscillating magnetic field produced in the azimuthal direction in the cavity between the two cylinders. Coupling loops are inserted into this cavity through the end plate furthest from the RF input such that the magnetic field inductively powers the coupling loops that insect the magnetic flux. A time varying voltage is set up in the coupling loops as per the Maxwell Faraday equation.

$$\nabla \mathrm{x} E = -\frac{dB}{dt} \tag{2.1}$$

The coupling loops drive push-pull power to the multi-tile electrode system via twisted pair transmission lines; each loop forms a pair of outputs. The PSTLD

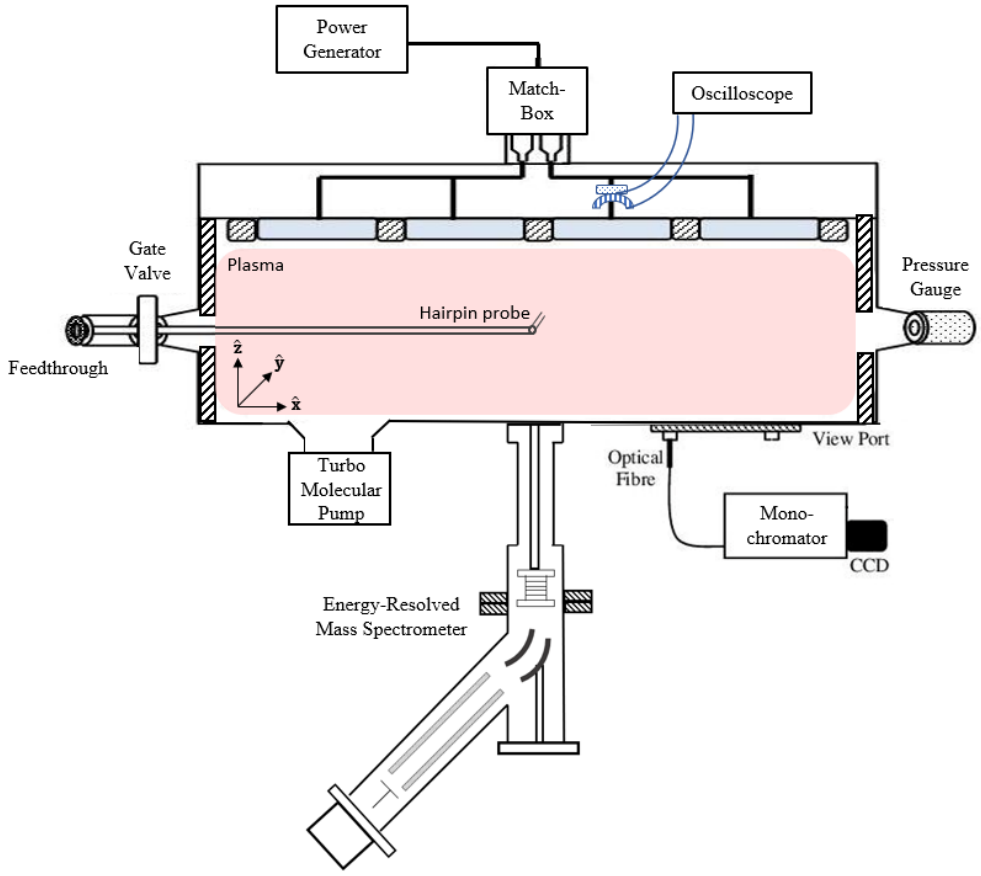

Figure 2.1: Side view of the PASTIS experimental set-up along with diagnostic probes and detection systems, not to scale.

provides fully differential RF power to each of the 6 pair outputs (12 tile electrodes) in the 2-dimensional array. More detailed discussion of the PSTLD can be found in [74]. For all presented results in Chapter 3 , tiles are powered in checkerboard (push-pull) configuration, meaning that each tile is 180° out of phase from its neighbouring tiles. Gas is introduced to the chamber through a shower-head structure in the tiles and flow is controlled by mass-flow-controllers (MFCs). The chamber pressure is regulated with an automated gate valve above a turbomolecular pump backed by a rotary pump.

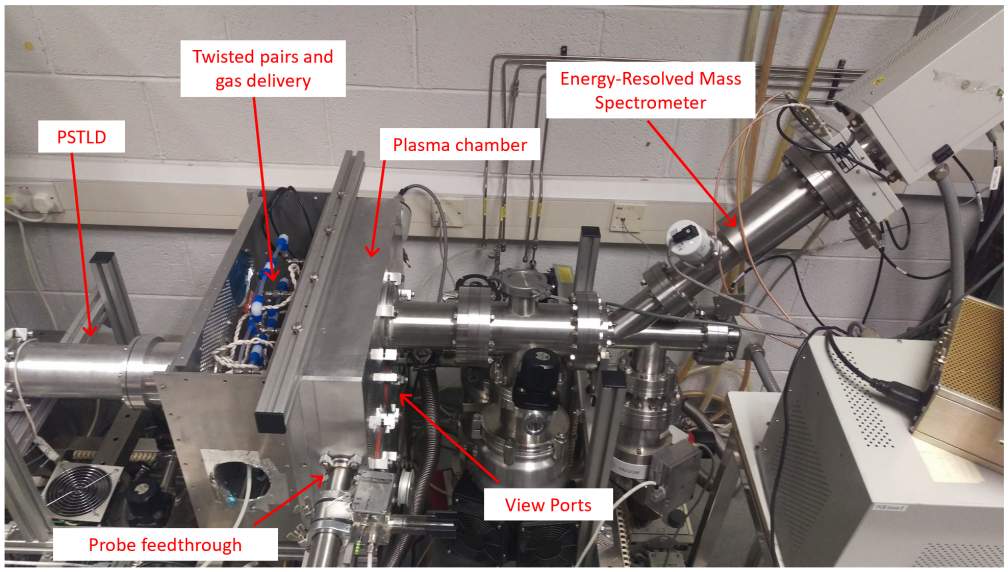

Figure 2.2: Photograph of the PASTIS experimental system

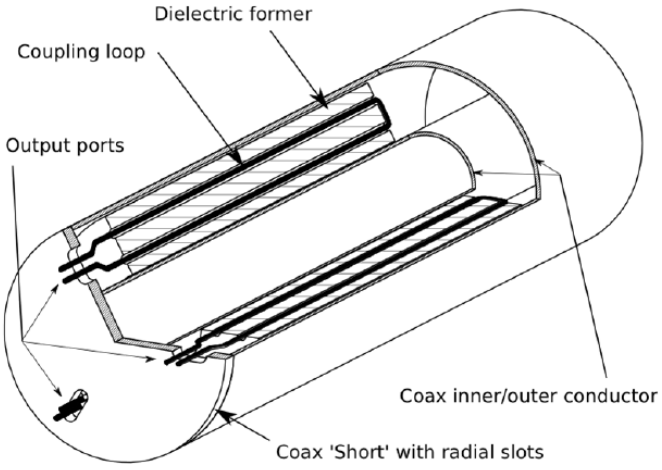

Figure 2.3: Internal structure of the PSTLD.

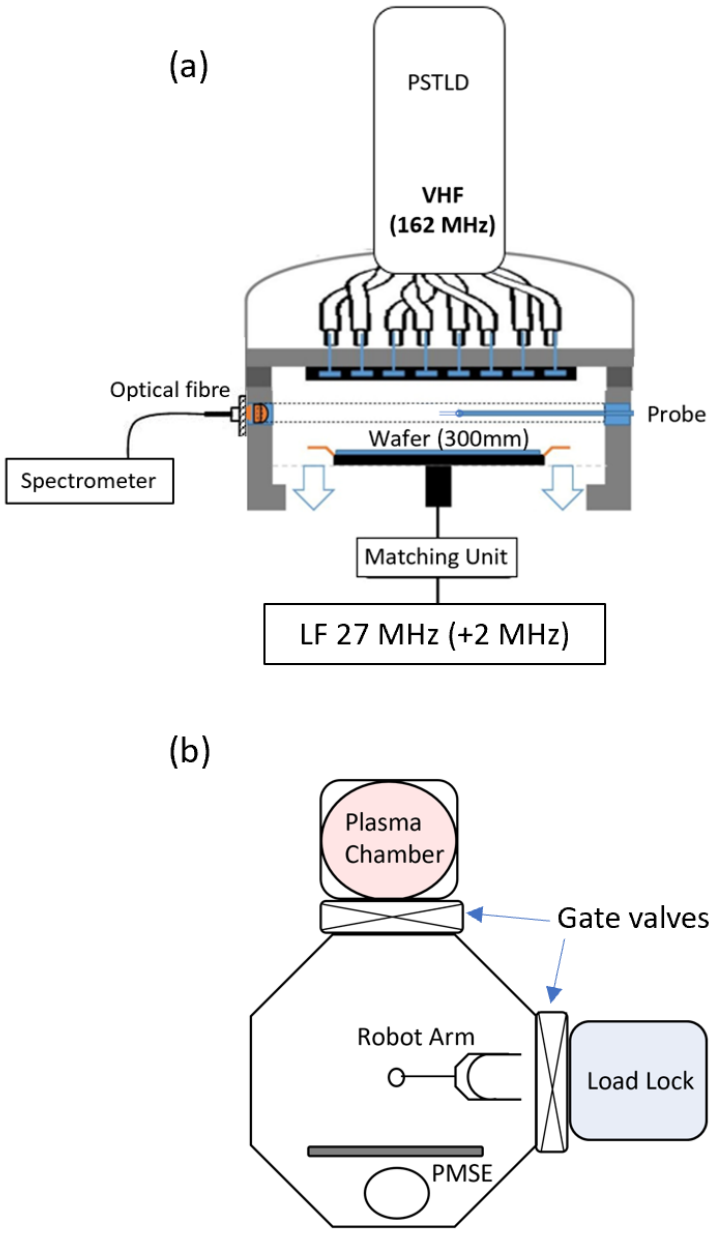

Figure 2.4: (a) Side view of the *Starchief* experimental set-up along with diagnostic probes and detection systems, not to scale, and (b) Top-down view of the transport module connected to the processing chamber and load-lock via gate via valves. Robot arm transfers wafer between load-lock, processing chamber and in-vacuo Phase-Modulated-Spectroscopic Ellipsometer (PMSE) (See Section 2.8.

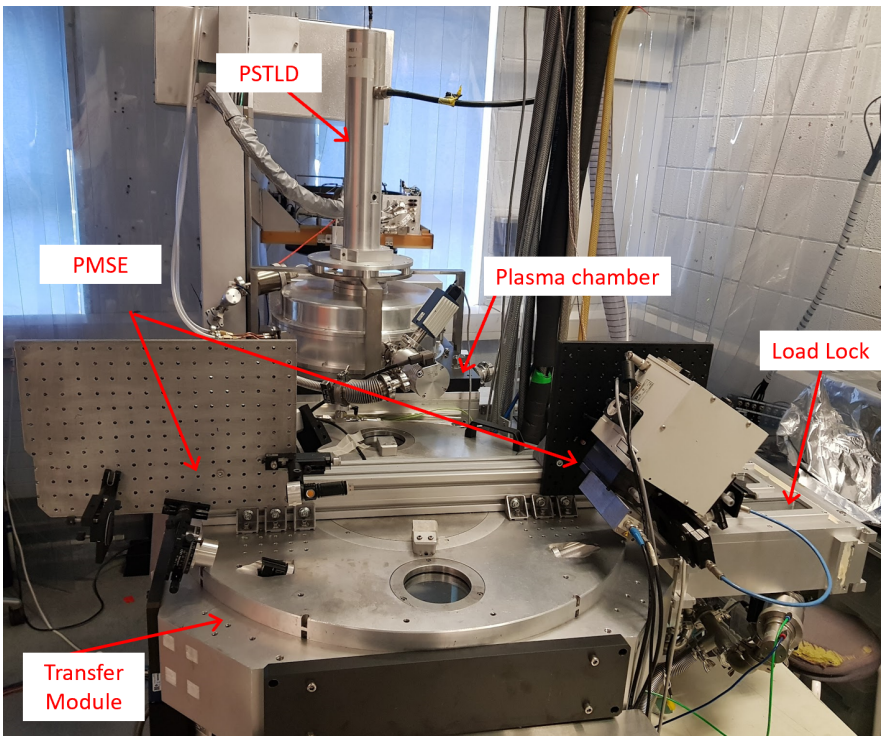

Figure 2.5: Photograph of the Starchief experimental system with transfer module, load-lock and PMSE

2.2 Description of *Starchief*: 2-frequency CCP (162 MHz VHF plasma source + 27 MHz bias at wafer)

The *Starchief* plasma reactor, shown in Figure 2.4(a), ** and the photo Figure 2.5 is a modification of an industrial low-volume CCP tool for 300 mm wafer processing, donated to the Plasma Research Laboratory by Lam Research Corporation. The tool originally had a capacitively coupled 27 MHz (+2 MHz) powered lower (substrate) electrode and grounded upper electrode. The upper electrode is now replaced with a VHF (162 MHz) multi-tile electrode and PSTLD. The multi-tile electrode is a 2-dimensional tile array for 300 mm substrate processing. There is an alumina insulation layer between the tiles and the plasma, similar to the Hawaii plasma source reported previously in [75, 76, 77]. The chamber diameter is 52 cm, and the discharge gap is 4 cm.

Similar to PASTIS, radio-frequency powered is supplied by a 162MHz Advanced Energy Ovation generator and coupled to the PSTLD which provides fully differential RF power to 15-pair outputs, resulting in a 30-tile powered electrode. The PSTLD has a single vacuum seal and power coupling loops are inside the high-vacuum. As in PASTIS, each tile is powered 180° out of phase from its neighbouring tile. The resulting modified reactor is a 2-frequency CCP; VHF (162 MHz) as upper source power and LF (27 MHz) as lower substrate-bias power. The reactor is in an unconfined configuration; outer chamber walls are exposed to the plasma and are grounded. An electrostatic chuck (ESC) is used to clamp the wafer onto the bottom electrode. Gas flow is controlled by mass-flow-controllers (MFCs) located in a (separate) gas-box. For ALE cycling, the gating (opening and closing) of pnematic valves positioned after MFCs were automated in a timing sequence (described in Chapter 4).

As shown in Figure 2.4(b), the plasma processing chamber is connected to a high-vacuum transfer-module, equipped with a robot arm to transfer wafers between the load-lock, processing chamber and in-vacuo Phase-Modulated-Spectroscopic-Ellipsometer (PMSE). Operation of gate-valves between chamber and load-lock,

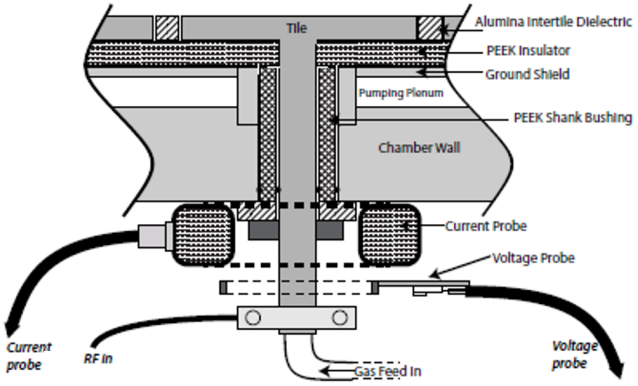

Figure 2.6: Mounting of current and voltage probes on the electrode shank on the backside of PASTIS.

valves to turbomolecular pumps, and robot arm is controlled via LabVIEW.

2.3 Electrode Current and Voltage probes

A set of current transformers and voltage probes were developed and used to the measure the current and voltage in the PASTIS reactor. The probes are placed on/around the electrode shanks of the middle row electrodes, between the backside of the chamber and the twisted pair connections, see Figure 2.6. A non-integrating Rogowski coil (Bergoz current transformer) and an in-house designed and built capacitive-resistive divider are used for current and voltage probes respectively. Most commercial voltage probes do not operate above 100 MHz or to high voltage levels. The developed probe's LCR circuit resonance is purposely chosen to be at least an order of magnitude less than the RF driving frequency (162 MHz $= 1 \times 10^9$ rad/s). Calibration for impedance and frequency sweep responses are verified using a Vector-Network-Analyser to validate sufficient separation from internal resonances. Phase calibration of probes with known resistive/capacitive loads are also accounted for.

Our recent article [78] detailed an atmospheric-pressure discharge driven by the same PSTLD at 162 MHz, configured with the above mentioned current and voltage probes. Therein, the apparent/circulating power per electrode tile was

investigated as a function of total set power. Apparent power consists of both reactive("wattless") and resistive(real) power components. With no plasma, the load is almost purely capacitive, and the apparent power value is due to a large reactive power component. Capacitive loads produce reactive power and store energy in the electric field, such that the apparent(capacitive reactive) power increases linearly until power strikes. The addition of a plasma resistive element in series counteracts the reactive power and causes corresponding increase in real delivered power. The measured Q (circulating power/dissipated power) achieved by the PSTLD in the non-plasma case was 25, dropping to ∼4 with plasma, varying the plasma condition. The ratio between the real delivered power and apparent power is related by the power factor = $cosine(\phi)$, the phase between the current and voltage. The plasma resistive element adds a real delivered power component which is evident from a current voltage phase change upon plasma strike. This experiment in the 162 MHz atmospheric-discharge confirmed a drop in voltage and increase in current upon plasma striking, which is expected for CCP-type operation.

2.4 Resonance Hairpin Probe

A floating resonance Hairpin probe is used to measure the plasma density. The working principle of the hairpin is well described and understood in the literature and is based on the combined features of Piejak's reflection mode hairpin [79] and Stenzel's floating microwave resonance probe [80]. Physically, the hairpin probe is a U-shaped metal wire. Electrically, it is an open-ended $\lambda/4$ transmission line. When a microwave is coupled to the structure, the waveform gets reflected from the open end. Incident and reflected waves constructively interfere along the hairpin structure. At resonance, the hairpin supports a standing wave and the resonance frequency is given as:

$$f_r = \frac{c}{4L\sqrt{\epsilon}} \tag{2.2}$$

where ϵ is the permittivity of the surrounding medium. If the prove is in vacuum, where $\epsilon = 1$, then the resonant vacuum frequency is:

$$f_0 = \frac{c}{4L} \tag{2.3}$$

with a sharp resonance (Q in the low hundreds). The permittivity of a medium defines the phase velocity of electromagnetic waves propagating through it. The plasma permittivity ϵ can be defined as a function of ω, which is the angular frequency of the high frequency electromagnetic field, and the plasma frequency ω_{pe}:

$$\epsilon = 1 - \frac{\omega_{pe}^2}{\omega^2} \tag{2.4}$$

The plasma frequency, as given in Eqn 1.4, is a function of the electron density, thus from monitoring the shift in resonance frequency of the hairpin from vacuum to plasma, the electron density can be determined. Specifically, from Eqns 2.2, 2.3, and 2.4, we can derive the relation for the shifted resonance frequency in the plasma:

$$f_r^2 = f_0^2 + f_p^2 \tag{2.5}$$

Again, using f_p based on the plasma frequency in Eqn 1.4, an expression for the electron density as a function of the resonance frequency in the plasma is found as:

$$n_e = \frac{f_r^2 - f_0^2}{0.81} \tag{2.6}$$

where the frequencies are in GHz and the electron density is in units of $\text{x}10^{10}\text{cm}^{-3}$.

The constructed probe for experiments was a 0.25 mm diameter molybdenum wire with a length and width of 3 cm and 5 mm respectively. The measured vacuum resonance frequency is $\sim$2.6 GHz in this case. For measurements in PASTIS,

the probe was installed from the side port, Figure 2.1, such that the probe position is ∼3 cm from the multi-tile electrode. The probe is scanned radially across the multi-tile electrode to provide a spatially resolved electron density profile. The plane of the hairpin is held perpendicular to both the axis of the probe and the plane of the multi-tiles, in order to give the best resolution of density differences between the tile edge and tile centre. For measurements in *Starchief*, again the probe was installed from the side port, Figure 2.4, such that probe position is ∼ 1 cm above the wafer. Here, the length of the hairpin is held parallel to the axis of the probe and the plane of the hairpin is parallel to the substrate (and plasma boundary). The hairpin probe is driven by a Hewlett Packard HP8350 microwave sweep generator in the frequency range of 2-4 GHz with a step size of 2 MHz. The reflected signal from the non 50 Ohm termination (coupling loop) is captured on an oscilloscope using a directional coupler and a Schottky diode. A sharp drop in the reflected signal is observed when the scanning frequency is at the resonance frequency of the probe tip. To improve signal-to-noise ratio the DC level at each frequency without plasma is subtracted from the signal with plasma. Furthermore, this subtraction is done for each position of the probe in the reactor. This mitigates any perturbation introduced by the stray capacitance variation of the vacuum feedthrough. An automated peak detection technique (developed in LabVIEW) is used for electron density measurements which give a data bandwidth of nearly 100 Hz.

2.5 Planar Flux Probe

The planar flux probe is a deposition tolerant device allowing direct measurement of ion current in the plasma. As a form of the Langmuir probe [81], the planar flux probe is simply a flat metallic disc, such that when it is placed in a plasma, and sufficiently biased negatively, all electrons will be repelled and only positively charged ions are incident on the probe tip. Figure 2.7 The electron current

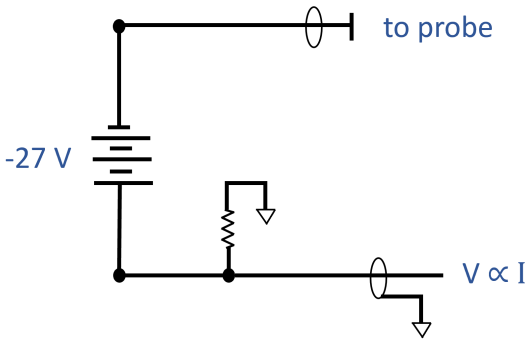

Figure 2.7: Schematic of planar flux probe.

collected by a biased probe is given by:

$$I_e = \frac{1}{4} e n_e \nu_{e,th} A \exp\left[\frac{V_B - V_P}{T_e}\right] \tag{2.7}$$

where the factor $\frac{1}{4} e n_e \nu_{e,th} A = I_{e,sat}$ is the electron saturation current, V_B is the probe bias, V_P is the plasma potential and T_e is the electron temperature, estimated to be $\sim$2 eV. For a plasma potential expected in the range of +15 to +25 V, and probe biased to -27 V, the collected electron current is sufficiently suppressed, to be considered negligible.

The magnitude of the current from the flow of positively charged ions is determined by measuring the voltage across a sense resistor (10 kΩ), that is placed in series with the negative DC supply. The probe tip used in experiments was a flat circular tungsten disc, diameter 4 mm, one side covered in ceramic, resulting in a charged collection area A is 1.25×10^{-5} m^2. The single-sided collection surface is orientated with the probe facing towards the electrode tiles.

For measurements in PASTIS, the planar probe (similar to the hairpin probe) is installed from the side port, Figure 2.1, such that the probe position is $\sim$3 cm from the multi-tile electrode. A DC-pass filter is connected in series with the circuit to ensure no RF noise is collected and that only ion currents are measured. The collected positive ion current I^+ is:

$$I^+ = 0.6 e A n_e u_B \tag{2.8}$$

where u_B is the Bohm speed given by Eqn 1.11.

2.6 Energy Resolved Mass Spectroscopy

To determine the ion energies ($(V_{DC} + \mathcal{F}(V_{RF})$, Section 1.2.5), we mount a Hiden electrostatic quadrupole plasma (EQP) system onto the grounded side of the PASTIS chamber.

The Hiden EQP operates as a mass spectrometer; samples plasma ions, or ionised neutrals, and uses the difference between the mass-to-charge ratio to separate them. The ions of each mass-to-charge ratio are then detected and displayed as a mass spectrum. The Hiden EQP system uses electron impact as source of ionisation for measuring neutrals, a quadrupole mass filter for ion sorting, and both a faraday cup and SEM (secondary electron multiplier) for detection. Furthermore, the EQP system combines a quadrupole mass spectrometer with an electrostatic 45° electrostatic sector energy analyser and therefore allows for the acquisition of mass and energy spectra of positive and negative ions, neutrals and radicals.

The EQP system can operate in two modes; plasma ion (PI) mode, or electron impact (EI) mode. In the PI mode, either positive or negative ions are sampled directly from the plasma and are focused onto the energy filter. The ionisation filters, are turned off in this operation. EI mode can also be referred to as residual gas analysis (RGA). The neutral species, which are key components playing a role in the reaction kinetics of a plasma process, are sampled and subsequently ionised by electron impact. Figure 2.8 provides an internal view of a full EQP system.

Behind the sampling orifice is the EI ion source. The purpose of this feature is to analyse the neutral species in the plasma, and in doing so, the plasma ions are rejected from entering the sampling region by applying a suitable potential to the extractor electrodes. In this ionisation method, a beam of electrons pass through a gas-phase sample, collide with neutral species, and transfer sufficient energy to the valence electron for its ionisation. The EI ionisation collision can

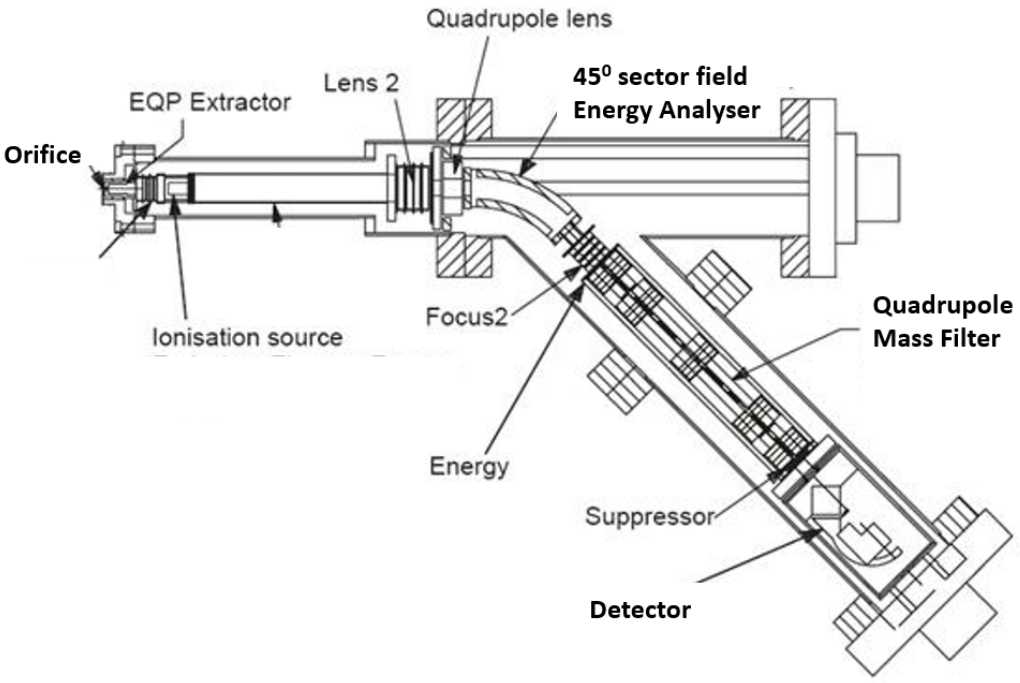

Figure 2.8: Hiden EQP mass and energy analyser.

be expressed as:

$$M + e \rightarrow M^{+} + 2e^{-} \tag{2.9}$$

The EI ionisation cross section is dependent on the energy of the incoming electron and is zero below a certain threshold energy, the ionisation energy. The cross sections typically reach a maximum between 50-100 eV, and for the vast majority of atomic and molecular gases, an electron energy of 70 eV is set as optimum value.

The EQP system uses thermionic emission from two current heated filaments to provide the beam of electrons for ionisation and the energy of these electrons can be varied. An ion source cage collects the electron emission current, typically on the order of 10^{-4} A, and thus the filament current can be monitored. This electron emission current also allows for the determination of the ionisation potential of neutrals and radicals. The EQP series is equipped with oxide coated iridium filaments, with an operating temperature of 1900 K, which is suitable for

gas mixtures with oxygen.

If the EQP system is operating in PI mode, the ionisation filaments are turned off, and the sampled plasma ions are passed through the transfer ion optics. In this transfer space, ions are accelerated to higher kinetic energies. Electrostatic lenses are then used to focus the ions into the energy filter. The electrostatic lenses are subject to the same chromatic aberrations as optical lenses. Chromatic aberrations (focal length is dependent on ion energy) mean that ions of different energies are deflected and focused to different locations. O'Connell et al [82] investigated the acceptance angle of the EQP system as a function of the ion energy for typical lens settings using SIMION, a computer simulation package. The acceptance angle depends on the electric field just inside of the orifice, and hence on the settings of the first electrostatic lenses. Their results provided optimum voltage settings to be used for a smooth function, with no increased acceptance angles for higher energy ions. They compared their simulation results to the extensive study by Hamers [83] which detailed ion transmission functions in a slightly different EQP system. The EQP from [82] uniquely has an extra-long drift tube (from 240-750 mm) and an additional fight-focus electrode.

A 45° electrostatic sector energy analyser analyser is used in the EQP system to provide minimum loss to the ion transfer path within the analyser for optimum energy resolution. It is formed by five electrodes which set the energy of the ions that can pass through the energy filter, as well of focusing and aligning the ion beam. The energy range is 100 eV, energy resolution (FWHM) is better than 0.25 eV [1], and the energy transmission for a sector field analyser is 100% [2].

After the kinetic energy of the ion beam is reduced from a decelerating lens, the ions are injected into the quadrupole mass filter. This comprises of three subdivisions; pre-filter (RF), main filter (RF and DC) and post filter (RF). In the main filter, there are four rods, arranged in the form of a square, as shown in Figure 2.9, which are electrically biased with both RF and DC to produce fields that confine small ranges of mass-charge ratios. Any ions entering the quadrupole field experience potential differences deflecting them from the original trajectory. The

[1] In comparison to other energy analysers such as the Bessel Box Energy Analyser(BBEA) which has 0.5 eV resolution [84], and 1 eV for the Retarding Field Energy Analyser(Impedans).

[2] Significantly better than the BBEA, which has transmission efficiency of 10%

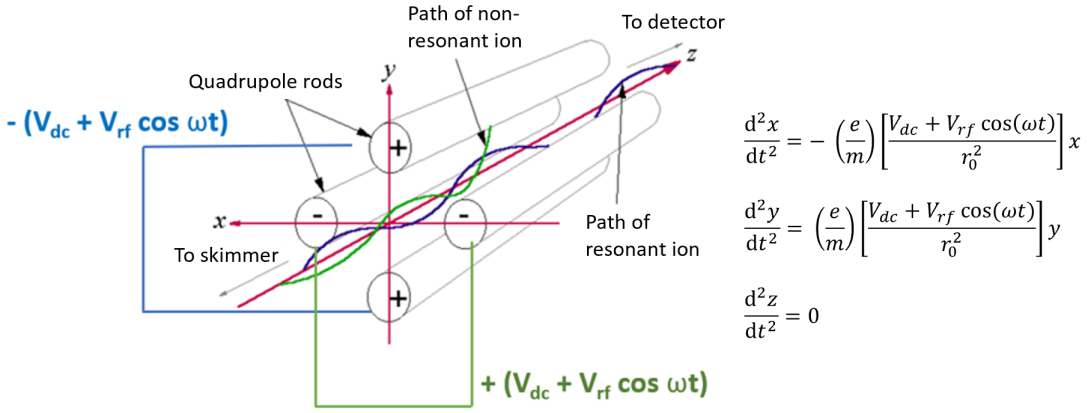

Figure 2.9: Quadrupole mass filter with corresponding RF voltages on alternating rods, as described by the Mathieu's equations (right).

extent of this deflection correlates to their mass-charge ratio. At each interval of the RF scan, only one mass-charge ratio, pre-set by the user, resonates with the specified field, and these ions are permitted to pass along the z-axis of the rods, i.e. towards the detector, Figure 2.9. All other unwanted mass-charge ratios are accelerated towards the rods, neutralised and undetected. The resulting applied quadrupole field within the rods deflects ions in the x and y directions. The trajectory oscillation amplitude must be smaller than the field radius for ions to reach the detector. The motion of the ions is described by Mathieus equations [85], which also depicts the four rods in the main filter with the corresponding RF voltages described in the Mathieu's equations, shown in Figure 2.9, where V_{dc} and V_{rf} is the amplitude of the DC and RF voltages respectively, ω is the RF frequency, r_o^2 is the closest distance between the four electrode poles, e is electron charge and m is ion mass.

The filtered ions leaving the quadruple mass filter are focused onto an ion counting detector, and an ion current is measured by a sensitive amplifier. There are two detection devices available in the EQP: an SEM (secondary electron multiplier) or a Faraday cup. The SEM is designed to produce secondary electrons. Ions hitting the SEM surface emit two or three electrons, each of which undergo further collisions, generating more electrons. The EQP uses a continuous dynode which provides the applied voltage for this cascading effect. The Faraday cup is simply an earthed passive conducting surface in the shape of a cup. Ions strike

the cup, and cause a cascade of secondary electrons. The Faraday cup option extends the detection range up to $5\,\text{x}10^{11}$ counts for high density plasma applications. For all results in Chapter 3 the Faraday cup is used.

The EQP system is mounted flush to the grounded electrode of the PASTIS reactor. A rotatable off-centre flange was designed and added to the end of the EQP system so that the orifice sampling position could be rotated from tile centre to tile edge.

2.7 Optical Emission Spectroscopy

Optical Emission Spectroscopy (OES) is used to provide "free", non-invasive information on the internal condition of the plasma. There can be challenges to using OES, such as optical transparency, overlapping emission lines, and multiple excitation pathways. In this work, we select techniques that permit the extraction of internal state information, specifically: vibrational temperature (T_{vib}), rotational temperature (T_{rot}), and actinometry, which will be discussed in the following sections. First, the optical access and light collection from PASTIS and *Starchief* will be described.

2.7.1 Optical Access

In the PASTIS system, light that is emitted from the plasma is collected by a lens mounted on the grounded side of the chamber, oriented such that it collects light from the columnar region above the lens. The lens sits in a rotatable flange, mounted on the grounded side of the chamber, allows for collection from either the region at tile-tile boundary, or from a tile face (Figure 2.1). The collimated light from the lens is focused onto an optical fibre. The optical fibre is 600 μm in diameter with high efficiency in the UV-Vis range. A Horiba Jobin Yvon spectrometer is used with optical resolution of 0.3 nm.

In the *Starchief* system, optical emission is collected from a side viewport, as

shown in Figure 2.4(a). The lens and fibre collects the integrated emission from a cylindrical column across the diameter of the discharge. Here, the optical fibre is coupled to an Ocean Optics HR2000+ spectrometer.

The Horiba Jobin Yvon and Ocean Optics HR2000+ spectrometers are calibrated to a known-light standard, and analysed spectra are corrected for variations in system efficiency versus wavelength.

2.7.2 Vibrational and Rotational Temperatures

In PASTIS, the optical emission spectra of N_2 is obtained in the wavelength range of 250-900 nm. A typical optical emission spectrum of N_2 and the corresponding energy level diagram for the lowest electronic states is shown in Figure 2.10. From the N_2 emission spectra, vibrational and rotational temperatures are determined. Rotational temperature is determined by comparing the shape of the measured and simulated spectra, whereas, vibrational temperature is determined by the slope of a Boltzmann fit on the peaks with the vibrational quantum number difference $\Delta\upsilon = -2$. The detailed descriptions of the rotational and vibrational temperature measurements are as follows.

Vibrational temperature(T_{vib}) is determined from the N_2 second positive system (SPS) $\Delta\upsilon = -2$ transitions from the excited level $C^3\Pi_u$. Initially the N_2 gas starts in the molecular ground state $X^1\Sigma_g(\upsilon{=}0)$ and, through energy exchange collisions with electrons, gets excited into one of the vibrational levels ν' of excited electronic state $C^3\Pi_u$. From here, it decays to a lower level $B^3\Pi_g$ by spontaneous emission, resulting in a line emission intensity $I_{\upsilon'-\upsilon''}$:

$$I_{\upsilon'-\upsilon''} = \frac{c(\lambda)A_{\upsilon'-\upsilon''}N_{\upsilon'}}{\lambda} \tag{2.10}$$

where $c(\lambda)$ is the spectrometer response factor at wavelength λ, $A_{\upsilon'-\upsilon''}$ is the Einstein coefficient for the probability of spontaneous transition, λ is the wavelength of the transition, and $N_{\upsilon'}$ is the population density of the excited state. For a

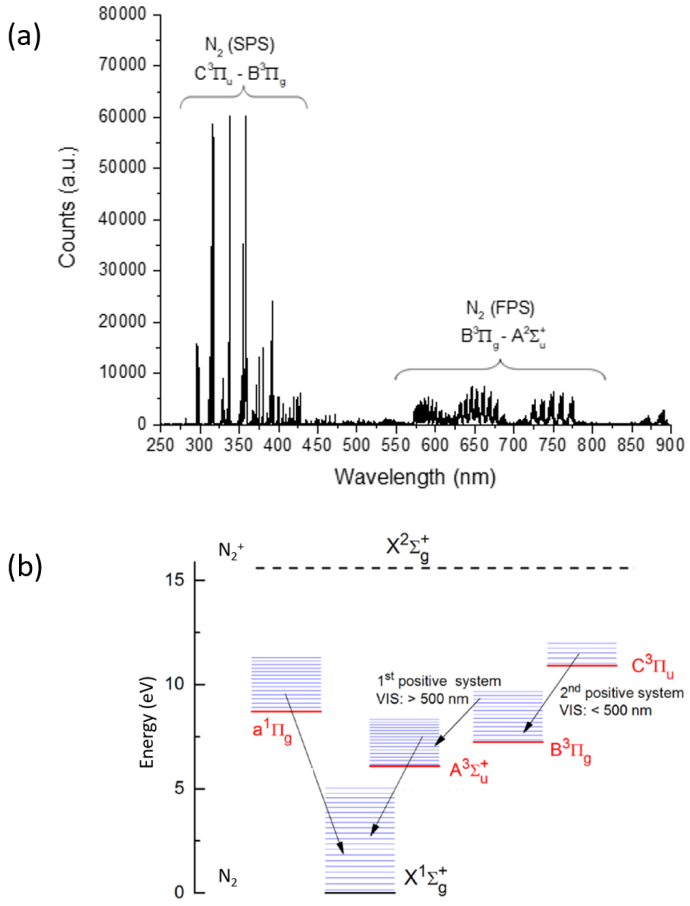

Figure 2.10: (a) Typical spectrum of the N_2 plasma from PASTIS, showing radiative transitions from second positive system (SPS) and the first positive system (FPS) of molecular nitrogen. The SPS, intense in the UV range can be overlapped by radiation of the first negative system (FNS) of the molecular nitrogen ion (N_2^+). (b) Energy level diagram for the lowest electronic states with vibrational levels of N_2.

Boltzmann distribution for the population density of the vibrationally excited state:

$$\frac{N_{\upsilon'}}{N_{\upsilon=0'}} = exp\left(\frac{-E_{\upsilon'}}{kT_{vib}}\right) \tag{2.11}$$

where $-E_{\upsilon'} = (\nu + \frac{1}{2})\omega_e$ is the vibrational energy of the excited molecules in the quantum harmonic oscillator approximation disregarding the anharmonicity constant [1]. A sequence of four peaks are used, with a vibrational transition sequence $\Delta\upsilon = -2$; 0-2 at 380.4 nm, 1-3 at 375.4 nm, 2-4 at 370.9 nm, 3-5 at 367.0 nm[2]. Using Eqn 2.10 and this series of emission peaks, T_{vib} can be obtained from [87]:

$$ln\left[\frac{I_{\upsilon'-\upsilon''}}{A_{\upsilon'-\upsilon''}}.\lambda\right] = \frac{E_{\upsilon}^{'}}{kT_{vib}} + constant \tag{2.12}$$

The vibrational temperature is represented by the inverse slope of a linear fit of $ln\left[\frac{I_{\upsilon'-\upsilon''}}{A_{\upsilon'-\upsilon''}}.\lambda\right]$ as a function of the vibrational energy of the excited molecule. Within the SPS, the chosen vibrational transition sequence $\Delta\upsilon = -2$ is suitable because it has a longer radiative lifetime of 36 ns, and contains the most intense lines in the SPS. Figure 2.11 depicts the allowed transitions within the SPS, and inset shows the selected sequence of peaks. The spectroscopic parameters for these selected peaks, to use in Eqn 2.12 are presented in Table 2.1. Einstein coefficients are taken from [88](page 1062).

[1] ω_e, vibrational wavenumber on level $C^3\Pi_u$ is provided by [86] page 194

[2] For the four transistions used to determine T_{vib}, the spectral response of the spectrometer is equivalent, and also the transmission spectrum of the glass view-port is accounted for.

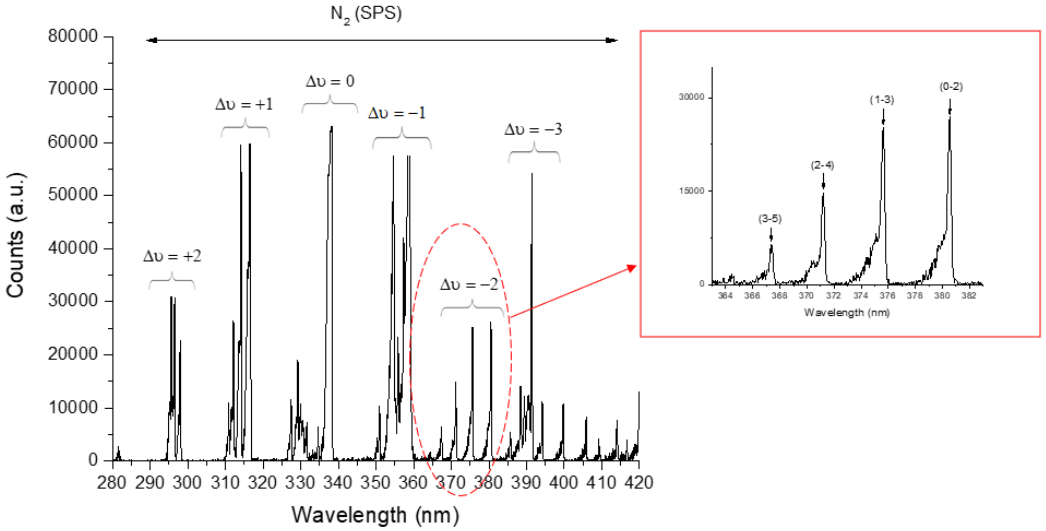

Figure 2.11: (Main view) Typical spectrum of the N_2 emission peaks from the SPS. (Inset) Sequence of peaks with $\Delta\upsilon$=-2 for the vibrational temperature determination.

λ(nm)	$A_{\upsilon'-\upsilon''}$(x10^6 s^{-1})	$E_{\upsilon'}$(cm^{-1})
367.0	2.35	6913.62
370.9	4.04	4981.00
375.4	4.93	3014.22
380.4	3.56	1013.28

Table 2.1: Spectroscopic parameters used for determination of vibrational temperature

Rotational temperature(T_{rot}) can be determined using rovibrational spectroscopy band fitting; by iteratively comparing experimental spectra of an unresolved vibrational band envelope with simulated spectra of a known T_{rot}, until the smallest fitting error is reached. For nitrogen discharges, any emission bands within the second positive system (SPS) or first positive system (FPS) can, in principle, be used [89]. Background gas temperature is often inferred from this determined T_{rot} provided that the time needed for thermal relaxation to occur between the rotational and translational states (τ_{RT}) is shorter than the radiative lifetime of the excited state (τ_{RAD}). This is not the case in our experimental

conditions ($\tau_{RT} \approx 10^{-5} - 10^{-6}$s, which is longer than the τ_{RAD} of the SPS and FPS). However, if electron impact is the dominant excitation process (i.e. SPS), T_{rot} can still mirror the background gas temperature. Due to the mass difference between the electron and molecule, the molecular rotational moment is conserved in a collision, such that the ground state maps into the excited state distribution. For this reason, the SPS, and specifically the transition $C^3\Pi_u(\upsilon{=}0)$ to $B^3\Pi_g(\upsilon{=}2)$ at 380.4 nm, is the most commonly used emission band to determine T_{rot}(gas temperature) in low pressure nitrogen discharges [90, 91, 92]. The procedure for obtaining simulated spectra is well described in the literature [93]. First, the wavelength of each **J'→J"** transition (where **J** is rotational quantum number) in a rotational band is calculated. Based on the selection rule $\Delta\mathbf{J}{=}0, \pm1$ the P, Q and R branches are calculated. Next, the theoretical intensities should be related to the rotational temperature and then the discrete lines are convolved with a suitable function (Gaussian or Voigt) to correct for instrument broadening. Finally, after adding up all the branches the unresolved rotational band is compared with the measured spectra, in MATLAB, for different values of rotational temperature to obtain the best fit between measured and simulated spectra using a least-squares fitting analysis [94]. The parameters used to obtain simulated spectra are taken from the literature [93].

2.7.3 Actinometry

In Starchief, actinometry is used to measure changes in atomic fluorine density in fluorocarbon discharge excited by VHF or LF. The actinometric technique, introduced by Coburn and Chen [95], is based on the comparative measurement of the line emission of a species of interest with unknown density, to the line emission of an actinometer species of known density. In this work, argon is employed as the actinometer and optical emission at 750.4 nm and 703.7 nm is used for argon and fluorine respectively. Valid actinometry requires that actinometer and species of interest undergo the same excitation path. The excited states of Ar (750.4 nm) and F (703.7 nm) are assumed to be populated solely by electron impact from the ground state: all upward transitions to excited states are by electron impact and

all downward transitions are by radiative decay with a constant branching ratio. The intensity of the optical emission from the excited state is:

$$I_X = k_e^X \; r_X \; n_e \; [X] \tag{2.13}$$

where r_X is the branching ratio for emission relative to all other de-excitation paths, n_e is the electron density, $[X]$ is the concentration of species, and k_e^X is the excitation efficiency:

$$k_e = \int f(\epsilon)\sigma_e(\epsilon)\upsilon(\epsilon) \; d\epsilon \tag{2.14}$$

where $\upsilon(\epsilon)$ is the electron velocity, $f(\epsilon)$ is the electron energy distribution and $\sigma_e(\epsilon)$ is the collision cross section for species excitation. By scaling the emission intensity of species X with emission intensity of the actinometer A, the actinometric ratio no longer depends on n_e and the branching ratios are assumed constant under conditions when collisional de-excitation is not important:

$$\frac{I_X}{I_A} = \frac{k_e^X \; [X]}{k_e^A \; [A]} \tag{2.15}$$

The threshold excitation energy of F line at 703.7 nm (14.8 eV) is similar to threshold excitation energy of Ar emission line at 750.4 nm (13.5eV), and their excitation cross sections have similar functionalities. Therefore the ratio of excitation efficiencies k_e^X/k_e^A can be considered constant, and the monitoring of relative atomic F densities with Ar by the actinometric method is valid.

2.8 Ellipsometry

Elllipsometry is an optical technique which derives film thickness and optical properties from measuring the change in light polarisation upon reflection from a surface. When light strikes a surface at oblique incidence it splits the beam; a

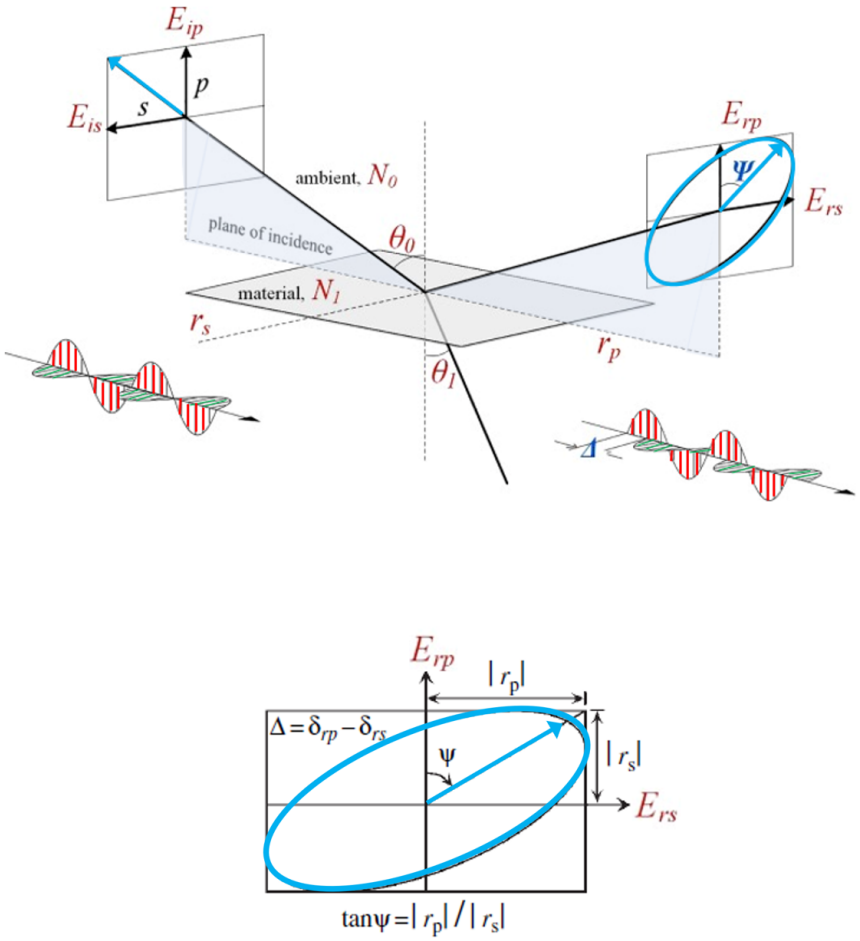

Figure 2.12: Changes in the polarisation of light by reflection from a surface.

portion is deflected into the material, a portion is reflected and a portion may be absorbed. If two parallel surfaces are close enough to each other in comparison to the wavelength of light (i.e. in the case of a thin film on a substrate), the reflected beams from each surface will form an interference effect. Information about the surface and material is contained in the polarisation state of this resulting beam.

Polarisation states are usually defined in terms of the electric-field vector of the electromagnetic (light) wave. We can define the oscillation directions of the electric field relative to the plane of incidence, such that p- and s- polarisations have electric field oscillating parallel and perpendicular to the plane of incidence respectively, as shown in Figure 2.12. Upon reflection, these p- and s- polarisa-

tion states experience different attenuation and phase shift [96]. This effect is described by the well-known Fresnel amplitude reflection coefficients r_p and r_s for p- and s-polarisation respectively:

$$r_p = \frac{E_{p,r}}{E_{p,i}} = |r_p|\exp(i\delta_{rp}) \qquad r_s = \frac{E_{s,r}}{E_{s,i}} = |r_s|\exp(i\delta_{rs}) \tag{2.16}$$

where the subscripts i and r are incident and reflected components. The phase δ indicates the delay introduced by the reflection and the absolute value $|r|$ represents the change of the amplitude. Ellipsometry measures the ratio of the reflection coefficients, and is generally written in terms of the so-called ellipsometric parameters Δ and Ψ:

$$\frac{r_p}{r_s} = \tan\Psi\exp(i\Delta) \tag{2.17}$$

where $\Delta = \delta_p - \delta_s$ is the relative phase difference between both components and $\tan\Psi = {}^{|r_p|}/_{|r_s|}$. Measurements are usually performed at an angle of incidence where the difference between r_p and r_s is maximized, i.e. at the Brewster angle. Ellipsometry is an indirect measurement, therefore a model-based analysis is required to fit experimental data to optical models and extract desired information such as film thickness and refractive index from a best-fit.

All ellipsometers contain the same basic components; light source, polarisation generator, polarisation analyser, and detector. To measure the difference in amplitude between the p- and s-polarised components of the reflected light, it is necessary to separate the polarisations prior to the light entering the analyser. This process involves rotating or modulating one of the optical elements, then deducing the polarisation state by examining the time-dependence of the intensity reaching the detector. In this way, ellipsometry systems are generally classified into two categories; systems that use rotating optical elements [97, 98, 99] and those that use photoelastic modulators [100, 101, 102]. For rotating element configurations, the component is driven by a mechanical motor with typical frequencies $\sim$100 Hz. In phase-modulated-spectroscopic-ellipsometer (PMSE), instead of

a rotating polariser/analyser/compensator, a birefringement modulator is used to introduce a periodic sinusoidal phase difference between the polarised waves. Under the principle of the photoelastic effect, the photoelastic modulator (PEM) is composed of a material that exhibits birefringence proportional to the mechanical stress induced on it. The modulation is imposed by applying an AC voltage to a piezoelectric transducer which is coupled to the PEM crystal, typically at a frequency of 50 kHz corresponding to the resonant frequency of the quartz crystal material. The PEM induces a phase difference $\delta(t)$ relative to the p- and s-components, of:

$$\delta(t) = \delta_m(\lambda, V)\sin(\omega t) \tag{2.18}$$

where $\omega = 2\pi f$ and f=50 kHz. δ_m is the retardation amplitude, proportional to V/λ, where V and λ are the voltage applied to the piezo-transducer and wavelength of light respectively. In this work, a PMSE was constructed onto the lid of the transfer-module (Figure 2.4(b)) for in-vacuo measurements, and the set-up is shown in Figure 2.13. [1] The components of the optical system are: a white LED flashlight as a broadband (400-700 nm) light source, a 200 mm focal length mirror, Glan Taylor Prism polariser and analyser, a SpectraPro-150 monochromator and ARC photomultiplier tube P2(R928) with a high-voltage power supply. Details and specifications of these listed optical components are provided in [103]. For the original RAS application, the polarising optics have a high extinction ratio ($\sim 10^{-5}$), however PMSE does not demand such a high extinction ratio and is only weakly sensitive to small deviations in the angular orientation of each component [104]. The light, after passing through the polariser is incident and reflected from the sample (in vacuum) at an angle of 70°. Light entry and exit from the vacuum transfer-module is through sapphire windows at near perpendicular to the window plane, and parallel to the c-plane of the sapphire, to reduce strain-induced birefringence. The photoelastic modulator is a PEM90 from Hinds

[1] The PMSE was constructed using components from a Reflection-Anisotropic-Spectroscopy (RAS) system donated to us from another research group in the School of Physics. RAS measures at normal incidence ($\theta_i < 5°$) where there is no distinction between r_p and r_s. In a sense, RAS is a reduced form of ellipsometry, in that it only monitors r_p from perpendicular directions in the plane of the sample, and therefore is a probe of surface anisotropy.

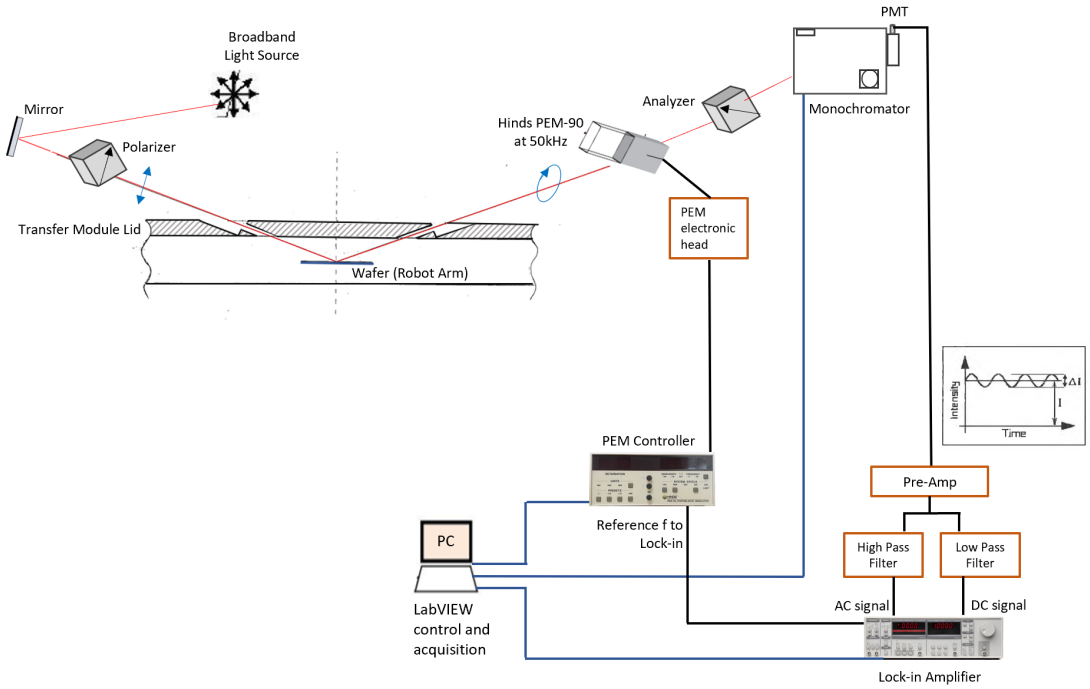

Figure 2.13: Set-up of the Phase-Modulated-Spectroscopic-Ellipsometer mounted onto the Starchief transfer-module lid.

Instruments, with a modulator frequency of 50 kHz. The conventional ellipsometry parameters Ψ and Δ are related to 3 components of the detected signal in PMSE; DC component, component at PEM frequency (ω), and component at twice the PEM frequency (2ω). The theoretical expression of the light emerging from the optical components as shown in Figure 2.13 can be analysed using Jones and Mueller matrix representation, which is detailed elsewhere [105][1]. Here, we start by setting the polariser angle to 45° and the angle between the analyser and PEM is 45°, then we can express the detected light signal as:

$$\begin{aligned} I(t) = I_{dc}[1 &+ (\sin 2\Psi \sin \Delta) \sin \delta(t) \\ &+ (\cos 2\Psi \sin 2\theta_M + \sin 2\Psi \cos \Delta \cos 2\theta_M) \cos \delta(t)] \end{aligned} \tag{2.19}$$

[1]See section 3.3, 3.4 and 4.2 in [105] for in-depth analysis and derivation with Jones and Mueller matrices

where θ_M is the angle of the PEM. In PMSE, it's more convenient to use the associated parameters given by [100]:

$$\begin{aligned} N &= \cos 2\Psi \\ S &= \sin 2\Psi \sin \Delta \\ C &= \sin 2\Psi \cos \Delta \end{aligned}$$

Equation 2.19 can therefore be rewritten as:

$$\begin{aligned} I(t) = I_{dc}[1 &+ S \sin \delta(t) \\ &+ (N \sin 2\theta_M + C \cos 2\theta_M) \cos \delta(t)] \end{aligned} \tag{2.20}$$

$\delta(t)$ is the PEM sinusoidal modulation from Equation 2.18, such that the terms $\sin \delta(t)$ and $\cos \delta(t)$ can be Fourier analysed to give:

$$\begin{aligned} \sin \delta(t) &= \sin[\delta_m \sin(\omega t)] = 2J_1(\delta_m) \sin(\omega t) \\ \cos \delta(t) &= \cos[\delta_m \sin(\omega t)] = 2J_0(\delta_m) + 2J_2(\delta_m) \cos(\omega t) \end{aligned} \tag{2.21}$$

where $J_n(\delta_m)$ is the nth Bessel function of the argument δ_m. Combining Equations 2.20 and 2.21, it's evident that the intensity possess the harmonics of the PEM frequency ω including a DC term. Variations in the source intensity and transmittance of the optical system can be rendered inconsequential by normalising the harmonic components with respect to the DC intensity [106]:

$$\frac{I(t)}{I_{dc}} = 1 + S[2J_1(\delta_m) \sin(\omega t)] + C[2J_0(\delta_m) + 2J_2(\delta_m) \cos(\omega t)] \tag{2.22}$$

where θ_M is set to 0° in Equation 2.20. The normalised intensities of the first and second harmonics are therefore:

$$\frac{I_\omega}{I_{dc}} = S[2J_1(\delta_m)] \quad and \quad \frac{I_{2\omega}}{I_{dc}} = C[2J_0(\delta_m) + 2J_2(\delta_m)] \tag{2.23}$$

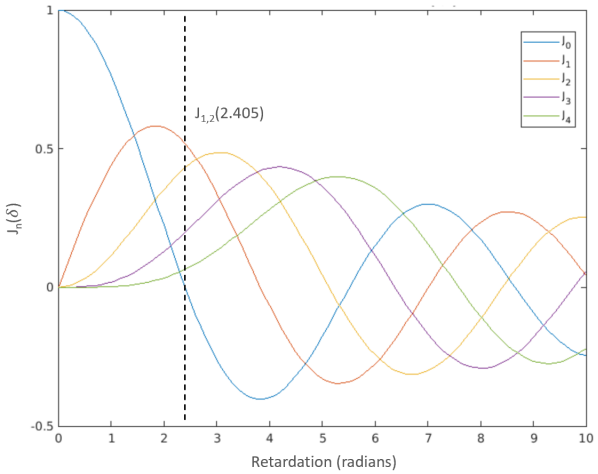

Figure 2.14: Plot of Bessel functions. Dashed line shows retardation value 2.405 radians where $J_1(\delta_m)$ and $J_1(\delta_m)$ are within 15% of their maximum values.

To maximise $^{I_{\omega,2\omega}}/_{I_{dc}}$ it is necessary to select a retardation amplitude to give the maximum value at both first and second harmonic intensities. Figure 2.14 shows the first 5 Bessel functions. With $J_0(\delta_m) = 0$, a retardation amplitude of 2.405 radians provides $J_1(\delta_m)$ and $J_2(\delta_m)$ that are within 15% of their maximum values. As shown in Equation 2.18 the retardation amplitude is a function of applied voltage and wavelength. Thus, in order to keep $\delta_m = 2.405$ radians constant for different wavelengths, the applied voltage has to be adjusted. The internal calibration (δ_m vs λ) of the Hinds PEM90 was tested and confirmed on another RAS optical set-up [107].

The output signal current from the PMT, with typical amplitude of ∼micro-amps, is composed of the AC component(at ω and 2ω as described above) superimposed on the DC offset. A pre-amplifier circuit [103] consisting of a low-pass and high-pass filter is used to separate out (and amplify) the DC and AC components respectively. The pre-amplifier also converts the photo detector current into a voltage output that is fed into the lock-in amplifier (Stanford Research SR830). The analog-to-digital converter of the lock-in amplifier is used to measure the DC component and the AC component is phase-sensitively measured using the modulation frequency of the PEM as a reference signal. The lock-in amplifier, monochromator and PEM are connected to PC and a LabVIEW program was

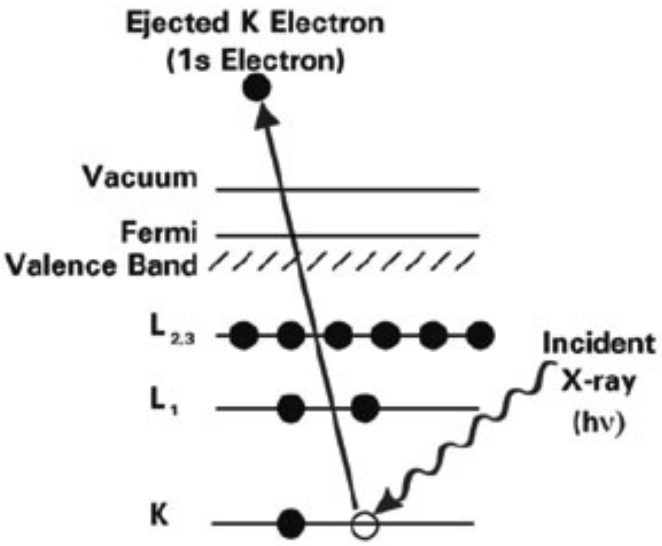

Figure 2.15: Photoemission process involved for XPS surface analysis: incident X-ray causes core electron ejection [108].

developed to control the PMSE system.

To benchmark measurements in the in-vacuo PMSE, an ex-situ commerical ellispometer (M-2000UI by J.A.Woollam Company) is used. Here, ellipsometric data is recorded at an incidence angle of 75° with a rotating-compensator configuration. Data is analysed using the EASE software, and can be displayed in terms of Ψ and Δ, or the PMSE parameters N,S and C.

2.9 X-Ray Photoelectron Spectroscopy

X-ray photoelectron spectroscopy (XPS) is a surface sensitive technique used to determine the chemical composition and chemical environment of materials. XPS spectra are obtained by irradiating a surface with a beam of x-rays, while simultaneously measuring the kinetic energy of the electrons emitted from the material (Figure 2.15). Given that every energy level of each element has a discrete binding energy, the elemental composition of a sample material can be determined by comparing the measured binding ($\propto$kinetic) energies to known spectra. In addition

to identifying elemental composition, XPS has the ability to distinguish between different chemical environments of the same element. Small shifts in the kinetic energy of the electron caused by the outer electron cloud is dependent on the relative electronegativity of bonding-partners, and this yields chemical bonding information. The binding energy of the electron is obtained from the measured kinetic energy as follows. An energetic (X-ray) photon transfers its energy ($h\upsilon$) to a core electron with a binding energy (E_B), which in turn leaves the shell with a certain kinetic energy. The kinetic energy (E_{Kin}) of that electron in vacuum is given by $h\upsilon - E_B - \Phi_S$, where Φ_S is the sample material work function. With Φ_{Spec} the spectrometer work function, according to Equation 2.24, the E_{Kin} measured by the spectrometer is given by $E_{Kin} = h\upsilon - E_B - \Phi_S - (\Phi_{Spec} - \Phi_S) = h\upsilon - E_B - \Phi_{Spec}$, such that the binding energy is [109]:

$$E_B = h\upsilon - E_{Kin} - \Phi_{Spec} \tag{2.24}$$

This equation allows the binding energy of an electron to be obtained once the X-ray photon energy and spectrometer work function are known.

In this work, XPS sample characterisation is performed ex-situ using a non-monochromated MgKα source with base pressure of 1.12x10^{-10} mbar with a VG Microtech Clam 2 Hemispherical analyser. Wide-energy-range survey and high resolution spectra are taken at normal emission from the sample surface with 0.5 and 0.1 eV step sizes respectively. Angularly-Resolved XPS is carried out an angle of 60° off-normal emission. All spectral analysis of XPS data is carried out using CasaXPS processing software. Spectra are surface charge compensated by calibrating the binding energy position of the Si2p peak at 103.5 eV [110]. Spectra are fit using a Shirley-Sherwood type background [111] and deconvoluted into chemical contributions using Voigt profiles (Gaussian-Lorentzian 70/30%), and components are fit using a least-squares fitting routine.

Chapter 3

VHF Plasma in Single-Frequency CCP: PASTIS Results

Contents

3.1 Nominal Operation of a Differentially-Fed Multi-tile Electrode

The PASTIS reactor is comprised of a multi-tile electrode driven at VHF (162 MHz). The tiles in the electrode are differentially fed such that additional current paths exist in the discharge in comparison to a conventional CCP (Section 1.4.2). This chapter presents results from the PASTIS system, and describes plasma dynamics of VHF multi-tile discharges and unique RF power coupling mechanisms associated with VHF and differential power delivery. Section 3.2 explores plasma uniformity by hairpin electron density measurements, and discharge non-equilibrium by OES analysis in Section 3.3. Section 3.4 presents measurements of RF current and voltage, electron, positive and negative ion densities, and IEDs in a low-pressure O_2 discharge. We find differences in how RF current and voltage,

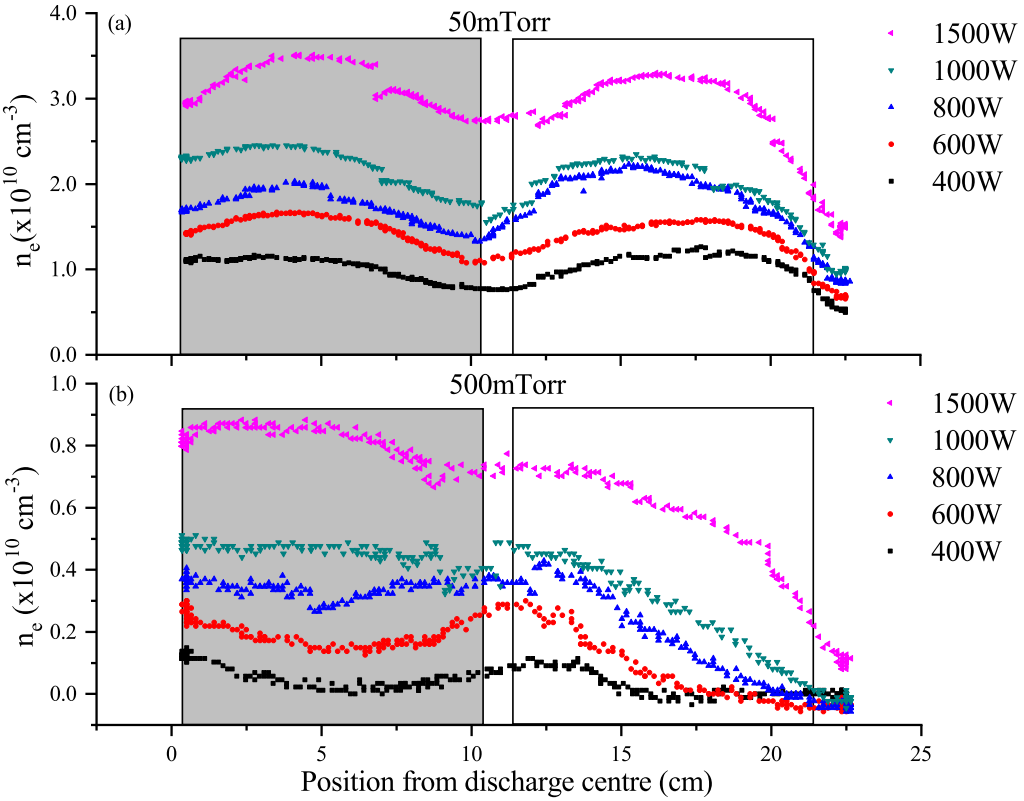

Figure 3.1: Spatial electron density profile for N_2 across radial 2 tiles as function of power at (a) 50 mTorr and (b) 500 mTorr. The shaded/blank boxes representing electrode tile (180° out of phase) boundaries.

plasma densities, and ion energy scale with power, and use this to identify changes in power coupling mechanisms, and conclude there is a smooth transition in operational mode with increasing plasma density (power). Extending beyond this low-pressure electronegative case, Section 3.5 presents results in high-pressure O_2 and electropositive Ar which are indicative of electrical asymmetry in the VHF multi-tile system.

3.2 Spatial Uniformity

To investigate the spatial density variation in PASTIS, the hairpin probe is scanned radially across the multi-tile electrode to provide spatially resolved elec-

tron density profiles. Figure 3.1 plots the measured density profile from the centre of the discharge out to the edge. This spatial profile extends across two tiles (as illustrated by the shaded/blank boxes in Figure 3.1), inter-tile gap (tile edge), and towards the chamber edge where the dielectric "skirt" is located. Note also that the tile spacing (11 cm) is twice the discharge gap (5.5 cm). The n_e profile in Figure 3.1 is measured in a N_2 discharge at gas pressures of 50 mTorr and 500 mTorr for 400-1500 W RF power. As displayed in Figure 3.1, the multi-tile solution to VHF excitation imposes a spatial structure on the plasma density profile. At large radial positions, the effect of the radial boundary is seen, particularly in the higher pressure case. At a lower gas pressure (50 mTorr), the maximum of the density profile is found in the tile-centre, whereas, tile-tile boundary density is lower. Non-uniformity(%) can be defined as:

$$\frac{n_H - n_L}{n_H + n_L} \text{x} 100 \tag{3.1}$$

where subscripts define High and Low density values respectively [41]. As shown in Figure 3.2, on increasing power, the plasma uniformity is significantly improved. The non-uniformity improves from $\sim 24\%$ to $\sim 12\%$ at 500mTorr, and from $\sim 60\%$ to $\sim 10\%$ at 50 mTorr with increasing power. At 500 mTorr and low powers, the electron density peak is shifting toward the tile-tile boundary. However, at higher powers (1 kW and 1.5 kW), the spatial structure in electron density is highly suppressed and the discharge profile is governed by diffusion; the electron density is maximum at the centre of the discharge and decreasing toward the wall.

Power Coupling Mechanisms in Multi-tile VHF system

As discussed in Section 1.2, RF CCP discharges are mostly sustained by two types of heating mechanisms; ohmic heating due to electron-neutral collisions, and stochastic heating which is due to momentum transfer from moving sheaths. In a 13.56 MHz argon CCP, Godyak et al [6] experimentally investigated the transition from collisional ohmic to stochastic heating with decreasing pressure, and showed

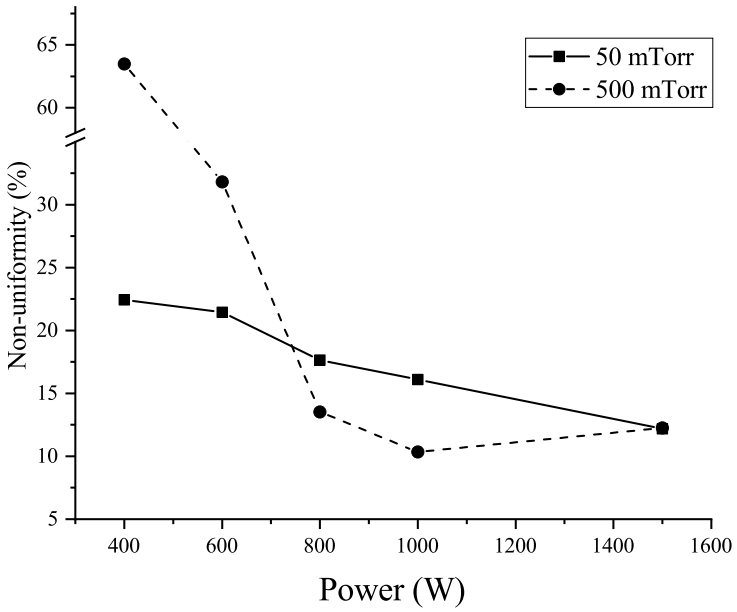

Figure 3.2: Plasma uniformity as function of VHF power.

a concurrent increase in electron density. In the following, we will evaluate the ratio of stochastic to ohmic heating in PASTIS. Starting with Equation 1.12 and following the extensive analytical solutions by Lieberman [4], the ohmic heating power per unit area is expressed as:

$$\bar{S}_{ohm} = 1.73 \left[\frac{m}{2e}\right] \left[\frac{n_s}{n_0}\right] \epsilon_0 \omega^2 \upsilon_m T_e^{\frac{1}{2}} V_1^{\frac{1}{2}} d \tag{3.2}$$

where n_s and n_0 are the electron density at the sheath edge and bulk electron density respectively, V_1 is the RF sheath voltage, υ_m is the electron-neutral collision frequency and d is the plasma bulk thickness. Again following [4], the stochastic heating power per unit area is:

$$\bar{S}_{stoc} = 0.45 \left[\frac{m}{e}\right]^{\frac{1}{2}} \epsilon_0 \omega^2 T_e^{\frac{1}{2}} V_1 \tag{3.3}$$

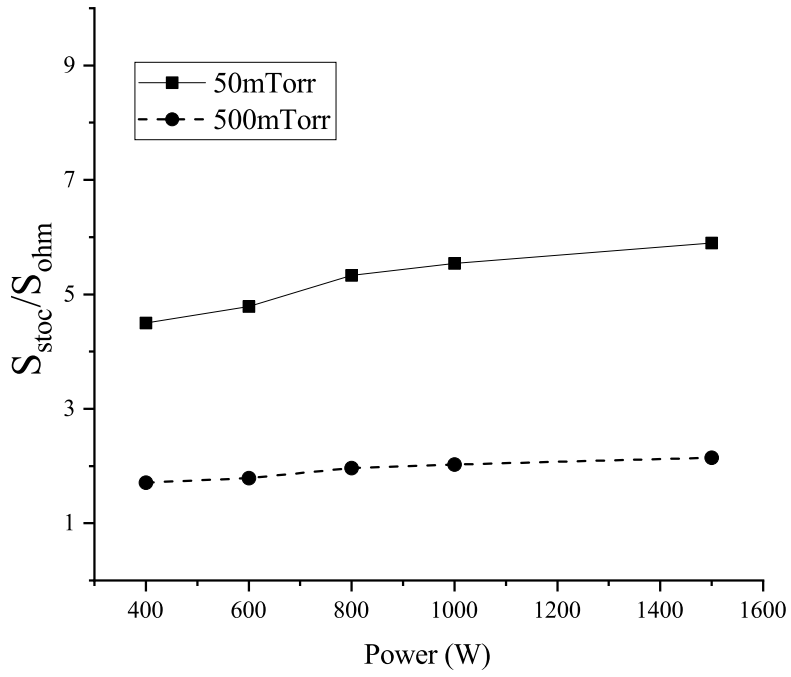

Figure 3.3: Stochastic to Ohmic heating ratio in VHF N_2.

The ratio of stochastic to ohmic heating can thus be expressed as:

$$\frac{\bar{S}_{stoc}}{\bar{S}_{ohm}} = 0.52 \left[\frac{e}{m}\right]^{\frac{1}{2}} \frac{V_1^{\frac{1}{2}}}{hdv_m} \tag{3.4}$$

where $h = {}^{n_s}/_{n_0}$. Although the above expression appears independent of driving frequency, for a constant power, V is strongly frequency dependent, and sheath width (therefore d) is weakly dependently. Furthermore, the electron-neutral collision frequency υ_m is a function of electron temperature, which varies with driving frequency. Sugai et al [26] reported on this frequency effect, and experimentally showed heating mode transitions in the frequency range 13.56-60 MHz, under constant RF voltage conditions.

To evaluate the heating mechanism in PASTIS, the value of discharge voltage for the corresponding RF power is measured using a high-voltage probe, as described

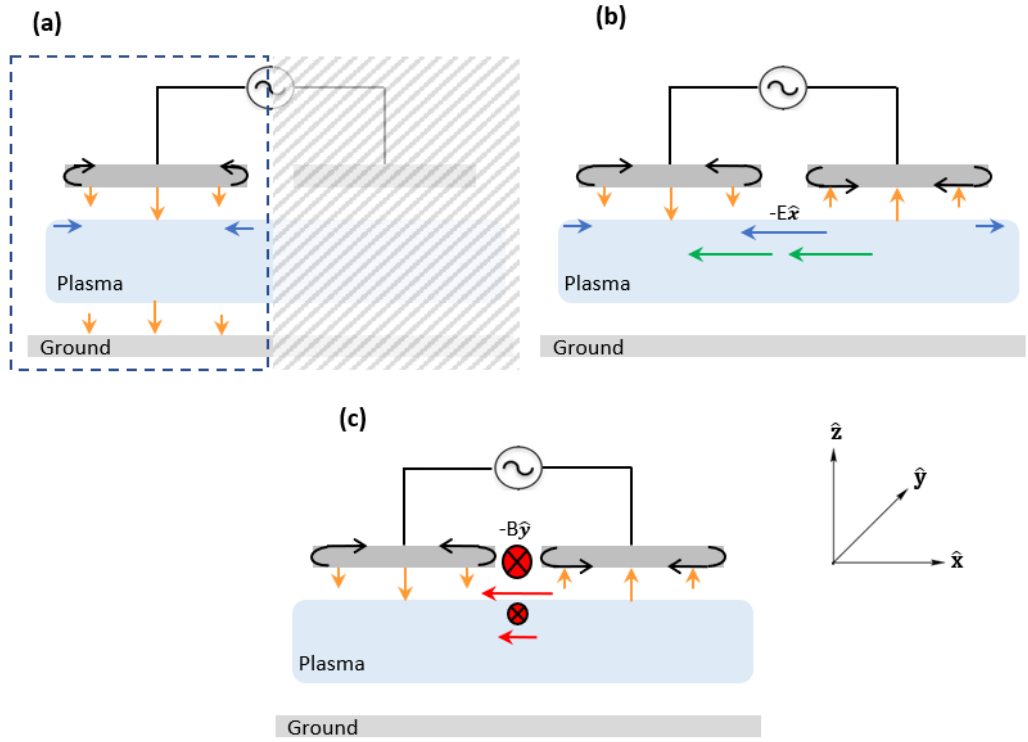

Figure 3.4: Schematic of currents in VHF multi-tile electrode plasma system (a) considering one isolated electrode tile (b) a 2-tile push-pull system (c) inductive B-field between tile-tile boundary.

in Section 2.3. The ratio of electron density at the sheath edge to the plasma bulk, $h = {}^{n_s}/_{n_0}$, is estimated as [112]:

$$\frac{n_s}{n_0} = 0.86\left[3 + \frac{d}{2\lambda_i}\right]^{-\frac{1}{2}} \tag{3.5}$$

where λ_i is the ion-neutral mean free path. The plasma bulk thickness is $d = l - 2s$, where l is the discharge gap, and the sheath thickness is estimated as:

$$s = 0.6\lambda_D\left[\frac{2V_1}{T_e}\right]^{\frac{3}{4}} \tag{3.6}$$

where the Debye length λ_D is determined from the measured n_e and estimated

T_e of 2 eV. The electron-neutral collision frequency is calculated as:

$$\upsilon_m = \overline{\nu}_e \sigma_g n_g \tag{3.7}$$

where $\overline{\nu}_e$ is the mean electron speed, σ is the collisional cross section [113, 114] and n_g is the neutral gas density. Figure 3.3 presents the $\bar{S}_{stoc}/\bar{S}_{ohm}$ ratio for VHF N_2 discharge as a function of power at 50 and 500 mTorr. For all conditions the ratio is greater than 1. Thus $\bar{S}_{stoc}$ dominates over $\bar{S}_{ohm}$, which enables more ionisation in the bulk and increased plasma density with power.

To understand the changes in the n_e-profile (and improvement in uniformity) with power and pressure, we consider the geometry of the multi-tile electrode system and VHF CCP excitation. Consider first one electrode tile isolated from the other tiles in the array, as shown in Figure 3.4 (a). This looks like a symmetric CCP plasma. VHF currents ($I\widehat{x}$) flow on the surface of the electrode (skin depth, Equation 1.19, at VHF $\approx$ microns, much less than the electrode thickness), and displacement currents flow through the driven sheath and out of the plasma at the opposing sheath at the grounded boundary. For a system driven at >10MHz, this would result in a capacitive sheath and a sinusoidal plasma potential oscillation, $\tilde{V}_p \sim \frac{V_{\text{pk}}}{2}(\sin\omega t)$, in contrast to a sub 1 MHz driven electrode which results in a resistive sheath, and a $\tilde{V}_p$ following the positive excursions of the driving voltage ($V_{\text{pk-pk}}$) [115, 116].

Now consider an adjacent electrode tile driven at 180^o relative voltage oscillation, Figure 3.4 (b), which leads to $\tilde{V}_p \sim \frac{V_{pk}}{2}(\sin\omega t + \pi)$. For this two-tile "system", there would be an electric field parallel to the surface of the tiles (-$E\widehat{x}$) caused by the spatial variation in $\tilde{V}_p\widehat{x}$ (due to π phase difference between the tiles). However, for $\omega \ll \omega_{pe}$ (the electron plasma frequency), the plasma cannot support large gradients in $\tilde{V}_p\widehat{x}$. Depending on the spatial separation between tiles, the plasma height (in $\widehat{z}$) and the plasma conductivity (in $\widehat{x}$), the $\tilde{V}_p\widehat{x}$ variation will be shorted out by plasma currents $I_p\widehat{x}$. The scale length of these currents ($I_p\widehat{x}$) at the tile-side boundary of the plasma scale (inversely) with λ_D. Additionally, current density flowing on the electrode surface ($I\widehat{x}$ scaling with tile "radius") results in $B\widehat{y}$ that drive image currents (-$I\widehat{x}$) in the plasma adjacent to

the sheath.

Note that the electrodes driven by the PSTLD are floating. This means they can acquire a negative DC bias and as such the $\frac{dV_p}{dx}$ would be substantially reduced. The acquirement of the DC bias depends on the plasma density (from conductivity, Equation 1.13), the plasma height, and the tile size. For example, a large tile coupled to a thin, low density plasma (i.e. low conductivity in $\widehat{x}$) may result in large $\tilde{V}_p$ with each electrode coupling as a symmetric CCP plasma with current coupled to the opposing grounded surface. In contrast, if the plasma has high conductivity in $\widehat{x}$, then $\tilde{V}_p$ is small, $I\widehat{x}$ is large, and $V_{\rm dc}$ is large (and negative) with strongly driven sheaths on the tile face, and very little RF current on the opposing sheath at the grounded electrode. The development of this will suggest DC bias and "shunting currents" ($I\widehat{x}$), and will be explored in Sections 3.4 and 3.5.

An additional power coupling mechanism occurs in the VHF multi-tile electrode system. Consider the magnetic dipole between adjacent tiles (Figure 3.4 (c)) which occurs due to electrode currents flowing in opposite directions around the tile edges ($I\widehat{z}$). This magnetic dipole induces an inductive B-field (-$B\widehat{y}$) between the adjacent tile edges, directed out of the page, which penetrates into the plasma bulk. Inductive currents (red arrows) are produced in the plasma as a result of this B-field, and are in phase with the image currents in -$I\widehat{x}$. The strength of the B-field scales with I, and the spatial variation in $\widehat{z}$ scales with the size of the dipole.

In the 50 mTorr pressure case where plasma densities are above 1x10^{10}cm^{-3}, the plasma skin depth (Eq 1.20) becomes comparable to the discharge gap (in $\widehat{z}$), which is 5.5 cm in this case. Therefore, the inductive coupling due to the tile boundary dipole can play a significant role in the plasma heating near to the tile-tile boundaries. The improvement in the plasma uniformity with increasing RF power is attributed to the inductive fields present near to the tile-tile boundaries, which increases the plasma density in that region.

At 500 mTorr (Figure 3.1 (b)) and low power, the maximum electron density is observed near to the tile-tile boundary. We attribute this localized effect to an additional power coupling mechanism; enhanced electrostatic (E-S) fields parallel to the tile surfaces caused by the differential voltage between adjacent tiles.

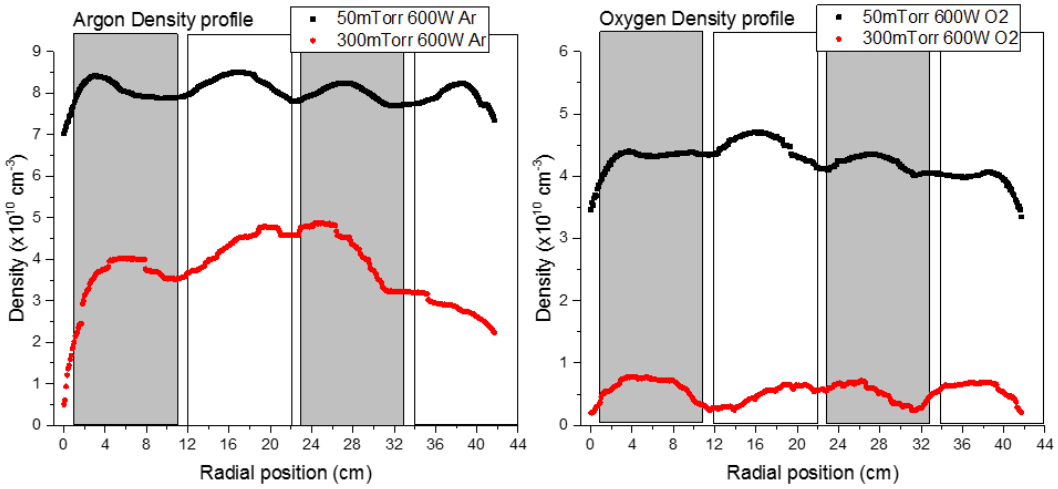

Figure 3.5: Spatial electron density profile for Ar (left) and O_2 (right) across radial 4 tiles. The shaded/blank boxes representing electrode tile(180° out of phase) boundaries.

Power into these E-S fields scale with collision frequency ($P = I^2R$), and the amplitude of the axial ($\widehat{z}$) component of the (E-S) dipole falls off as $(^{10\text{mm}}/_{z})^2$ where 10 mm is the characteristic dipole length, defined by the inter-tile spacer. At 500 mTorr and low power, collision frequency and sheath width ($\widehat{z}$) increase, such that the localized E-S power deposition observed at the tile-tile boundary is comparatively more important than capacitive coupling (via displacement currents $I_d \propto V \cdot C_{sh}$ into the bulk). However, as RF power increases, the electron density at the tile centre increases at a faster rate than for the tile-tile boundary regions. The density profile becomes flatter, as is observed at RF powers $\geq$ 1kW. As such, at higher pressures and power, the VHF multi-tile n_e-profile becomes diffusion dominated rather than one governed by the geometry of the electrode system.

The above explanation for centre dominated to edge dominated density peaks shifting with increasing pressure is also observed in Ar and O_2, as shown in Figure 3.5 for pressures of 50 and 300 mTorr at a power of 600 W. The spatial profile in Figure 3.5 extends across the middle row 4 tiles (as illustrated by the shaded/blank boxes), inter-tile gaps (tile edges), and towards the chamber edges on both sides where the dielectric "skirts" are located. Both discharge profiles

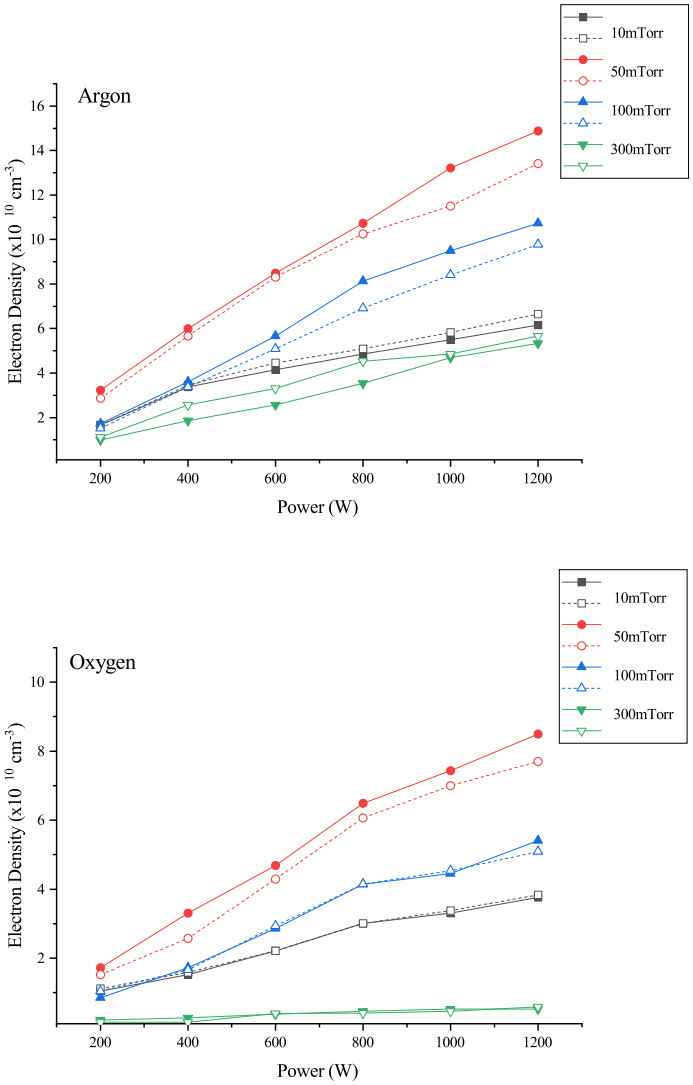

Figure 3.6: Electron density measured at the tile centre (solid shapes) and tile edge (open shapes) as a function of power for Ar and O_2.

exhibit a uniformity within 10%. Figure 3.6 plots the plasma density variation measured at tile centre and tile edge, in Ar and O_2, as a function of power for pressures 10-300 mTorr. For each pressure condition, the electron density in-

creases which is due to increased power dissipation into the plasma by enhanced stochastic heating at VHF.

The electron density as a function of pressure (10-300 mTorr) at a power of 1000 W is shown in Figure 3.7. For both gases, Ar and O_2, density initially increases (from 10-50 mTorr) and then decreases up to 300 mTorr. However, in O_2 the density decreases by 95% from 50 to 300 mTorr compared to a 65% decrease in Ar for the same pressure increase. This trend is also depicted in Figure 3.5 from 50 to 300 mTorr at 600 W power. To understand these variations in electron density, we consider a volume-average (global) model of the plasma chemistry, as developed by [117]. The global model captures scalings of plasma parameters with control parameters through the use of particle and power balance equations. To a first approximation, electron temperature is a function of pressure and geometry of the system (particle balance equation), and density is proportional to the input power (power balance equation). Specifically electron density is predicted by equating the power delivered to the plasma to the rate at which energy is lost due to collisions and outflux of particles to the walls, and can be expressed as [118]:

$$n_e = \frac{P_{abs}}{eu_B A_{eff} \varepsilon_L} \tag{3.8}$$

where P_{abs} is the absorbed power, A_{eff} is the effective area for particle loss, and ε_L is the collisional energy loss per electron-ion pair. The factor ε_L is directly related to the number of available energy-loss channels of neutral species. In the case of a molecular gas (O_2), electron-neutral collisions can result in electron energy losses and excitation of the heavy particle into an electronically, vibrationally, or rotationally excited state. For an atomic gas (Ar) there are no vibrational or rotational states available. Therefore the energy losses are higher in O_2, which results in a larger decrease in n_e compared to Ar.

The initial increase, and subsequent decrease of n_e with pressure for both Ar and O_2 is due to competing factors in Equation 3.8; ε_L and the effective loss area A_{eff} (dependent on ion-neutral mean free path λ_i). The energy loss per electron-ion pair is an increasing function of pressure, while the effective loss area

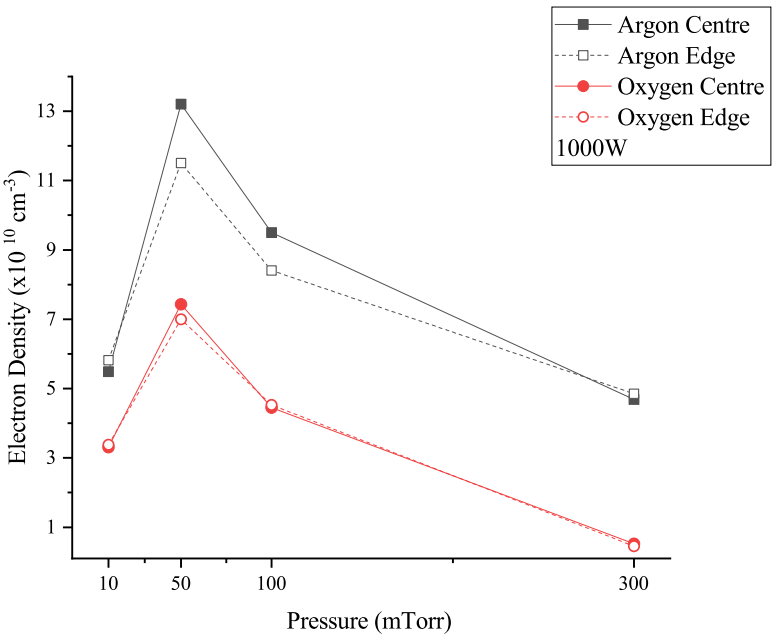

Figure 3.7: Electron density measured at the tile centre (solid shapes) and tile edge (open shapes) as a function of pressure for Ar and O_2 at power of 1000 W.

is a decreasing function of pressure (ions are more confined at higher pressure). From the trend in Figure 3.7, as the pressure increases above 50 mTorr, the ε_L factor dominates over the A_{eff} factor.

3.3 VHF Discharge non-Equilibrium

OES spectra in N_2 have been analysed to determine rotational and vibrational temperatures in VHF discharge. Figure 3.8 shows the resulting rotational temperature of N_2 in PASTIS. Error bars are introduced based on the chi-square fit between the experimental and the simulated spectra (Section 2.7). It is observed that the measured T_{rot} values are slightly above room temperature (~350-450 K) for all operating conditions. The effect of RF power and gas pressure on the rotational temperature is minimal, mostly within the error bar of ±30 K. At 50 mTorr gas pressure, a slight difference in the rotational temperature is observed between

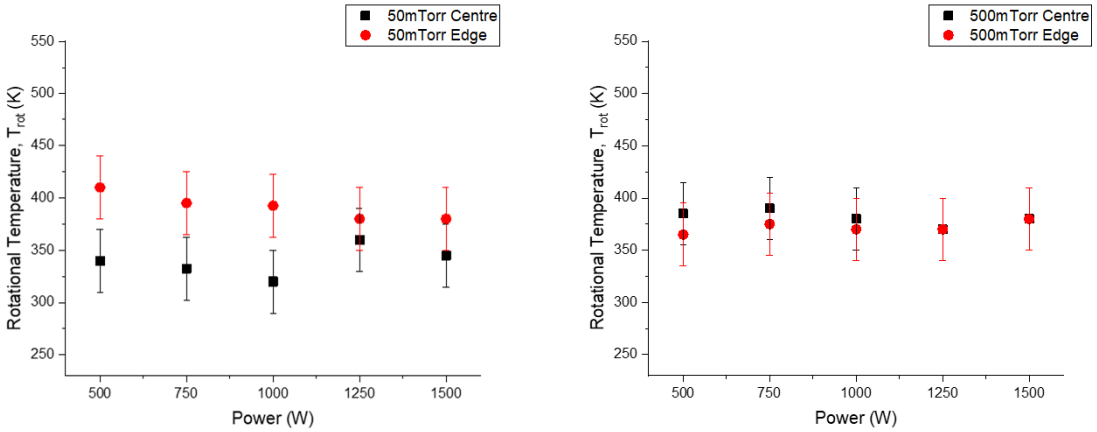

Figure 3.8: Rotational temperatures(T_{rot}) measured at tile centre and tile edge as function of power for pressures 50 and 500 mTorr.

tile centre and tile edge. This difference is higher at low RF power and consistent with lower electron density near to tile edge when compared to tile centre (Figure 3.1 (a)). The low density implies lower EEDF tail population and lower local ionization. It is observed that the difference is lower at higher RF power, which is due to the increase in inductive heating near to the tile edge as explained in Section 3.2. The inductive heating will further increase the electron energy above ionization threshold and will produce a two-temperature EEDF. This effect will reduce the electron population available for gas heating and thus the difference in the temperature decreases with increasing RF power. At a gas pressure of 500 mTorr the rotational temperature is nearly the same at the tile centre and tile edge. The mean free path for rotational equilibrium scales inversely with gas pressure such that the molecule-molecule collision frequency reduces the temperature difference [119].

OES analysis to determine the vibrational temperature of N_2 is shown in Figures 3.9 and 3.10. Figure 3.9 shows the resulting plot of $ln\left[\frac{I_{\upsilon'-\upsilon''}}{A_{\upsilon'-\upsilon''}}.\lambda\right]$ versus $E_\upsilon - E_0$ for each $\Delta\upsilon$=-2 transition at 50 mTorr. The data aligns well with the Boltzmann plot; correlation coefficient for all experimental data was $\geqslant$0.89. As such, calculation of T_{vib} from the Boltzmann distribution of the $C^3\Pi_u$ is valid. Figure 3.10 shows the T_{vib} values as a function of power and gas pressure at both tile centre and tile edge. T_{vib} increases with both power and pressure and this

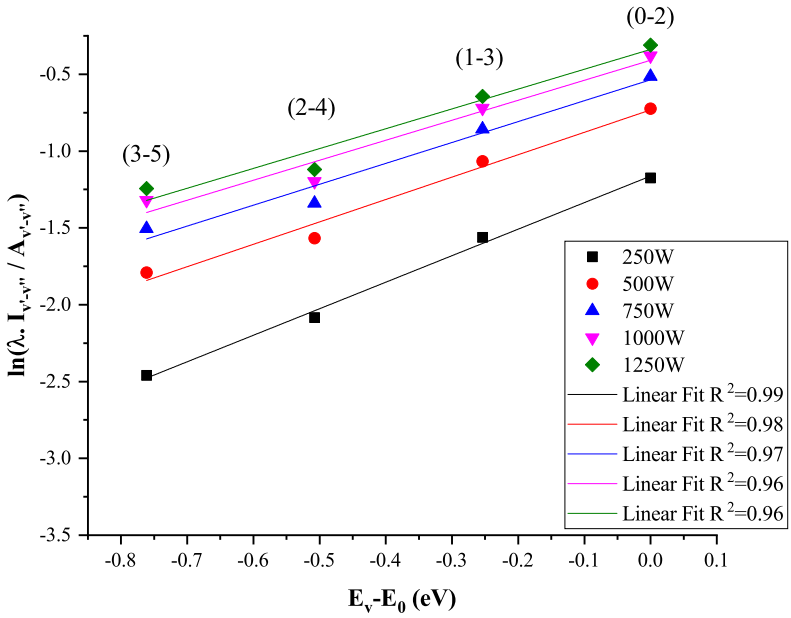

Figure 3.9: Boltzmann distribution fit of excited $C^3\Pi_u$ states for T_{vib}.

variation is similar for both tile centre and tile edge. The corresponding vibrational temperatures vary in the range ∼6250-9400 K.

The vibrational temperature is related to the vibrationally excited state ($C^3\Pi_u$) densities and can be expressed as [120]:

$$N_2(C, \upsilon') = n_e N_2(X, \upsilon) k_\upsilon \tag{3.9}$$

where N_2(X,υ) is the ground state density and k_υ is an excitation rate constant. This is valid when excited states are mostly populated by the electron impact excitations:

$$N_2(X^1\Sigma_g) + e \rightarrow N_2(C^3\Pi_u) + e$$

rather than cascade transitions or excitation from other states, such as metastable states. As reported by [121, 122], excitation and energy pooling from metastables state ($A^3\Sigma_u^+$) results in an overpopulation of the ($\Delta\upsilon$ = 1-3) transition. The increased significance of the metastable excitation channel was attributed to

EEDF changes, where in the systems reported by [121, 122], the high energy tail becomes depleted at high pressure, and the direct excitation channel from the ground ($X^1\Sigma_g^+$) to the excited ($C^3\Pi_u$) state is suppressed. As shown in Figure 3.9, we do not see any overpopulation, therefore suggesting minimal contributions from metastables affecting population statistics. Furthermore, for our pressure conditions, the $N_2(C^3\Pi_u)$ state is also unaffected by quenching processes due to its short radiative lifetime ($\tau_{RAD} \sim 37$ ns)[123]. As such an increase in the vibrational temperature is governed by rise in plasma density with power, which causes an increase in the production rate of the vibrationally excited nitrogen molecules. The rate of T_{vib} increase with power also matches that of the electron density, i.e. larger rate of increase at 500 mTorr compared to 50 mTorr (Figure 3.1). An increase in T_{vib} with power has also been reported elsewhere [124, 125]. In a dual-frequency CCP study by Huang et all [91], the T_{vib} dependence on power increase was compared for LF(2 MHz) and HF(41 MHz), such that T_{vib} for VHF=41 MHZ increased almost linearly with power(as observed in our VHF PASTIS), where as for LF=2 MHz, T_{vib} essentially did not change. This can be explained by the relation $p_i/p_e \propto 1/\omega^2$, where p_i and p_e is power to ions and electrons respectively.

With an increase in gas pressure, the neutral gas density increases. As shown in Figure 3.1, the plasma density decreases (∼70%) from 3x10^{10} cm^{-3} at 50 mTorr to 0.8x10^{10} cm^{-3} at 500 mTorr at 1500 W power. However, the rise in neutral density is higher as compared to the decrease in plasma density in this pressure range. This will lead to the increase in the population of vibrationally excited molecules. Thus the vibrational temperature will increase with gas pressure, as shown in Figure 3.10.

3.4 Mode Change in VHF Multi-tile

In asymmetrical CCPs, as discussed in Section 1.4.2, the smaller electrode is usually powered and the larger electrode is grounded. For a small volume system driven at low frequency, this results in the voltages (and therefore the ion energies) across each electrode being different. This is due to a DC self-bias developing

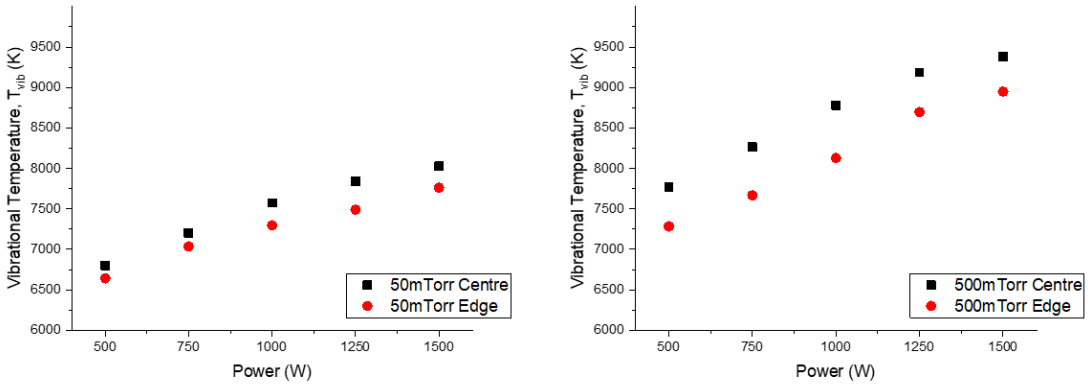

Figure 3.10: Vibrational temperatures(T_{vib}) measured at tile centre and tile edge as function of power for pressures 50 and 500 mTorr.

on the smaller powered electrode and a reduced voltage drop results across the larger grounded electrode. However, if this type of system is scaled to larger areas (for large-area wafer processing or roll-to-roll manufacturing), the ability to achieve (voltage) differences between the two electrodes becomes much more difficult, and is no longer possible in a controlled manner. Note that the large-area VHF driven PASTIS reactor resembles an almost symmetric CCP. The adjacent separation between the tiles in the multi-tile array is much smaller than the tile area and side walls are insulated; the ratio of the powered-tile area to the grounded electrode area is 80%. However, in the multi-tile array the adjacent tiles are powered differentially. It is unclear, a priori, whether the powered multi-tile array acts as a single electrode with different phases across the driven sheath, or if each tile behaves like a small individual electrode in a large (grounded electrode) chamber. In this work, some of the first detailed investigations will be presented to understand what the VHF driven multi-tile discharge is delivering to a substrate that would be located at the grounded electrode side.

Consider the two-tile system in Figure 3.11. In normal CCP operation, there is plasma resistance R. For a push-pull fed multi-tile system, the currents from one tile are out of phase with adjacent tile. Following from the discussion in Section 3.2, this results in a current path through the plasma, with a resistance $R_{inductive}$, and is shown in Figure 3.11. The inductive moniker arises because the currents are parallel to the boundary, the same as in ICPs. With this in mind, the

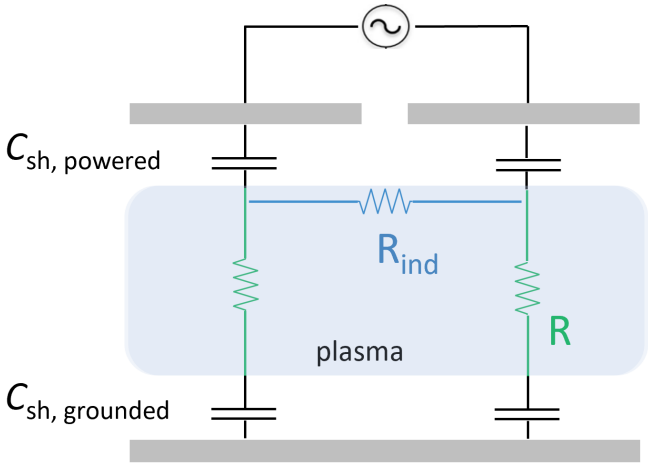

Figure 3.11: Schematic of resistance pathways in differential multi-tile system.

current density, and therefore the voltages across the sheath at the powered side ($C_{sh,powered}$) may be different to the grounded side ($C_{sh,grounded}$). This "modeled system" will be the basis of our interpretation of the following results.

In a low-pressure (10 mTorr) oxygen discharge condition, we find changes in the operational mode and infer changes in the power coupling mechanisms with increasing power. To test this, we ramp power which, as detailed from the previous Section 3.2, gives a linear increase in density. This should change the conductivity of the plasma and will also change parameters in the self-consistent sheaths both at the powered tiles and at the grounded electrode. First, current and voltage is measured at one powered tile (Section 2.3). Note that the dissipated power scales as:

$$P = \frac{1}{2}(I_{circulated})^2 \cdot R \tag{3.10}$$

where I is the discharge current and R is the resistance, which is made up of the series resistance of the wires and the distribution in the power-splitter, plus the plasma resistance ($R = R_{wires,PSTLD} + R_{plasma}$). The relationship between current and voltage scales with the impedance $Z = R + Im(Z)$ with real part resistance R. Accounting for power division among the tiles, the power dependence of the

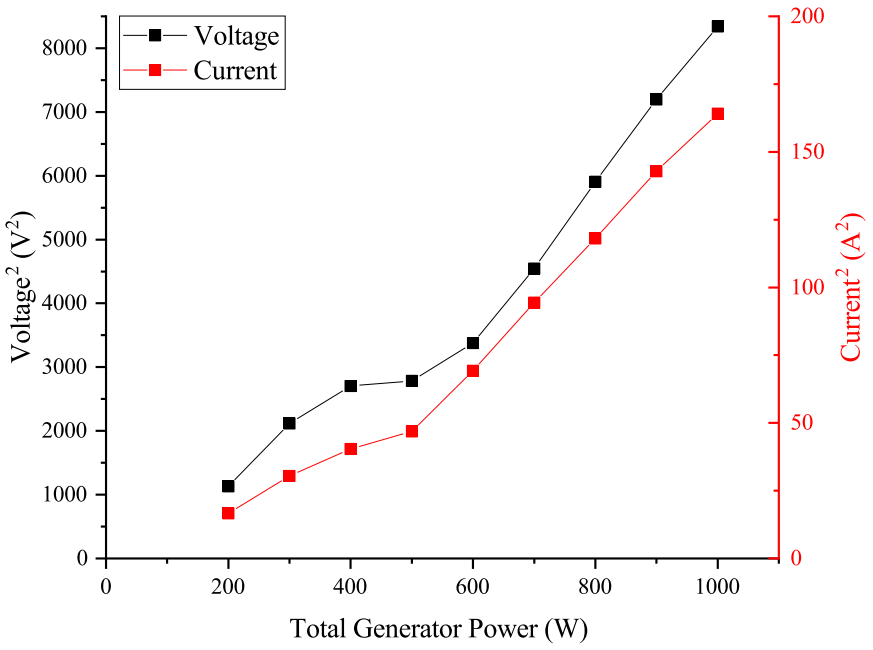

Figure 3.12: Current and voltage measured at one tile in the powered mult-tile electrode as function of generator power in 10 mTorr O_2.

resistance is therefore:

$$R(P) = \frac{1}{6} \cdot \frac{P}{I^2} \tag{3.11}$$

Figure 3.12 plots the square of the measured peak voltage and current (from one powered tile) versus delivered generator power in 10 mTorr O_2. Up to 500 W the resistance is constant with a value of approximately 1.75 Ohm. The experimental current values for O_2 10 mTorr in Figure 3.12 are reproduced in Figure 3.13, along with expected theoretical values of current for a constant resistance of 1.75 Ohm. There is a distinct kink in the curve, with R values (obtained from the slope, and projecting back to (0,0)) decreasing with increasing power. Careful observation of these experimental values and trend, suggests a piecewise smooth transition, without any hysteresis or observable jump. This is in contrast

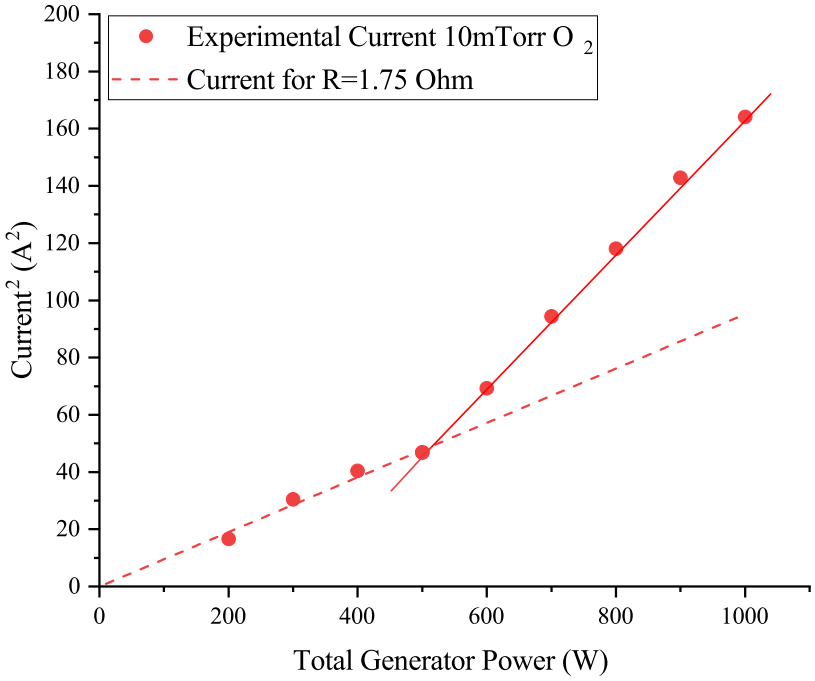

Figure 3.13: Experimental measured current in 10 mTorr O_2 and theoretical values of current for a constant resistance of 1.75 Ohm.

to transitions often seen in E-to-H transitions in ICP systems[126], or E-H-W coupling modes in Helicons[127], or mode-hoping as seen in RSLA (radial slot-line antennae)[128].

At higher powers, we note the linear behaviour and we suggest local differential resistances for this piece-wise linear section. Referring to Figure 3.11, we consider that the current in the plasma is now splitting into two paths (through R and $R_{inductive}$). Across the transition, the $R_{inductive}$ provides a lower-real-resistance pathway between adjacent tiles. We believe that this is due to an increase in plasma conductivity and thus in the plasma current in the $\hat{x}$ direction, the direction of inductive currents. This data implies a mode transition versus RF power in the discharge.

The mode transition can be expected to directly affect bulk plasma parameters. To investigate this, Figure 3.14 shows the measured electron, positive, and

negative ion density versus RF power. The electron density is measured by hairpin probe. The positive ion density (n_+) follows directly from measured ion-flux density (J_+), from planar flux probe;

$$n_+ = \frac{J_+}{eu_B} \tag{3.12}$$

where u_B is given by Equation 1.11. For the calculations here, we assumed O_2^+ to be the dominant ion and T_e is fixed at 2 eV. The negative ion density is calculated from the quasi-neutral condition $n_- = n_+ - n_e$, and the analysis is based on the method described in [129]. A calibration between the absolute-electron density of the hairpin probe and ion-flux probe is performed in electropositive argon (This data is supplied in Appendix A).

Distinct changes in the density trends are observed around the mode transition. As shown in Figure 3.14, n_+ increases linearly with power, with a change in slope at 600 W: n_e increases monotonically with power, with concave-up profile up to 800 W, and linear above. The negative ion trend shows ∼33% rise in density with an increase in RF power up to 600 W and then decreases with a further increase in RF power. The corresponding electronegativity, $\alpha = {}^{n_-}/_{n_e}$, is decreasing from 1.1 at 200 W to 0.3 W at 1000 W.

Analysing Figure 3.14 in more detail, the negative ion density trend can be explained based on its production and loss mechanisms in the discharge. The main production mechanism of negative ion density is dissociative electron attachment

$$O_2(X^3\Sigma_g^+) + e \rightarrow O^- + O(^3P) \qquad (R1)$$

with a reaction rate $R = k_1 n_e n_{O_2}$, where k_1 is the reaction rate coefficient [130]. The dominant loss mechanisms are positive ion-negative ion neutralisation and electron collisions with negative ions (electron impact detachment) [131]

$$O^- + e \rightarrow O(^3P) + 2e \qquad (R2)$$

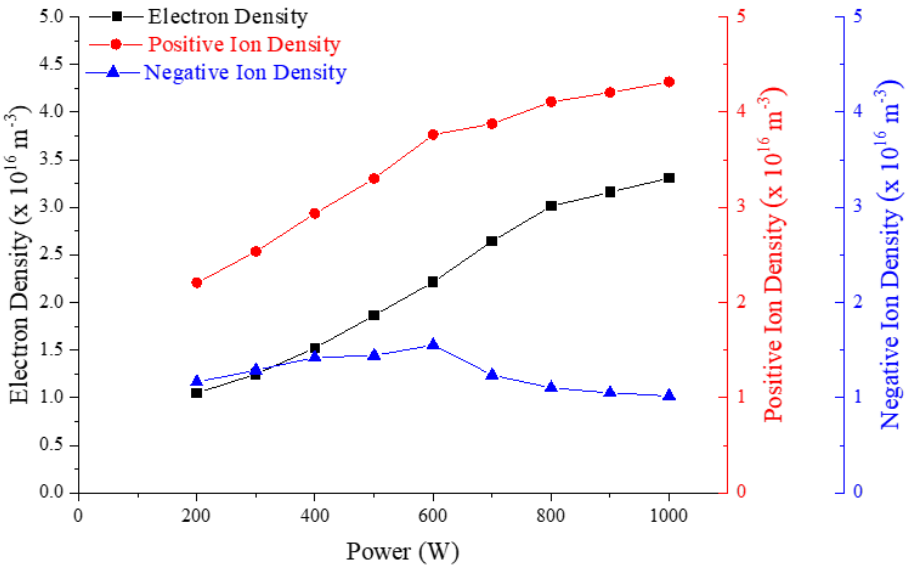

Figure 3.14: Electron density, positive ion density, and negative ion density as function of power in 10 mTorr O_2.

with a reaction rate $R = k_2 n_e n_-$, where k_2 is the reaction rate coefficient [130]. An initial (up to 600 W) increase in negative ion density suggests the discharge is dissociate attachment dominated. This process is a resonant, low-energy dominant process, particularly for vibrationally excited O_2 [132]. A further increase in RF power increases the positive ion density and therefore loss mechanism via ion-ion neutralisation increases. Additionally, increasing electron density further increases the destruction of negative ions by electron impact. The electron impact neutralisation of O^- is a comparably high energy process peaking at 10's of eV [133]. These electrons are high energy electrons which are generated near/in to the powered sheath. As shown in Figure 3.12, after mode transition the electrode voltage increase with RF power and hence sheath width, will increase the sheath velocity responsible for high energy electrons via stochastic heating. The combination of both, i.e. positive ion-negative ion neutralisation and electron impact neutralisation, drives the discharge in loss dominant mode at higher RF power.

Figure 3.15 plots the IEDs for O_2^+ as a function of power. Overall, the single-peak symmetry observed in Figure 3.15 is an indication of a collisionless regime in VHF with thin sheaths, in contrast to IEDs with an extendend tail of low

energy ions usually observed in low frequency RF plasmas [134]. We note that V_{rf} can be small, and on the same order as the V_{DC} for an unpowered sheath. For a high-frequency (capacitive) sheath the resulting ion energy peak has two dependencies, one to preserve the charge-neutral flux (standard plasma potential rise above the boundary), and a seconds resulting from the plasma potential oscillation ($\tilde{V}_{plasma}$) in the region above the sheath;

$$E_{ion,peak} = \mathcal{F}(T_e, m_i) + \frac{\tilde{V}_{plasma}}{2} \tag{3.13}$$

In symmetric CCP, $\tilde{V}_{plasma} \approx {}^{V_{rf,peak}}/_{2}$, as the drive voltage is split between the two series sheaths.

As discussed in Section 1.2.5, the two main factors determining the shape and distribution of the ion energies in RF discharges are sheath collisions and the ratio of the ion transit time τ_{ion} to the RF period τ_{rf}. The shape of the IEDs correlate with different regimes of ion transport across the RF-driven sheath. In the collisionless sheath regime the ion mean free path (λ_i) is larger than the sheath width (s) and the final energy of the bombarding ions is dictated by the time average sheath potential ($\bar{V}_s$). Sheath width decreases with driving frequencies due to increased plasma density such that the collisionless regime ($s \leq \lambda_i$) is still maintained at moderate pressures. For the 10 mTorr O_2 condition, $\lambda_i (= 5\,\text{mm})$ is estimated to be at least 5 times larger than the sheath width (Equation 3.6). Conversely in a collisional sheath, ions lose energy through elastic and/or charge-exchange collisions as they transverse the sheath. These results in a broader spread of energies and additional secondary peaks at lower energies respectively. These secondary peaks are due to the RF modulation of the sheath potential combined with the creation of thermal ions by charge exchange processes.) In the high frequency regime, when ${}^{\tau_{ion}}/_{\tau_{rf}} >> 1$, the phase in which the ions enter the sheath becomes irrelevant and the resultant IED is single-peaked, such is the case for 162 MHz.

Analyzing the data in Figure 3.15, the location of the energy peak is monotonically increasing with power up to 600 W, and decreases thereafter. As shown from Figure 3.12, above 600 W, the tile current and voltage both increase. The

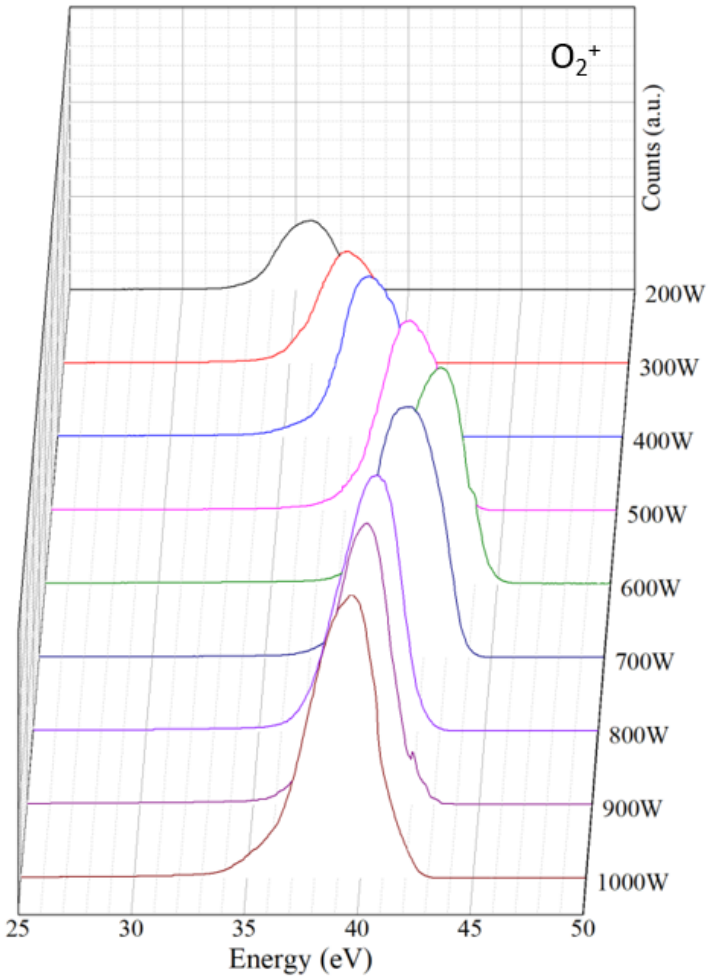

Figure 3.15: Ion energy distributions (IEDs) measured at the grounded electrode for O_2^+ as function of power at 10 mTorr O_2.

decreasing ion-energy peak above 600 W means there is reduced $\tilde{V}_{plasma}$ at the sheath-edge on the grounded side and thus reduced RF-current density in the grounded-side sheath. Due to current-conservation, there must be an increase in RF plasma current in the $\hat{x}$-direction between the plasma-regions associated with adjacent tiles, as discussed earlier referring to Figure 3.11. Following from the discussion in Section 3.2, we note that in a conventional symmetric CCP, the flow of displacement current at the powered sheath results in a $\tilde{V}_{plasma}$ in the bulk, and RF current out of the plasma at the (opposite) grounded surface. In the multi-tile system with differential coupling between adjacent tiles, the $\tilde{V}_{plasma}$ in

front of an individual tile is out of phase with the $\tilde{V}_{plasma}$ at an adjacent tile; displacement currents in the powered sheath can flow to the opposing ground sheath ($\hat{z}$) and "back and forth" between adjacent tiles at a RF-phase with maximum current. The current in a tile-face scales linearly with "radius" (Section 1.4.2) and, by solving Faraday's law across the conductor-vacuum (sheath edge) boundary, there is an $E_x(x,z)$ which scales with I_{tile} and is constrained by the boundary condition imposed by the grounded conductor opposite the plasma volume. With plasma, the induced field ($E_x(x,z)$ and $B_y(x,z)$) are further augmented by the skin effect (Equation 1.20); at 400 W δ_{pl} = plasma height, so increasing image current ($I\hat{x}$) in the plasma are expected with increasing power (plasma density). The B_y dipole resulting from "radial" currents wrapping around the edges of the tiles, penetrates into the plasma volume with spatial scaling associated with the dipole size (tile-tile gap), boundary condition from the ground electrode and skin depth effects (Section 3.2). Now suppose the current in the left-tile is in the $+x$, then the current in the right-tile is in the $-x$, and the induced B_y is in the $+y$ direction for both tiles, and for the tile-tile boundary dipole. Thus, the induced E_x is in the $-x$ direction across all three sections (tile radius, tile-tile gap, adjacent-tile radius). These are inductive electric fields, and currents, as they are parallel to the plasma boundary, and results in a reduction in the current density at the grounded side of the plasma volume.

At lower power n_e is low and n_- is high and R_{plasma} is (relatively) high. The ion energy measured on the grounded electrode increases with V, showing that the increasing I (and V) at the tile is also causing increasing $\bar{V}_{ground}$ (Equation 3.13) caused by current being driven through the ground sheath. This shows the plasma volumes in front of tiles behave like independent, symmetric discharges, and the plasma resistance is constant vs power. Above the transition, the electron density increases super linearly with power and the negative ion density decreases, yielding a reduced bulk-plasma resistance, and the skin depth is smaller than the plasma height. The ion energy now drops with increasing power (despite both I and V increasing, Figure 3.12); I_{ground} is not increasing, thus by current continuity there must be $I\hat{x}$ shunting between the tiles. This results in the tiles driving an asymmetric plasma as adjacent tile surfaces behave as current-return paths and thus a virtual ground surface. The ion energy remains somewhat high (38 eV)

so there must be some $I\hat{y}$ at this boundary. The plasma current now has two parallel paths, $I\hat{x}$ and $I\hat{y}$, and the overall resistive element of the plasma drops smoothly with increasing power. We note that the resistive load-line ($^{dI}/_{dV}$) is nearly constant with a value of 0.85 Ohms, and this represents the real impedance of the inductive-current path between tile regions. The continued increase in V_{rf} at the powered electrode, and not in $\bar{V}_{ground}$, implies that the tiles take on a DC self-bias. This indicates higher $\tilde{V}$, sheath width, and stochastic heating at the powered sheath. Small changes in the EEDF due to the increased hot-tail from stochastic heating and/or the diffuse inductive fields result in the reduced negative ion density. We point out that even with the positive feedback of the changes in n_- across the transition there is a piecewise smooth transition.

3.5 Electrical Asymmetry

The results presented from low-pressure 10 mTorr O_2 discharge (electrode voltage and current, charged particle density including negative ions, and ion energy), allow us to conclude that the mode transition observed across an increase in power is caused by changes in current coupling mechanisms and modification in the discharge impedance including the presence of negative ions. This power trend is not observed for other operating conditions; in higher-pressure O_2 and in electropositive Ar at low and high pressures. The IEDs as a function of power for 100 mTorr O_2 and 10 mTorr Ar are plotted in Figures 3.16 and 3.17 respectively, and show minimal increase (within 2 eV) in ion energy with power. These ion energy trends are indicative of diminished negative ions due to enhanced loss rates (in the case of high pressure O_2) and evidence of electrical asymmetry; the push-pull delivery of the PSTLD result in floating electrode tile that develop a DC bias such that the plasma potential oscillations (and therefore grounded sheath voltages and ion energies) are substantially reduced. This is in contrast to conventional symmetric CCPs, where the potential drop across both sheaths are equal and current is driven through the grounded electrode, and ion energies (from sheath voltages) increase with power [82].

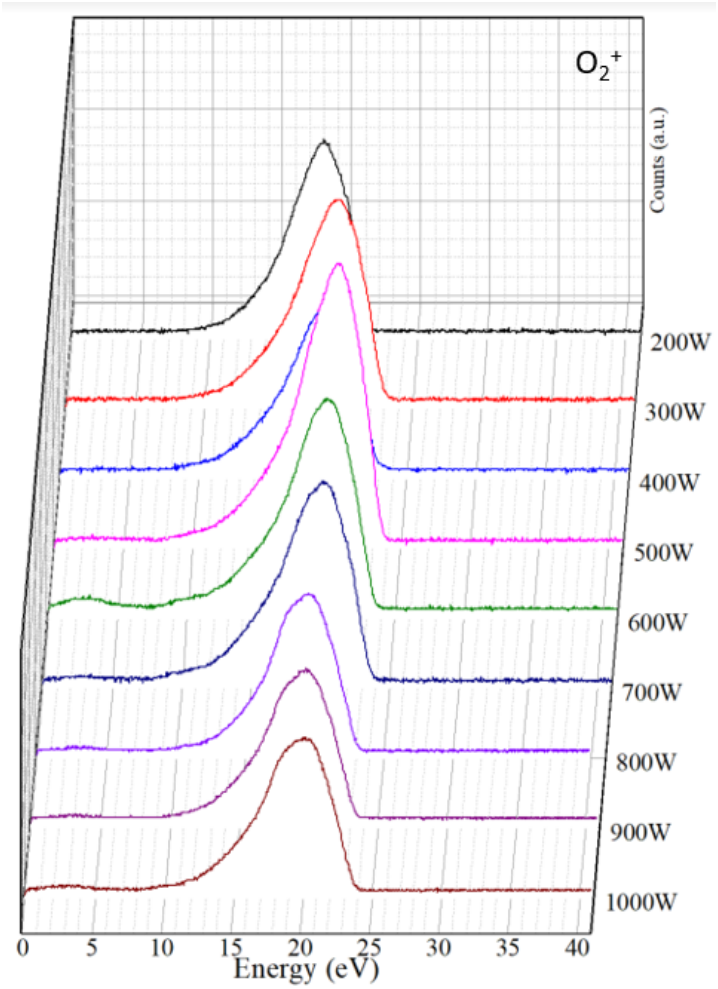

Figure 3.16: Ion energy distributions (IEDs) measured at the grounded electrode for O_2^+ as function of power at 100 mTorr O_2.

Further evidence is provided in Figure 3.18 which plots the square of measured peak voltage and current versus power in 10 mTorr Ar. In comparison to 10 mTorr O_2 case (Figure 3.12 and 3.13), there are no distinct changes in the R values; current values follow a constant resistance of ∼1 Ohm. The RF conductivity (parallel to $x-y$ plane) is sufficient to drive the shunting currents(in x), that reduce $\tilde{V}_{plasma}$ oscillations in front of adjacent tiles. Tile voltage continues to increase with power, with no RF driven enhancement of the ion energy at the grounded electrode.

Figure 3.19 plots the IEDs for pressures 10, 50 and 100 mTorr at 1000W. For

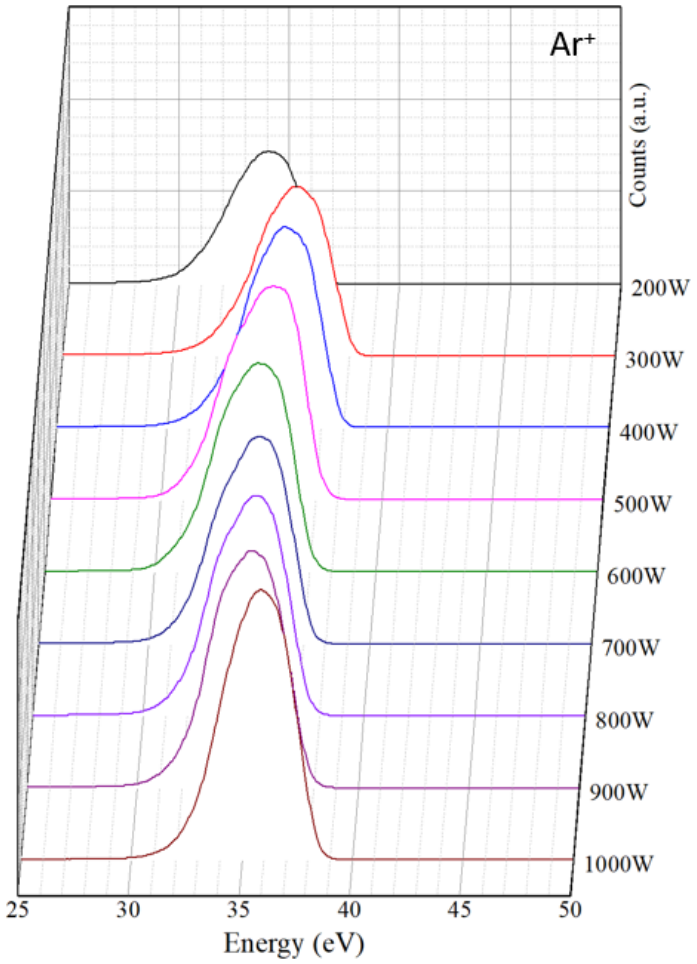

Figure 3.17: Ion energy distributions (IEDs) measured at the grounded electrode for Ar^+ as function of power at 10 mTorr Ar.

the 10 mTorr case, density (Figure 3.6) is low, so sheath width and voltage drop is (relatively) larger. A collisionless regime ($s \leq \lambda_i$) is still maintained at 50 mTorr, but increased electron density results in lower sheath voltage (width). In the 100 mTorr case, density is slightly lower than in 50 mTorr, but some broadening occurs due to elastic collisions in the sheath beginning to take effect as sheath width becomes comparable to λ_i.

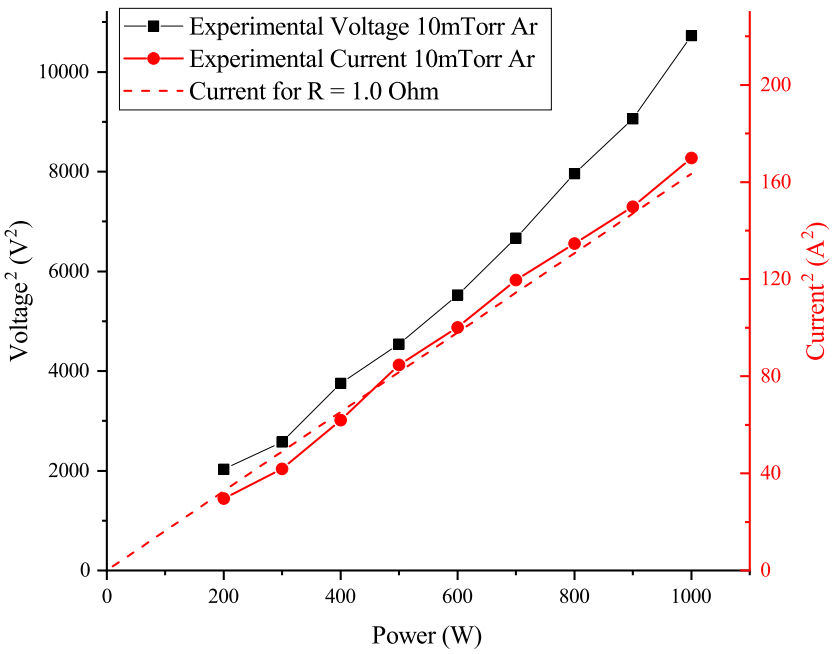

Figure 3.18: Current and voltage measured at one tile in the powered mult-tile electrode as function of generator power in 10 mTorr Ar, along with theoretical values of current for a constant resistance of 1 Ohm.

3.6 Summary

This chapter presents results of plasma dynamics and power coupling mechanisms in VHF multi-tile discharges. Plasma uniformity (from electron density), is investigated and results show edge effects can be minimized by changing power-pressure matrix; non-uniformities of within 10% are achieved.

From OES analysis, we observe high T_{vib} ($\sim$1000s K) and low T_{rot} (room temperature + <100 K), which demonstrates that the discharge is a highly non-equilibrium system. High vibrational temperature values are reported elsewhere but at the expense of high rotational/gas temperature, meaning the degree of non-equilibrium is less. Lower operating temperatures are highly desirable for

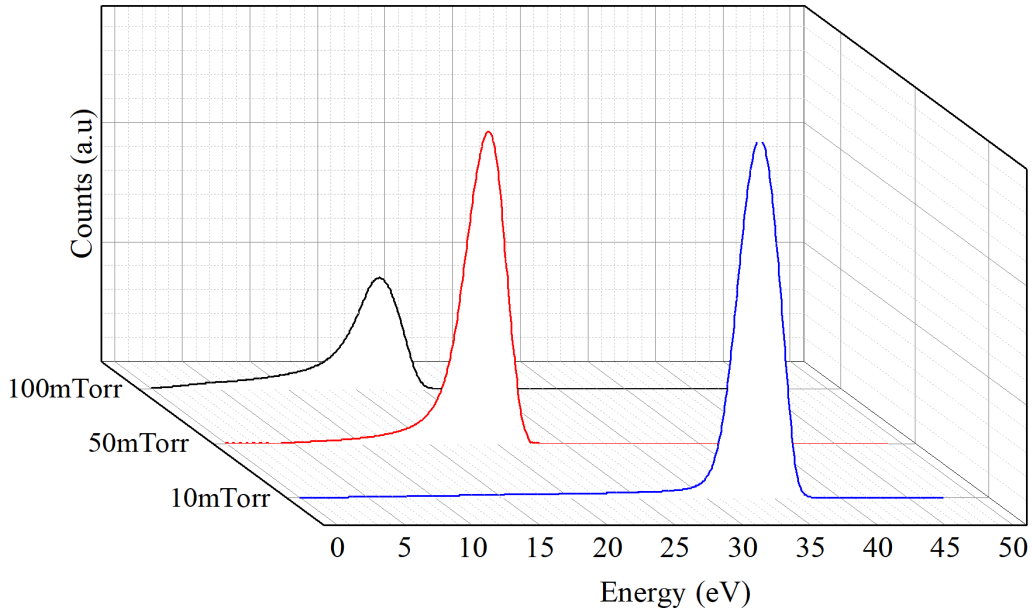

Figure 3.19: IEDs as a function of pressure in 1000 W Ar.

thin film processing, and particularly desirable in ALE for better control of the ALE thermodynamic process window. With non-equilibrium conditions in VHF, low operating temperatures can be accompanied by desirable gas chemistry and activation from high vibrational temperatures.

The large-area multi-tile PASTIS system, resembling a symmetrical geometry, is shown to achieve quasi-independence of ion flux (electron density) and ion energy (Section 3.5). The addition of a substrate bias (as in Starchief), would offer additional control of ion energy to the surface.

Chapter 4

ALE Behaviour in a 2-frequency CCP (162 MHz VHF plasma source + 27 MHz bias at wafer)

Contents

4.1 Fluorocarbon-based ALE of SiO_2

As discussed in Chapter 1, conventional plasma etch anisotropic etching is enabled by the synergistic effect of impacting neutral species and energetic ion bombardment. Even with an inhibitor layer, it is difficult to obtain reliable atomic precision because adsorption of inhibitor gas and reaction of ions occur at the same time. Specifically, the ion and neutral radical flux are linked through the plasma linking the same EEDF (electron energy distribution) and IED (ion energy distribution). In ALE, the separation of the chemical modification and subsequent etch-removal enable the fluxes of neutrals and charged particles to be independently optimised. Fluorocarbon-based ALE of SiO_2 is realised by passivating the surface with a thin fluorocarbon (FC) layer followed by (Ar) ion enhanced etching. Specifically, the deposited FC layer provides chemical species to react with the SiO_2 and removes surface layers through chemical reactions enhanced by low energy ion power deposition.

In this work, we demonstrate an ALE process with a fully self-limiting etch of SiO_2 in a large-area, low-volume, 2-frequency CCP (VHF 162 MHz CCP source + 27 MHz CCP bias). Background gas in the two steps are Ar/CHF_3 and Ar/O_2. The first section in this chapter investigates the effect of VHF and LF power coupling on plasma parameters in the modified industrial reactor *Starchief*; namely electron density from hairpin probe, relative reactive species density from OES, and ion energy effects inferred from sputter rates. These results provide insight into the operational window and favourable conditions to realise ALE behaviour of SiO_2 in our experimental system. Section 4.3 investigates, by XPS analysis, the atomic composition and chemical bonding of the fluorocarbon layers deposited with CHF_3 by the LF and VHF formed plasmas. A self-limiting ALE process of SiO_2 using cyclic CHF_3 and Ar/O_2 exposures is presented in Section 4.4.

Si substrates with nominal 900 nm of PECVD (Plasma-Enhanced-Chemical-Vapour-Deposition) grown SiO_2 obtained from ASM have been used for all experiments. For surface analysis measurements, SiO_2 samples are cut into coupons and placed on a 300 mm Si carrier wafer.

4.2 Frequency Coupling: VHF (162 MHz) and LF (27 MHz)

Figure 4.1 shows measured electron density (n_e) in a 98 mTorr $Ar/CHF_3 = 66/33$ gas mixture as a function of applied power. First we investigate the plasma density versus high-frequency power level (100-600 W) with a constant power of 10 W at 27 MHz. This demonstrates a linear plasma density versus high-VHF power level, and expected high-plasma production efficiency of the high-VHF multi-tile-CCP "plasma source". In contrast, variation in 27 MHz power level (50-600 W) at a fixed VHF power level of either 200 W or 400 W, results in nearly constant plasma density. Thus, plasma density is nearly decoupled from the LF power, demonstrating the separation of high-VHF giving plasma formation, and the LF (27 MHz) coupling to ion-power in the sheath [37].

The composition of fluorocarbon layers deposited in ALE is related to the

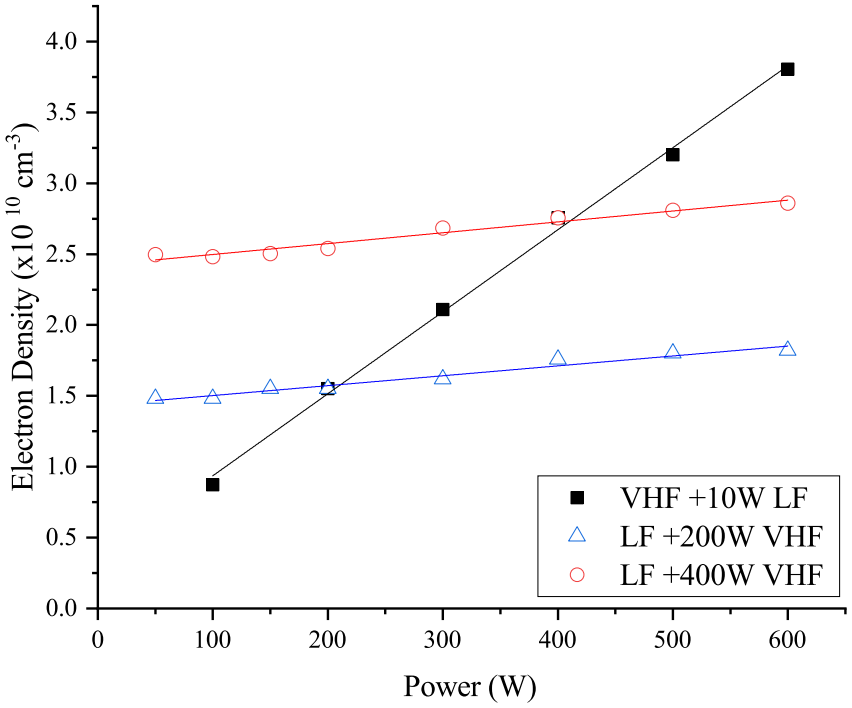

Figure 4.1: Electron density in CHF_3/Ar at 98 mTorr as a function of applied VHF power with 10 W LF (■), or as a function of applied LF power with 200 W VHF (△) and with 400 W VHF (○).

gas-phase chemistry of the plasma [135]. Low atomic F content and high CF_2 is favourable for better chamber conditions and for future studies for etch selectivity to Si_3N_4 and Si [136]. In this regard, low F concentration is critical as Si etches spontaneously in F rich environments. Figure 4.2 shows the ratio of F/Ar measured by OES in CHF_3/Ar as a function of power in either LF or VHF excited plasma, with errors bar representing measurement standard deviation. For constant pressure condition (98 mTorr), the relative density of atomic F increases with LF power but there is little effect for increasing VHF power. Electron-neutral collisions is the major pathway for fluorocarbon gas dissociation, therefore the EEDF and electron temperature directly affect the FC dissociations. The following are possible electron impact dissociation pathways generating F and CF_2

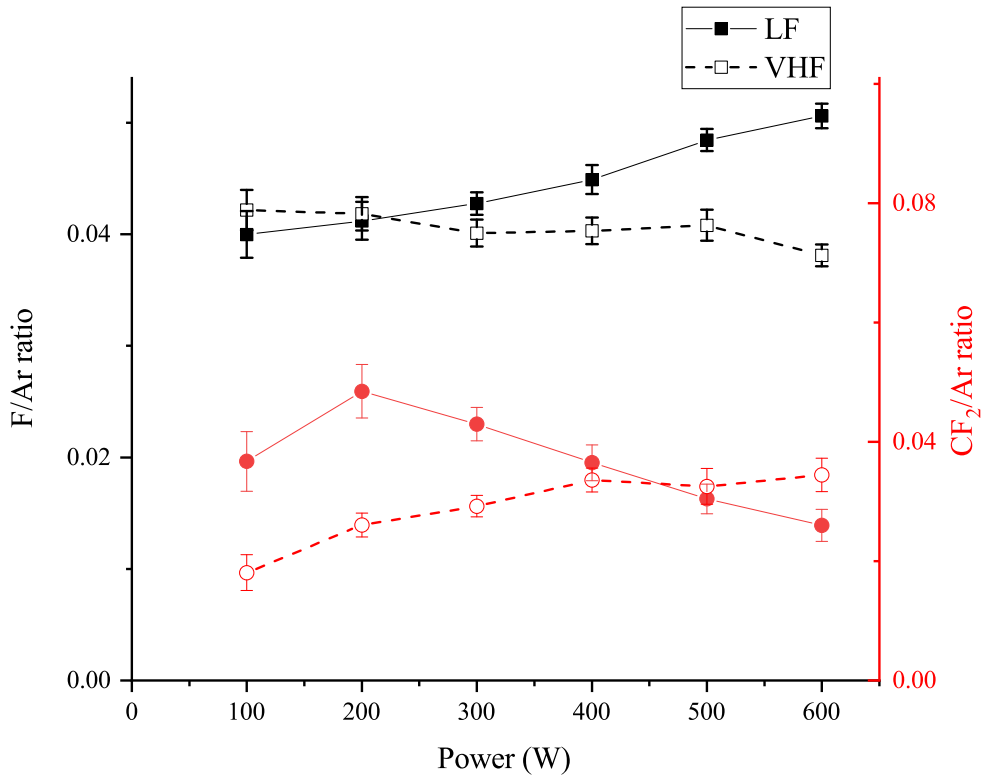

Figure 4.2: Relative concentrations of gas-phase F and CF_2 in the plasma as a function of either applied LF or applied VHF power.

species in CHF_3, where ΔH is the dissociation bond energy derived from thermochemical data [137]:

$$(a) \qquad CHF_3 + e \rightarrow CHF_2 + F + e \qquad \Delta H(a) = 4.90\,eV$$

$$(b) \qquad CF_2 + e \rightarrow CF + F + e \qquad \Delta H(b) = 5.35\,eV$$

$$(c) \qquad CHF_3 + e \rightarrow CF_2 + HF + e \qquad \Delta H(c) = 2.43\,eV$$

In contrast to FC gases such as C_2F_6 and C_4F_8 in which different dissociation reactions can be dominated by either bulk average electron temperature or high-

energy tail of the EEDF [138], dissociation of CHF_3 is mainly controlled by bulk average T_e. The increase in relative density of F radical with increasing LF power in Figure 4.2 indicates that the probability of reaction (a) and (b) increases, therefore implying a rise in average bulk electron temperature. Similar to Section 3.2, the global model determines the electron temperature (T_e) by equating the rates of particle production with particle loss to the walls in the particle balance equation [139]:

$$\frac{K_{iz}(T_e)}{u_B(T_e)} = \frac{1}{pd_{eff}} \tag{4.1}$$

where K_{iz}, u_B and p is the ionization rate, Bohm speed and neutral gas pressure respectively. K_{iz} is strongly dependent on the shape of the EEDF, particularly with reactions with threshold energies in the 5-15 eV range, which can have large discrepancies for small shifts off of a pure Maxwellian distribution towards either Druyvesteyn or two-temperature distributions. For a given gas pressure, the electron temperature is determined only by the effective plasma bulk thickness $d_{eff} = l - 2s$, where l is the discharge gap and s is the sheath width. It has been shown in both simulation and experiment [140, 141, 142] that sheath width increases with LF voltage, therefore decreasing the effective plasma bulk size and increasing T_e. From Equation 1.18 and Figure 1.8, the sheath impedance Z_{sh} is $\propto 1/\omega$ while the plasma impedance Z_p is $\propto \omega$. Therefore, it follows that the electric field penetration of the low-frequency component into the plasma bulk is larger than for the high-frequency component. Furthermore, for electronegative discharges like CHF_3, the electron density and bulk conductivity is lower than purely electropositive gases, therefore the electric field penetration is higher again leading to enhanced electron heating in the bulk [143]. In addition to increasing sheath width, LF power also increases sheath potential. As shown by PIC simulation results [140] higher sheath potential, causing high-energy ion bombardment to the electrode can produce secondary electrons which can be accelerated in the sheath and bounce into the bulk plasma, further raising the electron temperature. The ratio of CF_2 (at 251.9 nm) to Ar line is also plotted in Figure 4.2, and shows an eventual decreasing trend for LF, while for VHF there

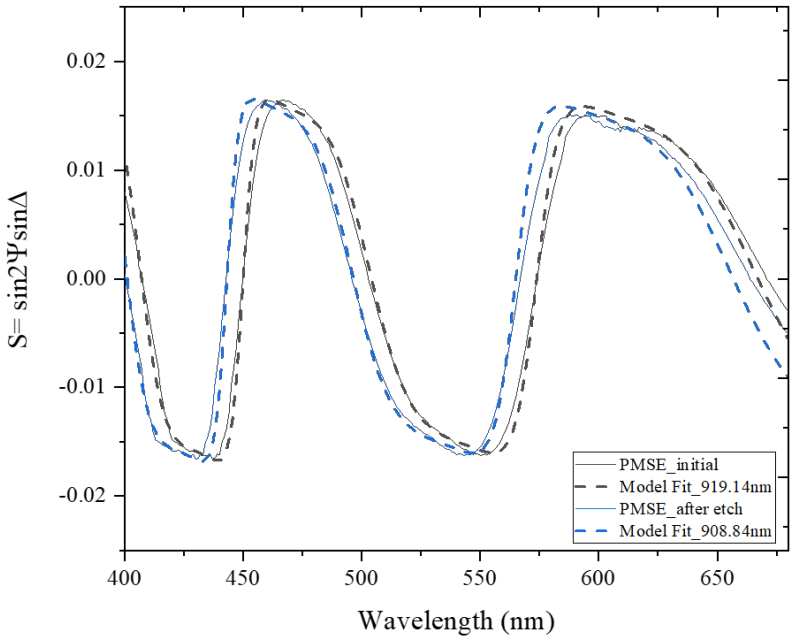

Figure 4.3: Sample PMSE measured S parameter and optical model fit for a 200 W LF Ar plasma exposure resulting in a 10.3 nm sputter etch of SiO_2.

is an increase in the CF_2/Ar ratio for increasing power. It should be noted that the validity of actinometry for CF_2 with Ar is somewhat questionable because of the large difference between corresponding excitation thresholds (4.9 eV and 13.5 eV respectively). However, the contribution of dissociative excitations is less in CHF_3 than in other fluorocarbon gases (C_4F_6, C_4F_8) with dissociative fragments of C_xF_y with low thresholds of ~10 eV. In any case, the CF_2/Ar ratio trend with power is consistent with the F/Ar trend (Figure 4.2), and serves to support the interpretation of increasing densities of mid-energy electrons in the EEDF (towards Druyvesteyn) with applied LF power, resulting in higher probability of reactions (a) and (b), and lower relative probability of reaction (c).

Evidence of higher sheath potential and in turn higher ion energy for increasing LF power is investigated by measuring the physical sputtering rate of SiO_2

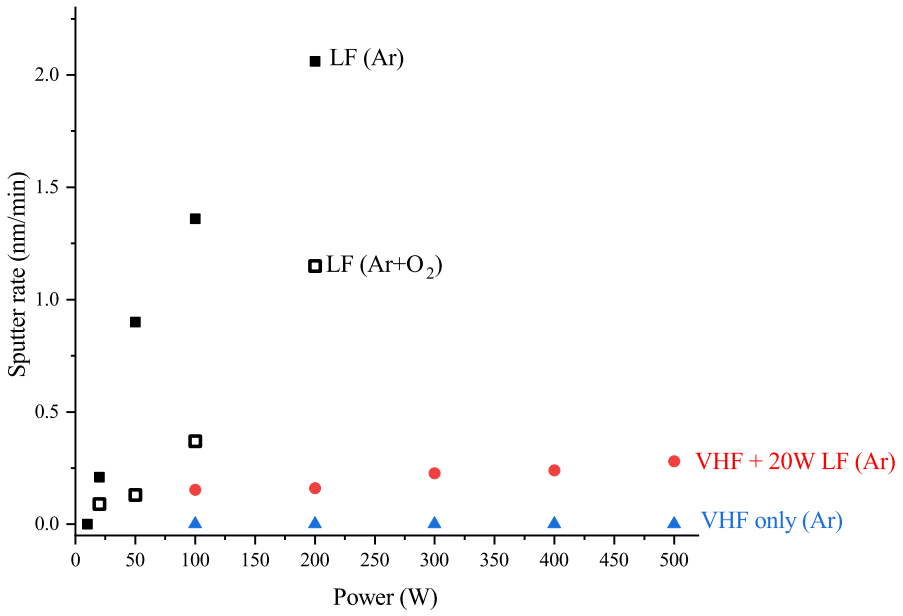

Figure 4.4: Sputter rate of SiO_2 as function of applied LF and VHF power. For Ar conditions, pressure is 68 mTorr and for Ar+O_2 pressure is 98 mTorr.

(Section 1.5.2). The SiO_2 film thicknesses are measured by in-vacuo PMSE and ex-situ ellipsometry. The optical model used for ellipsometry measurements consists of a fixed bottom Si layer and a transparent SiO_2 top layer parametrised with a Cauchy dispersion relation [144]. Figure 4.3 shows a sample plot of the ellipsometric S parameter ($S = \sin 2\Psi \sin \Delta$) measured from in-vacuo PMSE (Section 2.8) and corresponding model fit for a 200 W LF Ar plasma exposure resulting in a 10.3 nm sputter etch.

For the sputter rates plotted in Figure 4.4, SiO_2 thickness is measured before loading into the process chamber. After 5 minutes exposure of each plasma condition, the thickness change is measured and in turn sputter rate (nm/min) is determined. The sputter etch threshold has been reported elsewhere to range between 30 and 50 eV [69]. The sputter rate increases with applied power up to 200 W in both Ar (65 mTorr) and Ar/O_2 (98 mTorr). In the case of Ar/O_2 there

is a lower average energy for the atoms arriving at the surface, and therefore a lower sputter yield. For a fixed 20 W LF power, the sputter rate remains approximately constant with the addition of VHF power up to 500 W. This important result indicates that the addition of the VHF source power does not increase ion energies on the opposing substrate electrode in 2-frequency operation. Also, with no LF power and increasing VHF power up to 500W, there is no measurable sputtering occurring. This result is consistent with the findings in the PASTIS reactor (Section 3.5). The IEDs measured by the energy-resolved mass spectrometer in PASTIS for comparable pressure and power conditions showed minimal increase in ion energies at the opposing grounded electrode with increasing power. In a geometrically-symmetric single-frequency driven CCP with a multi-tile VHF source, we attribute this effect to a self-bias developing at the powered multi-tile electrode. In the Starchief experimental system, with the addition of LF substrate-bias, there is the additional effect of functional separation of ion-energy and plasma-density by low-frequency and high-frequency components respectively. The ratio of LF/(V)HF ratio here, 27 MHz/162 MHz is 0.16, which is expected to exhibit independent control from simulation reports [37], and our results of electron density and sputter rate (Figure 4.1 and 4.4) corroborate this.

4.3 Fluorocarbon Deposition

The results from Section 4.2 demonstrate that species fluxes and relative ratios in the fluorocarbon discharge can be controlled by VHF excitation while ion-energy, from LF substrate bias, is maintained below sputtering threshold. First, we investigate and characterise the deposition of fluorocarbon layers by LF only. LF power is set at 10W, to avoid physical sputtering of SiO_2 (Figure 4.4), and 50 sccm CHF_3 is added to 100 sccm Ar discharge; resulting pressure 98 mTorr. After 2 minutes, the sample is taken out for ex-situ XPS.

Deposited FC films are primarily characterised by the C1s spectral signatures. Figure 4.5(a) shows the XPS spectrum of the C1s high resolution scan before

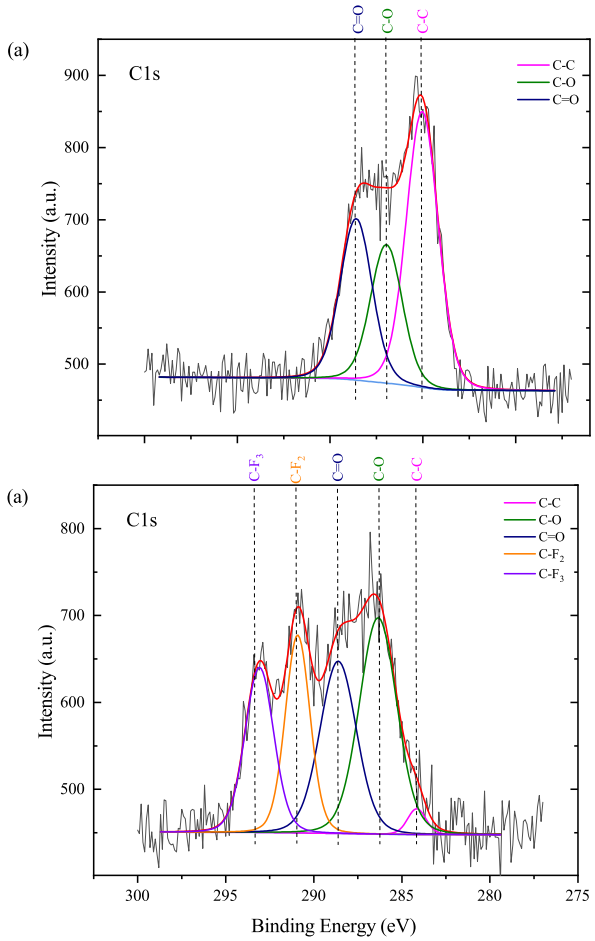

Figure 4.5: XPS high-resolution C1s spectra for (a) initial SiO_2 and (b) after fluorocarbon deposition by 10 W LF measured at normal emission.

deposition. The C1s photoemission spectrum from this reference SiO_2 scan, attributed to some adventitious carbon, is comprised of the main carbon (C-C) component, plus some amounts of singly and doubly bound oxygen. The C1s spectrum after deposition with LF, measured at normal emission from the sample surface, is plotted in Figure 4.5(b), and shows higher-binding-energy shifting which is ascribed to CF_x(x=1,2,3) species bonding [145]. The chemical shift and bonding to fluorine is similar to oxygen, therefore it is difficult to distinguish between CF_x and C-O contributions (i.e. C-O/C-CF_x or C=O/C-F) solely on the C1s spectrum. From the wide-energy-range survey scan and determination of el-

emental composition, it is clear there is a transparency in the deposited FC film. This transparency means there is significant contribution from the underlying substrate Si2p and O1s peaks (77% and 71%) respectively, therefore we attribute two of the fitted component peaks in the C1s spectrum (Figure 4.5(b)) to C-O and C=O respectively. The remaining high binding energy peaks are assigned to C-F_2 and C-F_3 [146, 147].

Now, we look at the FC deposition with the addition of VHF source power (LF substrate bias maintained at 10 W). Figure 4.6(a) shows the C1s spectrum before deposition, and after FC deposition with 300 W VHF power for 20 s measured at (b) normal emission and (c) 60° off-normal emission. From the survey scans and elemental composition analysis, there is not a significant contribution from Si2p and O1s peaks from the underlying substrate, therefore in the deconvolution of the C1s spectrum after VHF deposition, we attribute the components to C-CF_x and C-F bonding instead of bonding to oxygen. In total, the peaks in the C1s spectrum are assigned to C-C, C-CF_x C-F, C-CF_2, and C-F_3 [146, 147].

The fluorine-to-carbon ratio is often used to characterise deposited fluorocarbon films, as it is known to affect the etching characteristics, such as etch rate and selectivity of dielectric materials [64, 148]. The stoichiometry of the deposited layers, in terms of fluorine-to-carbon ratio can be calculated by independent methods; by dividing the ratio of the F1s core level signal by that of the C1s core level signal in the survey scan after correcting for differences in photoemission cross-sections (F1s/C1s), or from the deconvolution of the C1s spectrum components (F/C_{decon}) [149] as:

$$F/C_{decon} = \frac{3I_{CF_3} + 2I_{CF_2} + 1I_{CF}}{I_{C1s}} \tag{4.2}$$

where I_{CF_x} is the peak area of each fluorinated group and I_{C1s} is the total area of the C1s spectrum. F/C_{decon} from the deconvolution of the C1s spectrum measures the fluorine content in the deposited layer, while the F1s/C1s value determines the fluorine content in both the FC deposited layer, and the underlying SiO_2. Therefore, by observing the difference between the ratio values ($\Delta F/C$ =F1s/C1s -F/C_{decon}) provides an indication of substrate fluorination. For the

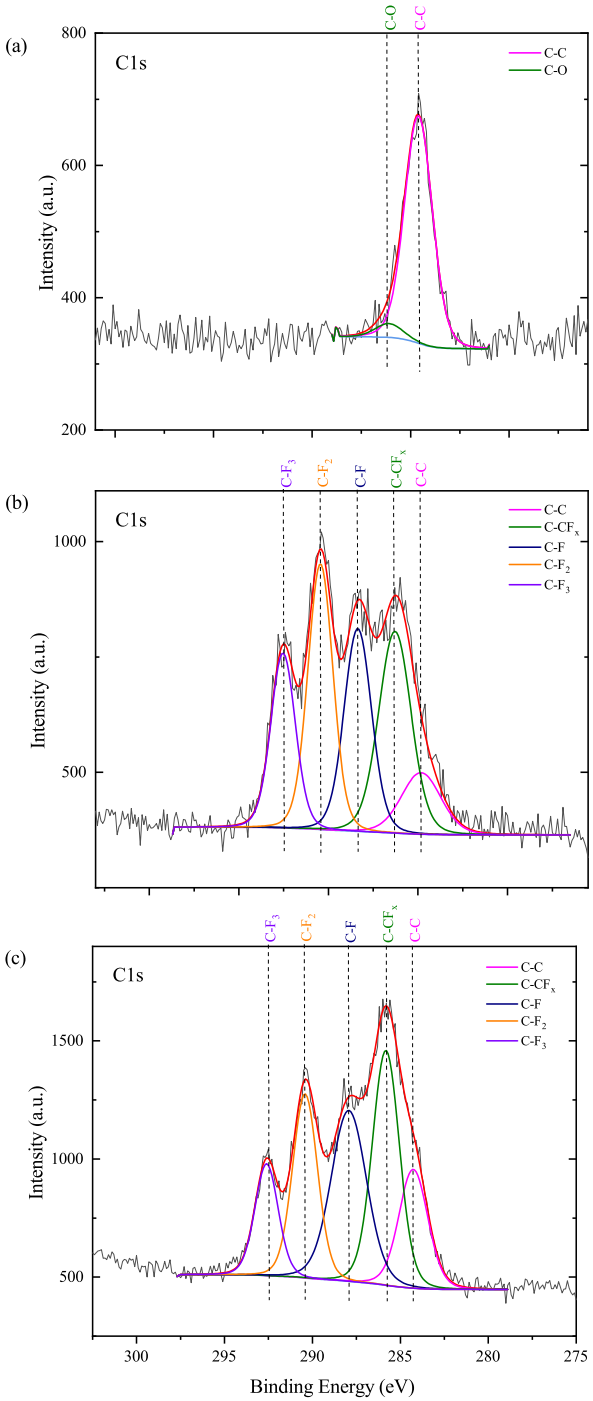

Figure 4.6: XPS high-resolution C1s spectra for (a) initial SiO_2, (b) and (c) after fluorocarbon deposition by 300 W VHF measured at normal emission and 60° off-angle respectively.

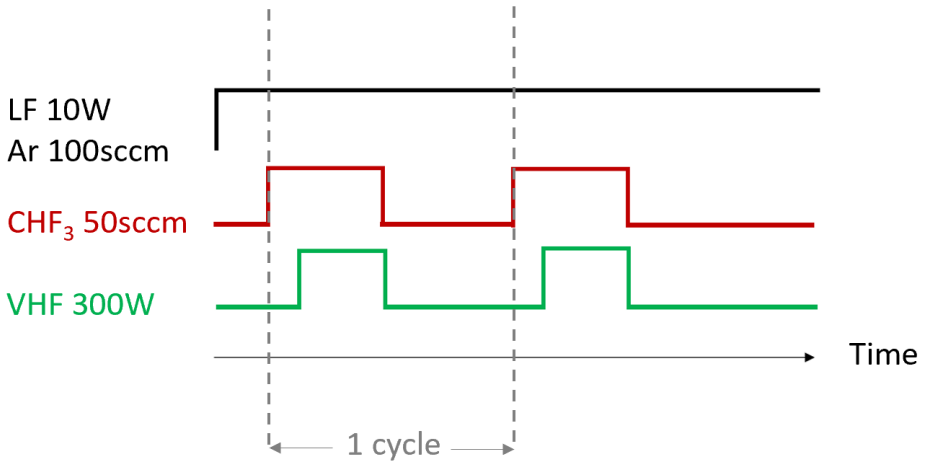

Figure 4.7: Schematic of gas and VHF power delivery times employed during the ALE process with Ar only in removal step.

FC layer deposited with 300 W VHF source power $\Delta F/C = 1.16$ suggesting that a significant amount of the F1s photo-electrons detected must originate from fluorine species that are not bonded to carbon. To further validate this observation, XPS spectra measured 60° off-normal emission are obtained. Spectra taken at an increased angle (off-normal emission) are more surface sensitive than those taken at normal emission, such that $\Delta F/C$ from 60° off-normal emission is now 0.45, much less than for normal emission. In the off-normal emission scans, there is a corresponding 24% decrease in the C-F_2 bonding and a 56% increase in the C-C bonding. The difference in the values of F/C from both normal and 60° off-normal emission show there is a gradient in the fluorine concentration with a higher F concentration towards the substrate SiO_2 in the VHF grown film.

4.4 Self-limiting ALE of SiO_2 with CHF_3 and Ar/O_2

Following FC deposition by VHF at 300 W for 20 s, we first investigated an ALE cycle with only Ar gas flow in the etch-back half-cycle. Figure 4.7 shows the

typical process sequence during this ALE cycling. For the entire process, there is continuous Ar flow at 100 sccm and constant LF bias power of 10 W. The position of the throttle valve above the turbo pump is kept constant such that the pressure varies between 68 mTorr and 98 mTorr for Ar only (etch half-cycle) and Ar + 50 sccm CHF_3 (deposition half-cycle) respectively. Synchronisation and automation of gas delivery (gating of pneumatic valves after MFCs) and VHF power is achieved by means of delay generators (Stanford Research DG535) controlled via LabVIEW. There is a time delay ($\sim$10 s) between change of gas flow at the gas-box MFCs and arrival of gas at the chamber, which is factored into the timing sequence.

For ellipsometry measurements, a two-layer optical model is used which consists of a bottom layer of SiO_2 and a varying top layer representing SiO_2 and a fluorocarbon layer, parametrised with a Cauchy dispersion relation. This model provides a good approximation of the data since the refractive indices of the fluorocarbon layer and underlying SiO_2 film are similiar [65, 150, 151]. In any case, the small differences in refractive index of the layers are negligible due to the large differences in thickness between the FC layer ($\sim$1 nm) and the SiO_2 layer ($\sim$900 nm).

During ion etching in the removal half-cycle, fluorine atoms in the FC layer react with the silicon atoms in the SiO_2 to form SiF_x by-products while carbon atoms react with oxygen in the SiO_2 to produce gas-phase CO_x molecules. Although a plateau in thickness change is detected after 2 minutes of an Ar plasma in the removal step, there are drifts in etch-per-cycle (EPC) over subsequent ALE cycles and in variability across several samples. We identified that this is due to a significant accumulation of CF_x on the chamber walls, which has been shown previously [64, 152] to induce changes in the plasma condition of subsequent deposition half-cycle steps, and in turn causing EPC variation as it enters gas-phase. This results in a non-fully self-limiting etch. The effect of CF_x build up is even more pronounced in large-volume reactors (ICPs, ECRs) because the fractional area of the pump to chamber walls is even smaller.

We add O_2 to the Ar discharge in the removal half-cycle, to prevent wall deposits in the deposition half-cycle and incomplete removal of reactants in the

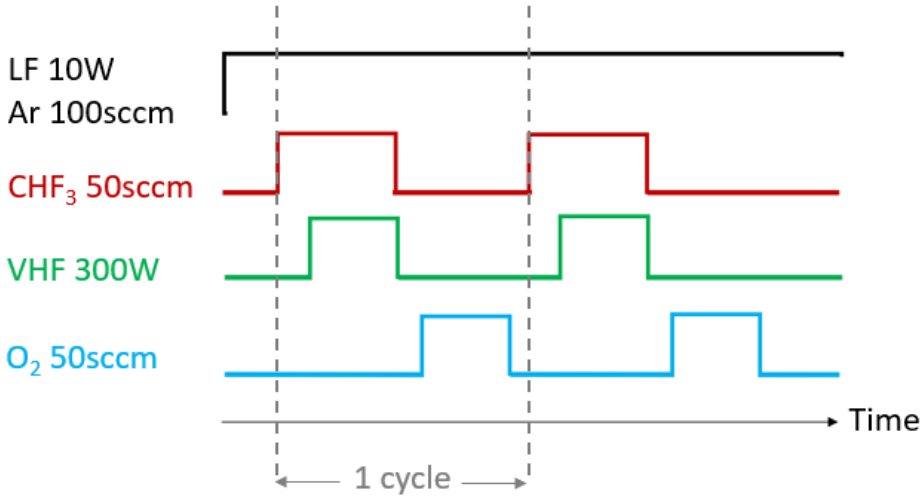

Figure 4.8: Schematic of gas and VHF power delivery times employed during the ALE process with the addition of O_2 in the removal step.

etch-back [66], and therefore to increase etch stability and achieve fully self-limting etch. In an Ar plasma, the physical interaction of Ar ions with the surface drives the oxide removal, whereas the addition of O_2 means that both physical and chemical reactions play a role in the etching mechanism. The Ar/O_2 plasma accelerates the removal of excess carbon on the surface as CO and CO_2. Figure 4.8 shows the typical process sequence for ALE cycle with the addition of O_2 in the etch-back half-cycle. The thickness change of SiO_2 as a function of process time is plotted in Figure 4.9. Following FC deposition, etching is initiated and plateaus after 30 seconds. Increased exposure time to the $Ar+O_2$ discharge shows no change in SiO_2 thickness. This is evidence of fully self-limiting behaviour; we are in a regime where ion energies in the removal half-cycle are more than the threshold energy to initiate reaction of the FC reactive layer with the substrate, but less than the physical sputtering threshold.

Total thickness etched after 1, 3, 10 and 25 ALE cycles and corresponding EPCs are plotted in Figure 4.10 with error bars representing variation across different sample runs. Reproducible EPCs of 0.4-0.5 nm/cycle are obtained (1 monolayer of SiO_2 is 0.35 nm [153]), and it is clear there is no significant drift in EPC with increasing cycle number.

Monitoring of optical emission is a time-honored approach to plasma-etch end

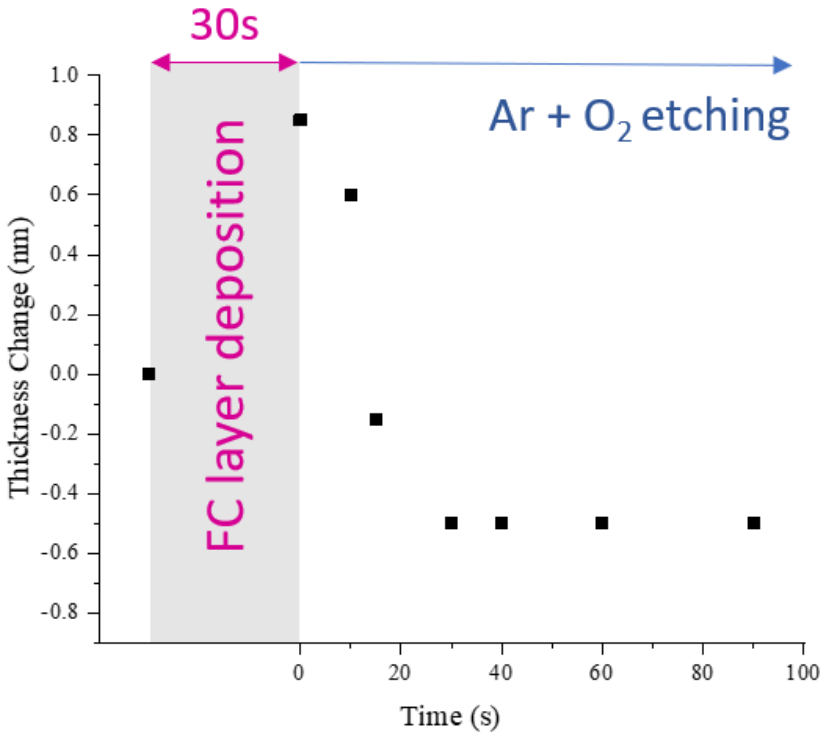

Figure 4.9: Thickness change of SiO_2 as a function of process time.

point detection [154]. In this way, selected chemical species identified as volatile by-products of the process are tracked as an indication of the extent of material removal. Here, we track CO emission as an indicator of etch-stop in the fluorocarbon based ALE removal of SiO_2. Figure 4.11(a) plots the peak intensity of CO optical emission as a function of process time with only Ar in etch-back step. As shown in Figure 4.11(a) the CO emission line initially increases then decays to an intensity higher than before etch initiation. This supports our previous observation of variable EPC and CF_x accumulation on the chamber walls. With only Ar, there is incomplete removal of reactants in the etch-back. Whereas, as shown Figure 4.11(b), the addition of O_2 accelerates the removal of excess carbon. The CO emission signal increases at a faster rate than in pure Ar, and decays rapidly to an intensity lower than before etch initiation. A plateau is discernible after 25 seconds. This decay and plateau time is consistent with the active-etch-period in Figure 4.9.

Although a fully self-limiting removal process is evidenced in Figure 4.9 and

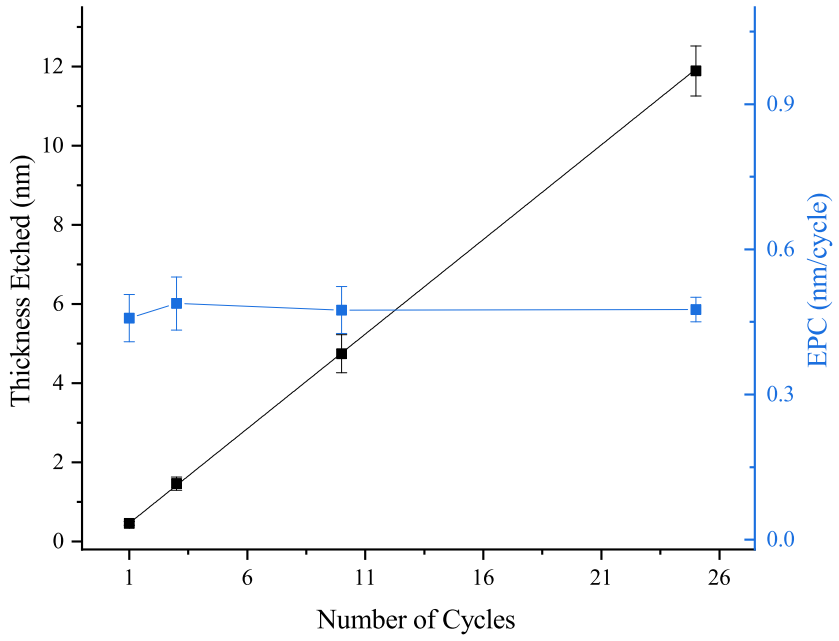

Figure 4.10: Total thickness etch and corresponding EPC(etch-per-cycle) as function of number of cycles.

4.11(b), it is important to investigate the composition of the SiO_2 surface after several cycles of ALE. Ideally, the surface at the conclusion of SiO_2 ALE cycles should be completely free of any C-related species [136]. Several reports [64, 68, 156] show evidence of a carbon-rich residue remaining on the surface with Ar plasma in the etch-back removal step. In a conventional ICP system, Kaler et al [68] showed a 0.2 nm thick C-film accumulates over the course of multiple cycles to the point of impeding subsequent etching. In an attempt to suppress the build-up of carbon residue, they added 2% O_2 to the Ar plasma in the removal step. Although the carbon buildup is slowed, the EPC also reduced from 0.19 nm/cycle to ∼0.04 nm/cycle, while adding 20% O_2 stopped etching completely.

Table 4.1 compares the SiO_2 elemental composition from XPS survey scan, and Figure 4.12 plots the C1s spectra for initial SiO_2 and after 10 cycles of our ALE process with $Ar+O_2$ in etch-removal. The peak intensity in Figure 4.12 is not directly representative of carbon content. Instead, from Table 4.1 the car-

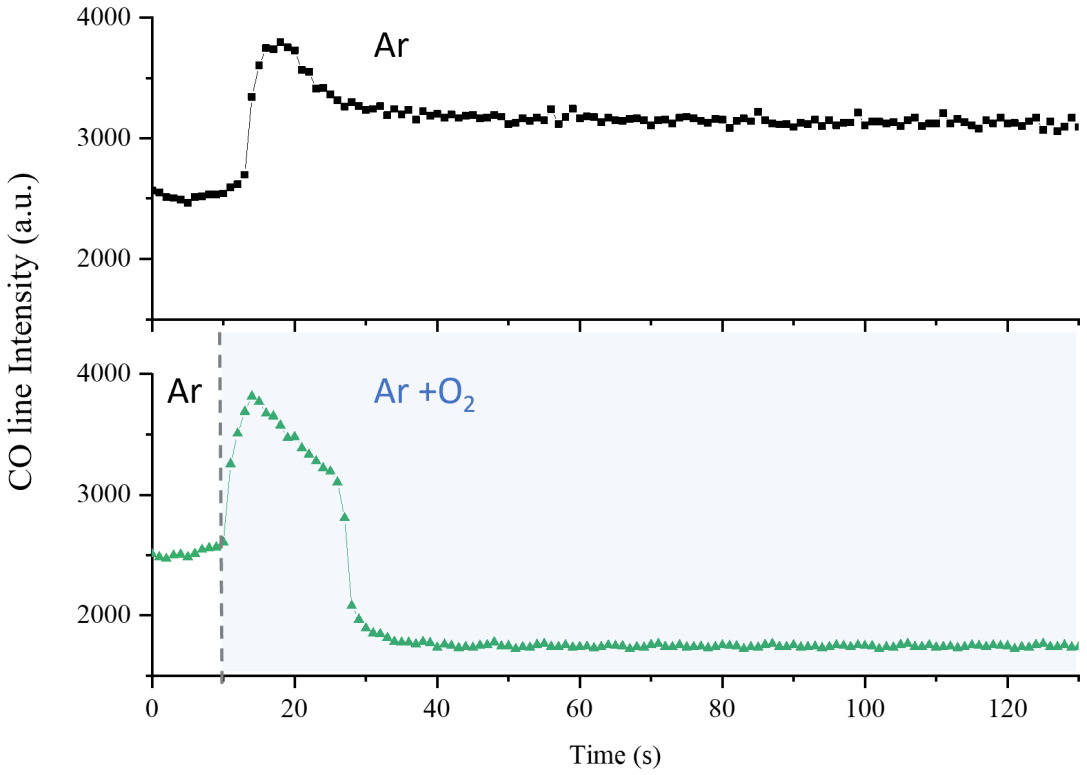

Figure 4.11: OES intensity of CO emission line as function of process time with Ar only (a) and with Ar+O_2 (b) in etch-back step.

bon content before treatment is 6.46% compared to 4.57% after 10 ALE cycles. The C1s spectrum is shifted slightly to higher binding energy indicative of some residual fluorine (6.57%). However, there is no evidence of shifting to lower binding energy in Figure 4.12, i.e. there is no increase in C-C peak bonding. This validates data in Figures 4.9 and 4.11(b), that the presence of O_2 in the etching step is sufficiently removing any residual carbon atoms, and desorbing from the surface as volatile CO or CO_2.

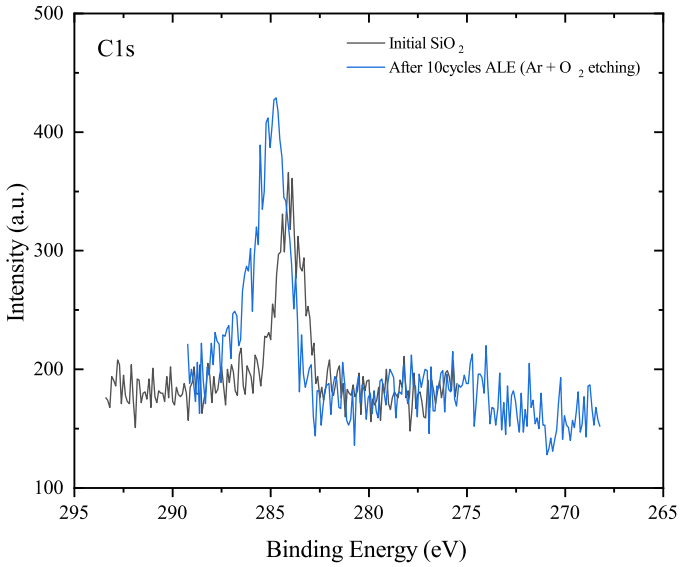

Figure 4.12: XPS high-resolution C1s spectra for initial SiO_2 and after 10 cycles of ALE

4.5 Summary

This chapter presents results of an ALE process with a fully self-limiting etch of SiO_2, demonstrated in *Starchief*; a large-area, low-volume, 2-frequency CCP (VHF 162 MHz source + LF 27 MHz wafer bias).

Frequency coupling of the VHF source power and the LF bias wafer to discharge conditions is investigated. Electron density measurements show sufficient separation of the VHF and LF power sources; VHF dominately drives the plasma formation. Dissociative species of CHF_3 are observed using OES. Actinometry analysis of atomic F concentrations shows a monotonic increase with applied LF power, whereas increasing VHF power does not contribute to a higher F content. The physical sputtering rate of SiO_2 is measured for increasing LF and VHF power. The results show sputter rate increases with LF power above 20 W. For a fixed 20 W LF power, the addition of VHF power does not increase ion energies (and therefore sputter rate).

Fluorocarbon layers deposited by CHF_3/Ar with 300 W VHF (+ 10 W LF) are

Name	Position [155]	% Composition	
		Reference SiO_2	After 10cycles ALE
Si 2p	103.5 eV	34.66	31.37
C 1s	285 eV	6.46	4.57
O 1s	532.5 eV	58.88	57.49
F 1s	686.7 eV	0	6.57

Table 4.1: XPS elemental composition from wide-energy-range survey scan of initial SiO_2 and after 10 cycles of ALE

characterised using XPS. Following FC deposition, we investigated an ALE cycle with only Ar gas flow in the etch-back half-cycle. Drifts in EPC and variability between samples for this process is attributed to CF_x build up on the chamber walls. With O_2 added to the Ar discharge in the removal half-cycle, a fully self-limiting ALE process is achieved, producing an etch-per-cycle of 0.4-0.5 nm/cycle. This is evidenced by a plateau in etch-back thickness change and also a plateau in the CO etch by-product emission signal, with a decay time that is consistent with the active-etch-period measured by ellipsometry. The composition of the SiO_2 surface after several cycles of ALE is investigated by XPS, and shows no evidence of a carbon-rich (such as C-C bond) residue.

Chapter 5

Conclusions and Future Work

In conclusion to this thesis, the main results are summarised. The motivation for this research was to gain further insight into the phenomenological aspects of Very-High-Frequency (VHF) Capacitvely-Coupled-Plasma (CCP) discharges, and to investigate the applicability of a VHF multi-tile plasma source to Atomic-Layer-Etching (ALE) of SiO_2.

In Chapter 3, the plasma kinetics, resultant gas-phase chemistry and ion-induced reactions at the substrate-holding electrode in the PASTIS (single- frequency 162 MHz VHF multi-tile CCP) reactor was explored. Hairpin probe was used to provide spatially resolved electron density profiles. At a lower gas pressure (50 mTorr), plasma density profile shows a maximum at the tile centre and a minimum at the tile-tile boundary, whereas, at higher pressure (500 mTorrr) the density peak is shifting towards the tile-tile boundary. At higher powers, the spatial structure is highly suppressed and governed by diffusion. Results showed that spatial uniformity can be improved and edge effects can be minimized by changing the power-pressure matrix; non-uniformities of within 10% are achieved. The changes in the density profiles and improvements in uniformity with power and pressure were elucidated by the power coupling mechanisms in a VHF multi-tile discharge. To evaluate the heating mechanism in PASTIS, the ratio of stochastic to ohmic heating was calculated in a N_2 discharge as a function of power at 50 and 500 mTorr. For all conditions, the ratio was greater than 1; stochastic heating is dominant in the VHF discharge. For increasing power, it was observed that plasma density increases monotonically (attributed to stochastic heating), and increasing presssure causes an initial rise then a decrease in plasma density. A global model approach was used to understand these electron density trends with pressure.

VHF discharge non-equilibrium was investigated by Optical-Emission- Spectroscopy (OES); vibrational (T_{vib}) and rotational (T_{rot}) temperatures in N_2. For T_{vib}, the sequence of transitions used from the N_2 Second-Positive-System (SPS) align with the Boltzmann plot (correlation coefficient $\geq$0.89). There is no evidence of overpopulation in any of the excited states, suggesting minimal contribution from metastables affecting population statistics. The absence of energy pooling from metastable states ($A^3\Sigma_u^+$) is consistent with a bi-Maxwellian EEDF in VHF discharge. The resulting T_{vib} values are in the range of 6250-9400 K, and

increase with RF power, analogue to plasma density. Measured T_{rot} (350-450 K) is slightly above room temperature for all operating conditions. The effect of RF power and pressure is minimal, mostly within the error bar of ±30 K. Lower operating temperature (inferred from T_{rot}) are highly desirable for ALE processing; to provide better control of the thermodynamic process window. The highly non-equilibrium conditions (the large difference between T_{vib} and T_{rot}) in VHF mean it is highly efficient in producing unique gas-phase chemistry.

A mode transition versus RF power in a low pressure VHF O_2 discharge was investigated. The electrode voltage and current, charged particle density, including negative ions, and ion energy distribution function were measured experimentally as a function of power from 200-1000 W. The results show that an inflection point is observed in the measured electrode voltage and current. The electron density increases smoothly across the transition, whereas the ion flux profile has a change in slope around mode transition. The negative ion density inferred from electron density and ion flux shows an increase up to the transition point and then decreases with further rise in power. Due to VHF plasma operation, the Ion-Energy-Distributions (IEDs) show symmetric narrow distribution. The corresponding mean ion energy increases with power up to the mode transition and then decreases. The results conclude that the observed mode transition is caused by the change in current coupling mechanisms and modification in the discharge impedance, including the presence of negative ions. In contrast, for electropositive discharge and higher-pressure electronegative discharge, the ion energy, and current and voltage, trends versus power are indicative of diminished negative ions and evidence of electrical asymmetry; the push-pull delivery of the Power-Splitter-Transmission-Line-Driver (PSTLD) result in floating electrode tiles that develop a DC bias such that plasma potential oscillations are substantially reduced. The PASTIS system, resembling a symmetrical geometry is shown to achieve quasi-independence of ion flux (electron density) and ion energy.

Chapter 4 presented results from the *Starchief* reactor; 2-frequency CCP (162 MHz VHF multi-tile source + 27 MHz bias at wafer). First, the effects of VHF and low-frequency (LF) powering coupling on plasma parameters were investigated to provide insight into the operational window and favourable conditions to realise ALE behaviour in our experimental system. Electron density measurements,

from hairpin probe, show sufficient separation of the VHF and LF sources; VHF dominantly drives the plasma formation.

The composition of fluorocarbon layers deposited for ALE is related to the gas-phase chemistry of the plasma. Therefore, relative reactive species densities from actinometry OES were investigated; atomic F (and CF_2) concentrations (relative to Ar) as a function of either applied LF power or applied VHF power. The results shows a monotonic increase in the atomic F densities with applied LF power, whereas increasing VHF power does not contribute to a higher F content. The CF_2/Ar ratio exhibits an eventual decreasing trend with applied LF power, while for VHF the ratio increases with power. The results, with applied LF power, indicate an increase in mid-energy electron densities in the EEDF, towards Druyvesteyn, which results in higher probability of the identified reaction pathways (producing higher F concentrations).

The ion energy effects, inferred from measured sputter rates, showed an increase in sputter rate for LF power above 20 W. However, for a fixed 20 W LF power, the sputter rate remains approximately constant with the addition of the VHF source power up to 500 W. This important result indicates that the addition of VHF source power does not increase ion energies on the opposing substrate electrode in 2-frequency operation, and is also consistent with the IED results in the PASTIS reactor.

The atomic composition and chemical bonding of the fluorocarbon layers deposited with CHF_3 by the LF and VHF formed plasmas were investigated by Xray-Photoelectron-Spectroscopy (XPS) analysis. After 2 minutes of CHF_3/Ar plasma exposure with LF power only, the high-resolution C1s spectrum showed contributions from the underlying SiO_2; two of the fitting peaks in the spectrum are attributed to C-O and C=O bonding. Following FC deposition with 300 W VHF (+10 W LF) we investigated an ALE cycle with only Ar gas flow in the etch-back half-cycle. Drifts in EPC and variability between samples for this process were attributed to CF_x build up on the chamber walls. To prevent wall deposits in the deposition half-cycle incomplete removal of reactants in the etch-back, we added O_2 to the Ar discharge in the removal half-cycle. This results in a fully self-limiting SiO_2 ALE process, producing an etch-per-cycle (EPC) of 0.4-0.5 nm/cycle. This is evidenced by a plateau in etch-back thickness change

and also a plateau in the CO etch by-product emission signal, with a decay time that is consistent with the active-etch-period measured by ellipsometry. XPS analysis of the composition of the SiO_2 surface after several cycles of ALE shows no evidence of a carbon-rich (such as C-C bond) residue.

In conclusion, we demonstrated the applicability of a VHF multi-tile plasma source to ALE of SiO_2. The advantage of the unique gas-phase chemistry and reduced ion-energy at the substrate electrode in VHF facilitates fully self-limiting etching of SiO_2. This also means the broader process window of VHF excitation allows for variability to future applications and requirements.

Future work, therefore, could include investigation into selectivity to other materials. For the application to Self-Aligned-Contact (SAC) (Section 1.5.2) structures, high etch selectivity of SiO_2 over Si_3N_4 is required to maintain the Si_3N_4 spacer after SiO_2 removal. The threshold for physical sputtering of Si_3N_4($\sim$20 eV) is lower than for SiO_2. However, due to differences in bond strength, substrate stoichiometry, and volatility of reaction by-products, the Si_3N_4 surface exhibits a lower carbon consumption. Conventional selective plasma etching of SiO_2 to Si_3N_4 exploits this carbon consumption difference. Specifically, in selective ALE, the FC film thickness and composition can be controlled independently, unlike in conventional RIE. The thickness of the deposited film can be controlled by the duration of the modification half-cycle and, generally, the type of fluorocarbon feed gas determines the composition of the FC layer. However, if the composition of the FC film can be changed by altering the plasma chemistry for a given parent feed gas, then this would offer additional process variability. Preliminary experiments during this PhD work from pulsing the VHF fluorocarbon discharge during the ALE cycle show some promisingly results. For a pulse period of 45 ms (gas residence time $\sim$450 ms), we investigated a 30% duty cycle of 1000 W to be comparable to the steady-state power condition presented in Section 4.4. XPS analysis of the deposited fluorocarbon layer showed a reduction in the fluorine-to-carbon ratio, and also a reduction in the ΔF/C ratio, suggesting there is less substrate fluorination. Furthermore, for this pulse-VHF plasma condition, the composition of the SiO_2 after several (10) cycles of ALE showed less residual fluorine as compared to the steady-state ALE condition. It would be fruitful to investigate further if a time-modulated VHF discharge could control the generation ratio of

CF_2 radicals to F atoms, and subsequently affect the FC film composition and etch selectivity. This would require insight into the electron temperature growth and decay rates by time-resolved hairpin electron density measurements. It may be possible that control of T_e over the pulse period (exploiting time dependence of dissociation pathways) and control of the pulse period and gas residence time ratio could provide interesting future results.

This PhD work provided the first experimental evidence of electrical asymmetry in a multi-tile VHF CCP system. The differential drive by the PSTLD is floating, therefore it would support the existence of a DC bias and development of electrical asymmetry. Another important area for future work would be to experimentally measure the existence and magnitude of this DC bias. The challenge would be to develop a diagnostic probe that will not drain away charge from the plasma, causing a perturbation and even an additional asymmetry between the tiles and probe.

Appendix A

Supplementary Figures

The data in Figure A.1 and A.2 is supporting material for Section 3.4. Following [157], the ratio of the positive ion flux to the electron density in electropositive (Ar) discharge provides a calibration for determining negative ion density in electronegative (O_2). Figure A.1 shows the measured electron density (from hairpin probe) versus power for Ar at 10 mTorr. Figure A.2 shows the ion-flux (from planar flux probe) measured in the same discharge condition.

Figure A.3 is supporting material for Section 4.3. Figure A.3

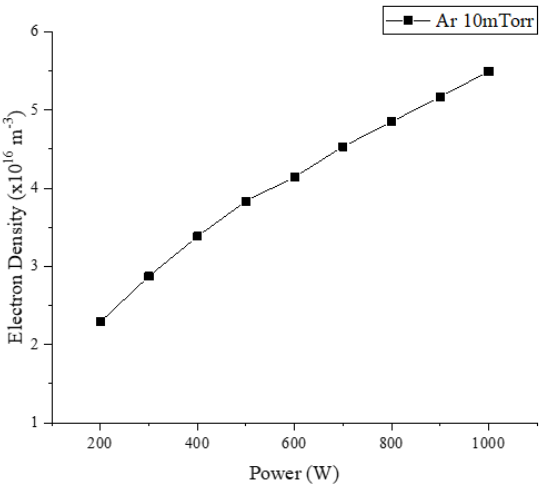

Figure A.1: Electron density as function of power measured in Ar 10 mTorr

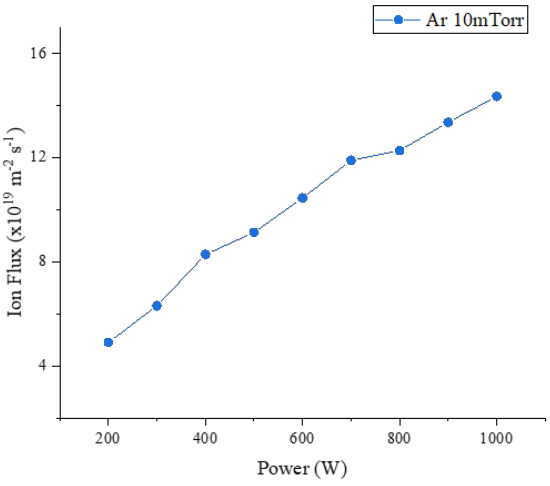

Figure A.2: Ion flux as function of power measured in Ar 10 mTorr

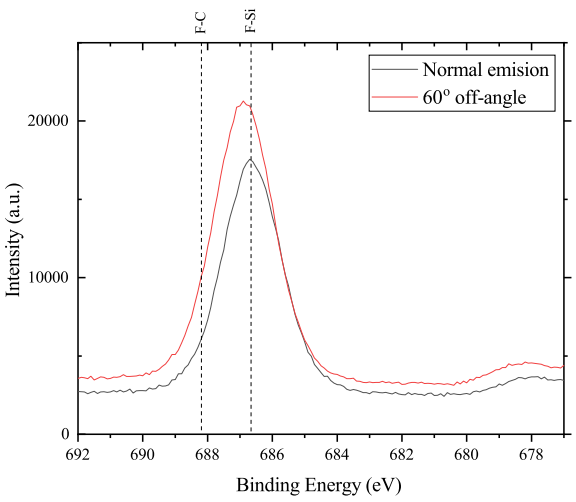

Figure A.3: XPS high-resolution F1s spectra for ***

References

[1] King S W 2015 ECS J. Solid State Sci. Technol. **4** N3029–N3047 3

[2] Kanarik K J, Tan S and Gottscho R A 2018 J. Phys. Chem. Lett. 4814–4821 3, 15

[3] Tonks L and Langmuir I 1929 Phys. Rev. **33** 195–210 4

[4] Lieberman M A and Lichtenberg A J 1994 Principles of Plasma Discharges and Materials Processing 2nd ed (New York: Wiley) 5, 10, 11, 15, 27, 74

[5] Turner M M 1995 Phys. Rev. Lett. **75** 11

[6] Godyak V A and Piejak R B 1990 Phys. Rev. Lett. **65** 996–999 12, 22, 73

[7] Kawamura E, Vahedi V, Lieberman M A and Birdsall C K 1999 Plasma Sources Sci. Technol. **8** R45–R64 12

[8] Benoit-Cattin P and Bernard L C 1968 J. Appl. Phys. **39** 5723–5726 13

[9] Agarwal A and Kushner M J 2005 J. Vac. Sci. Technol. A Vacuum, Surfaces, Film. **23** 1440–1449 14

[10] Attri P, Arora B and Choi E H 2013 RSC Adv. **3** 12540 15

[11] Coburn J W and Winters H F 1979 J. Vac. Sci. Technol. **16** 391–403 16

[12] Pearton SJ N D 2005 Plasma Process. Polym. **12** 17

[13] Vrtacnik D, Resnik D, Aljancic U, Mozek M and Amon S 2005 Device Process Technol. Microelectron. MEMS, Photonics IV **6037** 603720 17

[14] Samukawa S, Nakagawa Y, Tsukada T, Ueyama H and Shinohara K 1995 Jpn. J. Appl. Phys. **34** 6805–6808 17, 22, 24

[15] Godyak V A and Chung C W 2006 Jpn. J. Appl. Phys. **45** 8035–8041 18

[16] Vinogradov G, Menagarishvili V, Kelly A and Hirano Y 2004 Advanced Dielectric Etch Using 200/300-mm Low Residence Time GrovyICP Etcher Electrochem. Soc. Int. Meet. URL `https://www.electrochem.org/dl/ma/206/pdfs/0899.pdf` 18

[17] Curley G 2009 The dynamics of the charged particles in a dual frequency capacitively co Ph.D. thesis Ecole Polytechnique 19

[18] Kushner M J 2003 J. Appl. Phys. **94** 1436–1447 21

[19] Sekine M, Narita M, Horioka K, Yoshida Y and Okano H 1995 Jpn. J. Appl. Phys. **34** 6274–6278 21

[20] Vahedi V, Birdsall C K, Lieberman M a, DiPeso G and Rognlien T D 1993 Phys. Fluids B Plasma Phys. **5** 2719–2729 21

[21] Surendra M and Graves D B 1991 Appl. Phys. Lett. **59** 2091–2093 21

[22] Meyyappan M and Colgan M J 1996 J. Vac. Sci. Technol. A Vacuum, Surfaces, Film. **14** 2790–2794 21

[23] Kitajima T, Takeo Y, Nakano N and Makabe T 1998 J. Appl. Phys. **5928** 21

[24] Ferreira C M and Loureiro J 1984 J. Phys. D. Appl. Phys. **17** 1175–1188 21

[25] Wertheimer M R 1985 J. Vac. Sci. Technol. A Vacuum, Surfaces, Film. **3** 2643 21

[26] Abdel-Fattah E and Sugai H 2003 Appl. Phys. Lett. **83** 1533–1535 21, 75

[27] Abdel-Fattah E, Bazavan M and Sugai H 2011 J. Appl. Phys. **110** 21

[28] Kim K S, Sirse N, Kim K H, Ellingboe A R, Kim K N and Yeom G Y 2016 J. Phys. D. Appl. Phys. **49** 395201 21

[29] Monaghan E, Michna T, Gaman C, O'Farrel D, Ryan K, Adley D, Perova T S, Drews B, Jaskot M and Ellingboe A R 2011 Thin Solid Films **519** 6884–6886 21, 22

[30] Abdel-Fattah E and Sugai H 2003 Jpn. J. Appl. Phys. **42** 6569–6577 22

[31] Howling A A 1992 J. Vac. Sci. Technol. A Vacuum, Surfaces, Film. **10** 1080 22

[32] Goto H H, Lowe H D and Ohmi T 1992 J. Vac. Sci. Technol. A **10** 3048–3054 23

[33] Lowe H D, H Goto H and Ohmi T 1991 J. Vac. Sci. Technol. A **9** 3090 23

[34] Robiche J, Boyle P C, Turner M M and Ellingboe A R 2003 J. Phys D Appl. Phys. **36** 1810–1816 23

[35] Gans T, Schulze J, O'Connell D, Czarnetzki U, Faulkner R, Ellingboe A R and Turner M M 2006 Appl. Phys. Lett. **89** 37–40 24

[36] Karkari S K and Ellingboe A R 2006 Appl. Phys. Lett. **88** 24

[37] Boyle P C, Ellingboe A R and Turner M M 2004 J. Phys. D. Appl. Phys. **37** 697–701 24, 102, 108

[38] Sansonnens L and Schmitt J 2003 Appl. Phys. Lett. **82** 182–184 27

[39] Sansonnens L, Schmidt H, Howling A A, Hollenstein C, Ellert C and Buechel A 2006 J. Vac. Sci. Technol. A Vacuum, Surfaces, Film. **24** 1425–1430 27

[40] Yang Y and Kushner M J 2010 J. Appl. Phys. **108** 27

[41] Jung P G, Hoon S S, Wook C C and Young C H 2013 Plasma Sources Sci. Technol. **22** 055005 27, 73

[42] Min K S, Kang S H, Kim J K, Yum J H, Jhon Y I, Hudnall T W, Bielawski C W, Banerjee S K, Bersuker G, Jhon M S and Yeom G Y 2014 Microelectron. Eng. **114** 121–125 29

[43] Park S D, Lim W S, Park B J, Lee H C, Bae J W and Yeom G Y 2008 Electrochem. Solid-State Lett. **11** H71 29

[44] Ivanov T, Pourghaderi M A, Lin D, Yu J K, Tan S, Kimura Y, Hellin D, Geypen J, Bender H, Vertommen J, Kamarthy G, Collaert N, Marks J, Vahedi V, Arghavani R and Thean A 2014 Jpn. J. Appl. Phys. **53** 29

[45] Yoder M N 1988 US Pat. 4756794 29

[46] Djamdji F and Blunt R 1993 Mater. Sci. Eng. B **20** 77–81 29

[47] Donnelly V M and Kornblit A 2013 J. Vac. Sci. Technol. A Vacuum, Surfaces, Film. **31** 050825 29

[48] Matsuura T, Murota J, Sawada Y and Ohmi T 1993 Appl. Phys. Lett. **63** 2803–2805 30, 31

[49] Sakaue H, Iseda S, Asami K, Yamamoto J, Hirose M and Horiike Y 1990 Jpn. J. Appl. Phys. **29** 2648–2652 30

[50] Agarwal A and Kushner M J 2009 J. Vac. Sci. Technol. A Vacuum, Surfaces, Film. **27** 37–50 30, 33

[51] Athavale S D and Economou D J 1995 J. Vac. Sci. Technol. A Vacuum, Surfaces, Film. **13** 966–971 30, 32

[52] Rauf S, Sparks T, Ventzek P L G, Smirnov V V, Stengach A V, Gaynullin K G and Pavlovsky V A 2007 J. Appl. Phys. **101** 30, 33

[53] Jhon Y I, Min K S, Yeom G Y and Jhon Y M 2016 **093104** 1–6 30

[54] Athavale S D 1996 J. Vac. Sci. Technol. B Microelectron. Nanom. Struct. **14** 3702 30, 32

[55] Kim J K, Cho S I, Lee S H, Kim C K, Min K S and Yeom G Y 2013 J. Vac. Sci. Technol. A Vacuum, Surfaces, Film. **31** 061302 30

[56] Kanarik K J, Tan S, Holland J P, Eppler A and Gottscho R A 2013 Solid State Tecnhology **56** 30

[57] Brichon P, Despiau-Pujo E and Joubert O 2014 J. Vac. Sci. Technol. A Vacuum, Surfaces, Film. **32** 021301 30

[58] Graves M E B and B D 1995 J. Appl. Phys. **78** 6604 30

[59] Kanarik K J, Lill T, Hudson E A, Sriraman S, Tan S, Marks J, Vahedi V and Gottscho R A 2015 J. Vac. Sci. Technol. A Vacuum, Surfaces, Film. **33** 020802 31

[60] Chang J P, Arnold J C, Zau G C H, Shin H S and Sawin H H 1997 J. Vac. Sci. Technol. A Vacuum, Surfaces, Film. **15** 1853–1863 32

[61] Heinecke R 1975 Solid. State. Electron. **18** 32

[62] Matsui M, Tatsumi T and Sekine M 2001 J. Vac. Sci. Technol. A Vacuum, Surfaces, Film. **19** 2089–2096 33

[63] Ventzek P L G, Hoekstra R J and Kushner M J 1994 J. Vac. Sci. Technol. B Microelectron. Nanom. Struct. **12** 461 33

[64] Metzler D, Bruce R L, Engelmann S, Joseph E A and Oehrlein G S 2014 J. Vac. Sci. Technol. A **32** 33, 36, 110, 113, 116

[65] Li C, Metzler D, Lai C S, Hudson E A and Oehrlein G S 2016 J. Vac. Sci. Technol. A Vacuum, Surfaces, Film. **34** 041307 34, 113

[66] Tsutsumi T, Kondo H, Hori M, Zaitsu M, Kobayashi A, Nozawa T and Kobayashi N 2017 J. Vac. Sci. Technol. A Vacuum, Surfaces, Film. **35** 01A103 34, 114

[67] Metzler D, Li C, Lai C S, Hudson E A and Oehrlein G S 2017 J. Phys. D. Appl. Phys. **50** 254006 34

[68] Kaler S S, Lou Q, Donnelly V M and Economou D J 2017 J. Phys D Appl. Phys. **50** 34, 116

[69] Oehrlein G S, Metzler D and Li C 2015 ECS J. Solid State Sci. Technol. **4** N5041–N5053 35, 107

[70] Engelmann S U, Bruce R L, Nakamura M, Metzler D, Walton S G and Joseph E A 2015 ECS J. Solid State Sci. Technol. **4** N5054–N5060 35

[71] Tatsumi T, Fukuda S and Kadomura S 1994 Jpn. J. Appl. Phys. **33** 2175–2178 35

[72] Lee C G N, Kanarik K J and Gottscho R A 2014 J. Phys. D. Appl. Phys. **47** 273001 36

[73] LamBlogStaff 2016 Web article: New Atomic Layer Etching Capability Enables Continued Device Scaling 36

[74] Michna T and Ellingboe A R 2011 Curr. Appl. Phys. **11** 41

[75] Ellingboe A R 2012 High-VHF Capacitive-Coupled-Plasma Technology , with Scaling to 450mm SEMICON-Korea pp 2–5 45

[76] Ji Y J, Kim K S, Kim K H, Ellingboe A R and Yeom G Y 2020 Appl. Surf. Sci. **506** 45

[77] Byun J Y, Ji Y J, Kim K H, Kim K S, Tak H W, Ellingboe A R and Yeom G Y 2021 Nanotechnology **32** 45

[78] Harvey C, Vandenburg S and Ellingboe A R 2021 Curr. Appl. Phys. 46

[79] Piejak R B, Godyak V A, Garner R, Alexandrovich B M and Sternberg N 2004 J. Appl. Phys. **95** 3785–3791 47

[80] Stenzel R L 1976 Rev. Sci. Instrum. **47** 603–607 47

[81] Mott-Smith H M and Langmuir I 1926 Phys. Rev. **28** 727–763 49

[82] O'Connell D, Zorat R, Ellingboe A R and Turner M M 2007 Phys. Plasmas **14** 53, 95

[83] Hamers E, Van Sark W, Bezemer J, Goedheer W and Van Der Weg W 1998 Int. J. Mass Spectrom. Ion Process. **173** 91–98 53

[84] Downie P, Reynolds D J and Powis I 1995 Rev. Sci. Instrum. **66** 3807–3818 53

[85] Gross J 2006 Mass spectrometry: Textbook (Springer Science & Business Media) 54

[86] Lofthus A and Krupenie P H 1977 J. Phys. Chem. Ref. Data **6** 113–307 58

[87] Britun N, Gaillard M, Ricard A, Kim Y M, Kim K S and Han J G 2007 J. Phys. D. Appl. Phys. **40** 1022–1029 58

[88] Gilmore F R, Laher R R and Espy P J 1992 J. Phys. Chem. Ref. Data **21** 1005–1107 58

[89] Bruggeman P J, Sadeghi N, Schram D C and Linss V 2014 Plasma Sources Sci. Technol. **23** 023001 59

[90] Poirier J S, Berube P M, Munoz J, Margot J, Stafford L and Chaker M 2011 Plasma Sources Sci . Technol **20** 60

[91] Huang X J, Xin Y, Yang L, Yuan Q H and Ning Z Y 2008 Phys. Plasmas **15** 60, 85

[92] Donnelly V M and Malyshev M V 2000 Appl. Phys. Lett. **77** 2467–2469 60

[93] Johnson A W and Fowler R G 1970 J. Chem. Phys. **53** 65–72 60

[94] Biloiu C, Sun X, Harvey Z and Scime E 2007 J. Appl. Phys. **101** 073303 60

[95] Coburn J W and Chen M 1980 J. Appl. Phys. **51** 3134–3136 60

[96] Born M and Wolf E 1980 Principles of Optics 6th ed (Pergamon Press, Oxford) 63

[97] Lee J, Rovira P I, An I and Collins R W 1998 Rev. Sci. Instrum. **69** 1800–1810 63

[98] Collins R W 1990 Rev. Sci. Instrum. **61** 2029–2062 63

[99] Hauge P S 1976 Surf. Sci. **56** 148–160 63

[100] Jasperson S N and Schnatterly S E 1969 Rev. Sci. Instrum. **40** 761–767 63, 66

[101] Acher O, Bigan E and Drévillon B 1989 Rev. Sci. Instrum. **60** 65–77 63

[102] Duncan W M and Henck S A 1993 Insitu spectral ellipsometry for real-time measurement and control vol 63 (Elsevier Science Publishers B.V.) 63

[103] Carty D 2004 RAS and STM Investigations of Pentacene Molecules on Metal and Semico Ph.D. thesis Dublin City University 64, 67

[104] Pristinski D, Kozlovskaya V and Sukhishvili S A 2006 J. Opt. Soc. Am. A **23** 2639 64

[105] Fujiwara H 2007 Spectroscopic Ellipsometry Principles and Applications vol 53 (John Wiley & Sons) 65

[106] Jasperson S N, Burge D K and O'Handley R C 1973 Surf. Sci. **37** 548–558 66

[107] Fleischer K, Carroll L, Smith C and McGilp J F 2007 J. Phys. Condens. Matter **19** 1–11 67

[108] Scientific T F The Photoemission Process. URL `https://xpssimplified.com/whatisxps-photoemission.php` 68

[109] Hofmann S 2013 Auger- and X-Ray Photoelectron Spectroscopy in Materials Science (Springer) 69

[110] Gross T, Ramm M, Sonntag H, Unger W, Weijers H M and Adem E H 1992 Surf. Interface Anal. **18** 59–64 69

[111] Repoux M 1992 Surf. Interface Anal. **18** 567–570 69

[112] Godyak V A 1986 Soviet Radio Frequency Discharge Research (Delphic Asociates, Inc., Falls Church, VA) 76

[113] Tabata T, Shirai T, Sataka M and Kubo H 2006 At. Data Nucl. Data Tables **92** 375–406 77

[114] Itikawa Y 2006 J. Phys. Chem. Ref. Data **35** 31–53 77

[115] Köhler K, Horne D E and Coburn J W 1985 J. Appl. Phys. **58** 3350–3355 77

[116] Snijkers R J M M 1993 The sheath of an RF plasma : measurements and simulations of t (Eindhoven) 77

[117] Lee C and Lieberman M A 1995 J. Vac. Sci. Technol. A Vacuum, Surfaces, Film. **13** 368–380 81

[118] Gudmundsson J T 2001 Plasma Sources Sci. Technol. **10** 76–81 81

[119] Davis G P and Gottscho R A 1983 J. Appl. Phys. **54** 83

[120] Kang Z D and Pu Y K 2002 Chinese Phys. Lett. **19** 211–213 84

[121] Mavadat M, Ricard A, Sarra-Bournet C and Laroche G 2011 J. Phys. D. Appl. Phys. **44** 155207 84, 85

[122] Levaton J and Ricard A 2004 Eur. Phys. Journal-Applied Phys. **64** 59–64 84, 85

[123] Sakamoto T, Matsuura H and Akatsuka H 2007 J. Appl. Phys. **101** 023307 85

[124] Abdel-Fattah E, Bazavan M, Sugai H and Fridman 2012 Phys. Plasmas **19** 1–9 85

[125] Khan F U, Rehman N U, Naseer S, Naz M Y, Khattak N A D and Zakaullah M 2011 Spectrosc. Lett. **44** 194–202 85

[126] Kortshagen U, Gibson N D and Lawler J E 1996 J. Phys. D. Appl. Phys. **29** 1224–1236 89

[127] Ellingboe A R and Boswell R W 1996 Phys. Plasmas **3** 2797–2804 89

[128] Ghanashev I, Nagatsu M, Xu G and Sugai H 1997 Jpn. J. Appl. Phys. **36** 4704–4710 89

[129] Chabert P, Sheridan T E, Boswell R W and Perrin J 1999 Plasma Sources Sci. Technol. **8** 561–566 90

[130] Gudmundsson J T, Kouznetsov I G, Patel K K and Lieberman M A 2001 J. Phys. D. Appl. Phys. **34** 1100–1109 90, 91

[131] Deutsch H, Scheier P, Becker K and Märk T D 2003 Chem. Phys. Lett. **382** 26–31 90

[132] Laporta V, Celiberto R and Tennyson J 2015 Phys. Rev. A - At. Mol. Opt. Phys. **91** 1–5 91

[133] Gudmundsson J T, Kawamura E and Lieberman M A 2013 Plasma Sources Sci. Technol. **22** 91

[134] Olthoff J K, Van Brunt R J, Radovanov S B, Rees J A and Surowiec R 1994 J. Appl. Phys. **75** 115–125 92

[135] Samukawa S and Furuoya S 1993 Appl. Phys. Lett. **63** 2044–2046 103

[136] Gasvoda R J, Zhang Z, Wang S, Hudson E A and Agarwal S 2020 J. Vac. Sci. Technol. A **38** 050803 103, 116

[137] Takahashi K, Hori M and Goto T 1994 Jpn. J. Appl. Phys. **33** 4745–4751 104

[138] Huang H, Ye C, Xu Y, Yuan Y, Shi G and Ning Z 2010 Plasma Sci. Technol. **12** 566–570 105

[139] Stewart R A and Graves D B 1994 J. Vac. Sci. Technol. B Microelectron. Nanom. Struct. **12** 478 105

[140] Boyle P C, Ellingboe A R and Turner M M 2004 Plasma Sources Sci. Technol. **13** 493–503 105

[141] Kitajima T, Takeo Y and Makabe T 1999 J. Vac. Sci. Technol. A **17** 2510 105

[142] Kitajima T, Takeo Y, Petrović Z L and Makabe T 2000 Appl. Phys. Lett. **77** 489–491 105

[143] Liu W Y, Xu Y, Liu Y X, Peng F, Gong F P, Li X S, Zhu A M and Wang Y N 2014 Phys. Plasmas **21** 105

[144] Patel D, Shah D, Hilfiker J N and Linford M 2019 Vac. Technol. Coat. 29–33 107

[145] Metzler D, Li C, Engelmann S, Bruce R L, Joseph E A and Oehrlein G S 2016 J. Chem. Phys. **146** 109

[146] Loong S Y, Lee H K, Chan L, Zhou M, Loh F C and Tan K 1997 Proc. SPIE 3212 3–6 110

[147] Miyata K, Hori M and Goto T 1996 J. Vac. Sci. Technol. A Vacuum, Surfaces, Film. **14** 2083–2087 110

[148] Kim Y, Lee S, Cho Y, Kim S and Chae H 2020 J. Vac. Sci. Technol. A **38** 022606 110

[149] Schaepkens M, Standaert T, Rueger N R and Oehrlein G S 1999 J. Vac. Sci. Technol. A **53** 110

[150] Gasvoda R J, van de Steeg A W, Bhowmick R, Hudson E A and Agarwal S 2017 ACS Appl. Mater. Interfaces **9** 31067–31075 113

[151] Dallorto S, Goodyear A, Cooke M, Szornel J E, Ward C, Kastl C, Schwartzberg A, Rangelow I W and Cabrini S 2019 Plasma Process. Polym. e1900051 113

[152] Schaepkens M, Bosch R C M, Standaert T E F M, Oehrlein G S and Cook J M 1998 J. Vac. Sci. Technol. A Vacuum, Surfaces, Film. **16** 2099–2107 113

[153] Knizikevičius R 2008 Vacuum **82** 1191–1193 114

[154] Litvak H E 1996 J. Vac. Sci. Technol. B Microelectron. Nanom. Struct. **14** 516 115

[155] Beamson G and Briggs D 1992 High resolution XPS of organic polymers (Wiley) 119

[156] Metzler D, Li C, Engelmann S, Bruce R L, Joseph E A and Oehrlein G S 2016 J. Vac. Sci. Technol. A Vacuum, Surfaces, Film. **34** 01B101 116